ABSTRACT

Title of Dissertation: THE FREQUENCY DISTRIBUTION OF DAILY PRECIPITATION OVER THE UNITED STATES

Emily Jones Becker, Doctor of Philosophy, 2009

Directed By: Ernesto Hugo Berbery
Department of Atmospheric and Oceanic Science

This study examines the seasonal frequency distribution of daily precipitation and related variables over the United States using the North American Regional Reanalysis. Regions where the seasonal mean precipitation is dominated by heavy and extreme daily events or by more consistent lighter events are identified. The distributions are related to the variability of the vertically integrated moisture flux convergence (MFC) and precipitable water. The modulation of daily precipitation by ENSO and the Madden-Julian Oscillation (MJO) during winter is investigated.

Assuming that the frequency of daily precipitation can be approximated by a gamma distribution, the scale and shape parameters are useful proxies to estimate the observed frequency distribution of precipitation. During winter, most areas of the country with high mean precipitation have a strong contribution from extreme events, particularly along the West and Gulf Coasts. During summer, the wettest areas of the country are Florida, where the mean precipitation is dominated by more-frequent light and moderate rainfall days, and the central Plains, dominated by variable rains and

extreme events. Throughout the year, the MFC mean and scale parameter patterns strongly resemble those of precipitation, and areas with more heavy and extreme precipitation have stronger MFC daily values. These results suggest that the frequency distribution of MFC can be used as a proxy for the frequency distribution of modeled forecast precipitation.

Changes in the winter total precipitation between the phases of ENSO are largely attributable to changes in the heavy and extreme events. Areas showing increased mean precipitation during the warm phase show an even greater increase in extremes. Similar to precipitation, strong values of MFC are more sensitive to ENSO phase than is the mean MFC. While the ENSO variability of the frequency distribution of MFC shows a strong relationship to that of precipitation, the variability of precipitable water does not. MJO modulation of winter daily precipitation over the central U.S. occurs primarily during MJO Phases 5 and 6, when MJO-related enhanced convection is located in the western Pacific. During these phases, the winter storm track is enhanced, and positive MFC anomalies are present in the central U.S.

THE FREQUENCY DISTRIBUTION OF DAILY PRECIPITATION OVER THE UNITED STATES

By

Emily Jones Becker

Dissertation submitted to the Faculty of the Graduate School of the
University of Maryland, College Park, in partial fulfillment
of the requirements for the degree of
Doctor of Philosophy
2009

Advisory Committee:
Professor Ernesto Hugo Berbery, Chair
Dr. R. Wayne Higgins
Professor Eugenia Kalnay
Professor James Carton
Professor Karen Prestegaard

Table of Contents

List of Tables

List of Figures

Chapter 1: Introduction

Changes in the frequency and intensity of daily precipitation events within a season can occur independently from changes in the seasonal mean. For example, a season with an average total rainfall amount could have a greater-than-average incidence of very heavy and extreme precipitation events, and a reduced number of light and moderate events. More extreme events, even within a season of average total precipitation amount, can lead to high streamflow and flooding (Groisman et al. 2001). Consequently, the variability of daily precipitation statistics, such as the frequency distribution and intensity of rainfall within a season, can be more informative than seasonal mean variability.

Over the past fifteen years or so, several studies have discussed the sensitivity of the frequency and intensity of daily precipitation to climate variability, on both interannual and intraseasonal timescales. Sources of variability include major climate modes such as the El Niño/Southern Oscillation (ENSO) and the Madden-Julian Oscillation (MJO). These climate modes, which are usually identified in the tropics by anomalies in sea-surface temperature, convection, or other signals, force changes in the global atmospheric circulation, which in turn affects precipitation patterns in the midlatitudes.

ENSO, which has significant effects on seasonal average precipitation and surface temperature in various regions of North America (e.g. Ropelewski and Halpert 1986, 1996; Kiladis and Diaz 1989, Higgins et al. 1999), also affects the

character of daily precipitation. ENSO is implicated in interannual fluctuations in the frequency of precipitation occurrence over the United States, and in the frequency of extreme events (Higgins et al. 2007). During the warm phase of ENSO, wintertime precipitation in several regions of the United States shows a higher frequency of heavy and extreme rainfall compared to the long-term mean; during the cold phase, Northern California experiences more light rain days and fewer heavy events than average (Gershunov 1998). Along the west coast of the United States, the largest fraction of extreme precipitation events occurs during a neutral winter before onset of the warm phase (Higgins et al. 2000b). Ropelewski and Bell (2007) found shifts in the histograms of daily precipitation between the cold and warm ENSO phases in several areas of South America, including some regions that did not show a change in the seasonal mean. The MJO has also been found to modulate daily precipitation, on intraseasonal timescales. MJO-related increases in heavy and extreme precipitation have been identified in Central America and Mexico (Barlow and Salstein, 2006) and the west coast of the U.S. (Mo and Higgins 1998a, b; Jones 2000; Higgins et al. 2000a).

Studies of the frequency distribution of daily precipitation have found that the heavy and extreme end of the distribution is more sensitive than the mean to climate variability. Changes in mean monthly precipitation in some areas of the globe are likely to be associated with disproportionately large changes in the extremes (Groisman et al. 1999). Grimm et al. (2008), looking at South America, found that areas with ENSO-related changes in the frequency of extreme events are more

extensive than areas with ENSO-related changes in monthly rainfall totals. Modeling studies of the gamma distribution of daily precipitation have found that the scale parameter, representing heavy and extreme precipitation, is very sensitive to changes in mean climate (Katz and Brown 1992; Wilby and Wigley 2002; Watterson and Dix 2003).

The distribution of daily rainfall affects the overall hydroclimate, specifically drought, flooding, and streamflow (Groisman et al. 2001; Groisman et al. 2004). Barlow et al. (2001), looking at monthly average values, found significant relationships between modes of Pacific SST variability and precipitation, drought, and streamflow in North America during summer. Variations in the character of daily precipitation, especially increases in heavy and very heavy rainfall, have been linked to increased streamflow and flooding (Groisman et al. 2001). In Oregon and Washington, the MJO can influence precipitation rates, streamflow, and flooding in autumn and winter (Bond and Vecchi 2003).

Precipitation is one of the most important fields for the average user, but it is a highly variable field, and can be quite difficult to capture accurately in models (e.g. Gershunov 1998). Gershunov and Cayan (2003) used dynamical precipitation forcing fields such as geopotential height and sea-surface temperature in predicting extreme precipitation. An understanding of other fields pertaining to the hydrological cycle, such as precipitable water and moisture flux convergence (MFC), could potentially improve precipitation modeling skill. For example, Silva and Berbery (2006) compared the observed frequency distribution of precipitation with the modeled

distributions of precipitation and MFC, and found that the MFC distribution had a better representation of the observed precipitation.

The above review suggests that detailed analysis of the statistical properties of daily rainfall will contribute to an improved understanding of the effect of dominant large-scale modes on the character of daily precipitation, which will in turn help with seasonal and sub-seasonal forecasting. Predictability of the statistics of daily precipitation on both the shorter (two weeks to one month) and longer timescales could be enhanced by a greater understanding of the response of daily precipitation to major climate modes (e.g. Gershunov and Cayan 2003; Higgins et al. 2007). The current study should help elucidate the physical mechanisms that contribute to changes in the distribution of daily precipitation and so contribute to advances in climate prediction and projections.

The primary objective of this study is to improve our understanding of the variability of the frequency distribution of daily precipitation over the United States. This goal is achieved through the examination of daily precipitation data and other elements of the hydrological cycle, as well as aspects of the large-scale circulation. The effects of two major climate modes, ENSO and MJO, are considered. The objectives of this work are:

- To investigate how the seasonal mean and frequency distribution of precipitation varies across the United States.
    - What regions are sensitive to changes in extreme precipitation?

    - What are the relationships between precipitation and related hydrologic fields such as precipitable water and moisture flux convergence?
- To examine the variability of the frequency distribution of daily precipitation dependent on large-scale climate modes, such as ENSO and the MJO.
    - How do these modes affect the climate, mean precipitation, and the precipitation frequency distribution over the United States?
    - How do other components of the hydrological cycle and their relationship with precipitation change with climate modes?

Chapter 2 provides a description of the primary data set and analysis methods of this work, and introduces the precipitation-related fields. Chapter 3 describes the seasonal frequency distribution of daily precipitation. Chapter 4 investigates the ENSO-related modulation of the frequency distributions of precipitation and its related fields during winter. In Chapter 5, MJO-related modulations during winter are examined. Chapter 6 presents a summary, conclusions, and planned future work.

Chapter 2: Data and Method

The methodology employed for this dissertation is a statistical analysis of the North American Regional Reanalysis (NARR) products, with the goal of identifying the relationship between the modes of variability and the precipitation frequency distribution. Other variables associated with precipitation are included in the analysis. The first section of this chapter discusses the NARR dataset, the primary source of data for this study. The second section reviews the gamma distribution and the method used for estimating the gamma distribution parameters, and the third section defines the precipitation-related variables that have been examined.

2.1 Data

This study will use the North American Regional Reanalysis (NARR) 1979-2005 data to study the statistical properties of daily rainfall over the conterminous United States. NARR is a long-term, dynamically consistent, high-resolution, high-frequency, atmospheric and land surface hydrology dataset for the North American domain (Mesinger et al. 2006). The regional reanalysis was developed with the 2003 version of the Eta model and its associated Eta Data Assimilation System. The Eta model is coupled to the Noah land surface model (Ek et al. 2003) that simulates land surface temperature, the components of the surface energy balance and the surface water balance, and the evolution of soil temperature and soil moisture, both liquid and

frozen. The NARR computational grid has a 32-km horizontal resolution, with 45 layers in the vertical (Mesinger et al. 2006).

The model does not assimilate precipitation directly but instead derives latent heating profiles from precipitation analyses and from this forcing produces the NARR precipitation (Lin et al. 1999). Over the continental U.S., the daily analysis is disaggregated to hourly using temporal weights derived from a 2.5º by 2.5° analysis of hourly rain-gauge data (see Shafran et al. 2004; Mesinger et al. 2006). There is an extremely high agreement between NARR and observed precipitation over land, even over the complex western U.S. topography, and thus NARR should have a good representation of extreme events (Mesinger et al. 2006). In fact, a recent independent examination of NARR precipitation, including extremes, found it to be superior to global reanalyses over the contiguous U.S. (Bukowsky and Karoly 2007). To further understand the character of the daily precipitation distribution, we will examine several associated fields, including moisture flux convergence, precipitable water, and the convective available potential energy.

2.2 Frequency distribution

The frequency distribution of daily precipitation is usually positively skewed, as the bulk of daily precipitation events are lighter events, with fewer heavy and extreme events. This pattern can be described using the gamma distribution, which is bounded on the left by zero and positively skewed (Wilks 1995). The gamma distribution can be characterized by two parameters: shape (α), and scale (β), which

succinctly describe a wide range of distributions (Wilks 1990). The shape parameter, α, describes the skewness of the gamma distribution. Low values of α (less than 1) give a distribution with the maximum of variable *x* occurring at $x = 0$. The "exponential distribution" is described by $\alpha = 1$, and high values of the shape parameter ($\alpha > \sim 20$) mean a distribution approaching the Gaussian or normal distribution (Thom 1958). The parameter β scales the distribution by stretching or shrinking it along the x-axis. Some examples of these parameters appear in Fig. 2.1 (from Husak et. al 2007), which shows six gamma distributions with different shape and scale parameters and the same mean.

The expression of the gamma distribution is given by

$$f(x) = \frac{(x/\beta)^{\alpha-1} e^{-x/\beta}}{\beta \cdot \Gamma(\alpha)} \tag{2.1}$$

where α is the shape parameter, β is the scale parameter, and $\Gamma(\alpha)$ is the gamma function, defined by the definite integral

$$\Gamma(\alpha) = \int_0^\infty e^{-t} t^{\alpha-1} dt \tag{2.2}$$

The gamma function can be solved or estimated from tables; see Wilks (1995) for discussion. The shape and scale parameters need a statistical estimation. For this

study, the Maximum Likelihood Estimators method (MLE) of Thom (1958) was used. Thom's MLE method defines:

$$A = \ln(\bar{x}) - \frac{\sum_{i=1}^{n_p} \ln(x_i)}{n_p} \tag{2.3a}$$

$$\hat{\alpha} = \frac{1}{4A}\left(1 + \sqrt{1 + \frac{4A}{3}}\right) \tag{2.3b}$$

$$\hat{\beta} = \frac{\bar{x}}{\hat{\alpha}} \tag{2.3c}$$

where n_p is the number of non-zero values, $\bar{x}$ indicates the time mean, and $\hat{\alpha}$ and $\hat{\beta}$ are the estimated parameters. Thom's estimators have a slight bias, even for a large sample size, but this bias is generally of little importance for $\alpha > 0.1$ (Shenton and Bowman 1970).

The shape and scale parameters cannot be computed for days with zero precipitation (see Eq. 2.3a), thus they were estimated for the distribution of "wet-day" precipitation, following Watterson and Dix (2003) and Husak et al. (2007). Various studies have used different thresholds for defining a wet day; for example, all non-zero values (Groisman et al. 1999; Husak et al. 2007), 0.0017 mm d^{-1} in Watterson and Dix (2003), or 1.0 mm d^{-1} in Higgins et al. (2008). Here we use a threshold of 0.1 mm d^{-1}, which allows for the generation of a reasonably realistic gamma

distribution. The definition of a third parameter, the wet-day frequency, complements the use of the gamma distribution. This parameter is defined as

$$frequency = \frac{n}{N} \tag{2.4}$$

where n is the number of days with precipitation greater than 0.1 mm d^{-1} and N is the total number of days in the record. This parameter allows for the interpretation of the gamma distribution in the context of seasonal total precipitation.

As it follows from Eq. 2.3c, the product of the shape and scale parameters is equal to the mean of the non-zero observations. Hence, if the mean remains constant and α decreases, β must increase, and vice versa. Husak et al. (2007), looking at monthly rainfall in Africa, defined regions as "shape-dominated" (large α, small β) or "scale-dominated" (small α, large β). Shape-dominated regimes tend to define areas that typically receive consistent rainfall accumulation in the historical record, with fewer extreme events. Scale-dominated areas have large variance in comparison to the mean, with more extreme events (Husak et al. 2007). Figure 2.2 illustrates this relationship with a simple graphic. The choice of a higher wet-day threshold (e.g. 1.0 mm d^{-1}) lead to a higher wet-day mean and a lower frequency, and the shape parameter is larger. However, the scale parameter, and in particular the relationships between the scale and shape parameters and between the scale and the mean, are not greatly affected by the choice of a different wet-day threshold. Thus, the various

regions of the country retain their scale- or shape-dominance, and the scale parameter remains a useful diagnostic for extreme precipitation.

Daily precipitation distributions have a smaller shape parameter (are more strongly skewed) than the distribution of monthly values. However, the basic conceptual relationship between α and β remains the same. Husak et al. (2007) used this concept to locate areas of Africa where occasional drought may have an impact on agriculture, and possibly match crops and infrastructure to the precipitation regime. While most U.S. infrastructure and agriculture are already in place, the gamma parameters can identify areas sensitive to heavy and extreme precipitation. Shape- and scale-dominated regions will respond differently to changes in climate. For example, scale-dominated areas may depend on a few heavy/extreme events to replenish reservoirs, and so a season without these heavy events could lead to low water resources. Conversely, shape-dominated regions may be able to tolerate a season with fewer extremes, but could be vulnerable to prolonged dry spells.

2.3 Definition of terms

In the upcoming chapters, the precipitation gamma distribution is examined, and then this technique is applied to other variables of the overall hydrologic cycle, including precipitable water and moisture flux convergence (MFC), to better relate the statistics of precipitation to the statistics of the hydrologic cycle terms. Precipitation is one component of the hydrological cycle, and it is influenced by the available water in the atmospheric column; the two factors that comprise this are

precipitable water and MFC. Precipitable water is the total atmospheric water vapor contained in a vertical column. It is given by

$$W = \frac{1}{g}\int_{toa}^{p_0} q\,dp \tag{2.5}$$

where g is the acceleration of gravity and q is the specific humidity, and the integral is performed from the top of the atmosphere to the surface. The vertically-integrated MFC, the amount of water vapor brought in to a vertical column of atmosphere by the wind, is given by

$$MFC = -\frac{1}{g}\int_{toa}^{p_0} (\nabla \bullet Vq)\,dp \tag{2.6}$$

where V is the horizontal wind field, and the integral is again performed from the top of the atmosphere to the surface.

The convective available potential energy (CAPE) is the amount of energy available to an ascending parcel of air. It is calculated by

$$CAPE = \int_{LFC}^{EL} g\frac{T_v(z) - \overline{T}_v(z)}{\overline{T}_v(z)}\,dz \tag{2.7}$$

where $T_v(z)$ is the virtual temperature profile of the ascending air parcel, $\overline{T}_v(z)$ is the virtual temperature profile of the environment, and the integral is performed from the level of free convection (LFC) to the equilibrium level (EL) (Bluestein 1993).

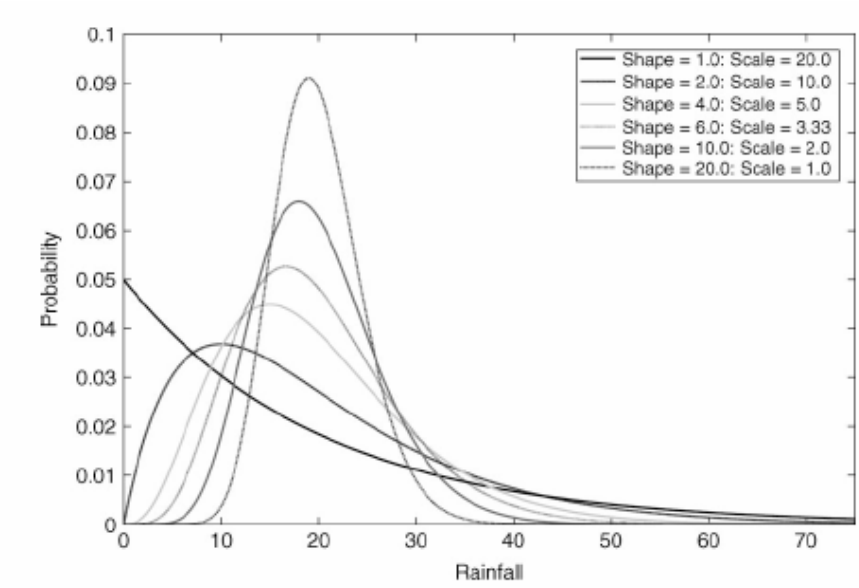

Figure 2.1: Six unique gamma functions, all with mean equal to 20. From Husak et al. (2007), Figure 1.

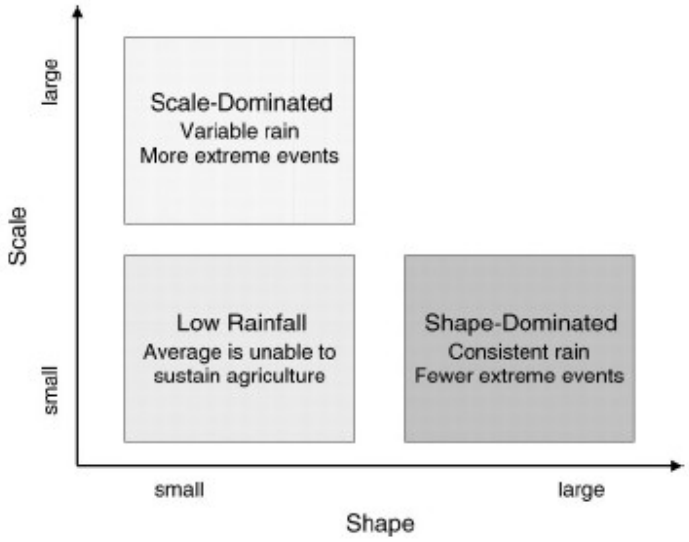

Figure 2.2: Conceptual depiction of shape- and scale-dominated frequency distributions. From Husak et al (2007), their Figure 2.

Chapter 3: Seasonal Frequency Distribution of Daily Precipitation

This chapter examines the spatial structure and seasonal evolution of the frequency distribution of precipitation and related fields. The gamma distribution is employed to examine the mean seasonal distribution of precipitation, and of several precipitation-related fields. The frequency distribution of daily precipitation reveals the dependence of the seasonal mean on light, medium, and extreme events. Regions where extreme precipitation dominates the mean seasonal total are identified, and the seasonal progression is examined in both the daily precipitation statistics and the statistics of the various precipitation-related fields. Decadal changes in the NARR data are examined in the last section of this chapter.

3.1 Daily precipitation

The mean wet-day precipitation amount, frequency, scale parameter (β), and shape parameter (α) for winter, spring, summer, and fall (JFM, AMJ, JAS, OND) are shown in Fig. 3.1. The wet-day frequency patterns obtained from NARR for the four seasons (Fig. 3.1, second column) are similar to those from observations as presented by Higgins et al. (2008, reprinted here as Fig. 3.2), although the frequency from our analysis is slightly higher than theirs, which is attributable to their use of a threshold of 1.0 mm d^{-1} versus ours of 0.1 mm d^{-1}.

In general, shape-dominated areas (large α, small β) will feature more consistent rain with fewer extreme events, while scale-dominated areas (large β,

small α) will receive more precipitation from extreme events. (See Chapter 2 for details of the gamma distribution.) According to the first row of Fig. 3.1, the winter precipitation patterns are very similar to the scale parameter patterns; i.e., where the mean wet-day precipitation is high, there is a greater contribution from extreme events. For example, the average wet-day amount of precipitation in California and along the West coast, which is high relative to most of the rest of the country, is dominated by heavy events, and the pattern of the scale parameter reflects this. Further analysis reveals some important regional differences, however. Both Northern California and the Pacific Northwest have relatively high average daily precipitation amounts (Northern California is ~ 10-12 mm d^{-1}, and the Pacific Northwest around 12-14 mm d^{-1}). Both areas have similar scale parameters, but the distribution of daily rainfall is less skewed (illustrated by the greater shape) in the Pacific Northwest than in Northern California, meaning the Pacific Northwest owes its greater average daily amount to more consistent, lighter events.

Other areas of note include the northern Plains and Great Lakes regions, and western New York State. These areas receive most or all of their winter precipitation as snow, and are shape-dominated. The Atlantic and Gulf of Mexico coasts are also scale-dominated regions where heavy precipitation from winter storms contributes to the higher mean. Central Arizona has a relatively high mean precipitation, governed strongly by heavy events, as seen in the high scale parameter. Overall, the winter gradient between low and high precipitation (from the central and northern Plains to the southeast) is also echoed in the scale parameter.

During spring (Fig. 3.1, row 2), the wet-day frequency decreases across most of the western U.S., and increases somewhat over the eastern U.S. The mean wet-day precipitation over the West coast has decreased as the winter storm track weakens, and increased in the central U.S., likely due to the onset of the Great Plains Low-Level Jet (GPLLJ), which transports moisture from the Gulf of Mexico into the interior of the U.S. in the warmer months (Bonner 1968; Higgins et al. 1997b). This region sees variable rain with more heavy events and is strongly scale-dominated. The Ohio River and Appalachian Mountain regions, as well as the northern Rockies, are dominated by consistent rainfall with fewer extreme events, illustrated by the relatively high shape parameter. The driest part of the U.S. in spring is southern Arizona, with a wet-day frequency less than 10% and a mean wet-day amount less than 2.0 mm.

By summer (Fig. 3.1, row 3), the effect of the GPLLJ in transporting moisture away from the Gulf coast into the central Plains can be seen in the inland peak in wet-day precipitation. In this region and a small area of northwest Washington State, variable rains and more extreme events provide the dominant contribution to the mean in summer. In both the wettest and the driest areas of the country (the southeast and the west, respectively), the daily mean is dominated by more frequent light and moderate rainfall days, i.e., shape-dominated.

The North American Monsoon usually begins in June, and is characterized by a reversal in the surface winds along the Gulf of California (Badan-Dangon et al. 1991), increased precipitation in western Mexico and southern Arizona and New

Mexico (Douglas et al. 1993), and reduced precipitation in the central U.S. (Higgins et al. 1997a; Barlow et al. 1998). The core Monsoon is located in northwestern Mexico, and only its fringes affect the southwest U.S. Therefore, the monsoon does not appear as a strong feature in the average wet-day amount, although it appears in the higher frequency of rainfall in Arizona, New Mexico, and Colorado. The Monsoon contributes consistent light and moderate rains to this area (Douglas et al. 1993) and this is illustrated by the strong dominance of the shape parameter.

The monsoon has ended by fall (Fig. 3.1, row 4), and the GPLLJ has decayed as well (Bonner 1968). Fall precipitation patterns over much of the U.S. appear largely similar to winter. Exceptions include the higher mean wet-day rainfall amount along the East coast, and a greater dependence on extreme precipitation events through the Midwest and around the Great Lakes region in fall than in winter. Overall, however, the similarities between fall and winter suggest that, regarding the daily precipitation frequency distribution, the transition between the warm season and the cold season occurs faster than the transition between the cold season and the warm season (i.e., spring).

3.2 Precipitation-related factors

To better understand the dynamic and thermodynamic factors related to precipitation, the precipitable water, vertically integrated moisture flux convergence (MFC), and convective available potential energy (CAPE) from NARR have been analyzed for the same period as precipitation. Precipitable water and moisture flux

convergence provide information about the amount of water in the atmospheric column available for precipitation, and CAPE represents the work done on a parcel of air by the environment as the parcel is accelerated upward (see Section 2.3 for definition of terms). All fields have been analyzed for wet days only, i.e., the same dates over which the mean precipitation (Fig. 3.1) was examined, and then a gamma distribution was fitted to MFC and precipitable water. This section will describe the seasonal characteristics of each factor and its relationship with precipitation.

The mean seasonal patterns of precipitable water are presented in Fig. 3.3. During winter (Fig. 3.3, first row), the western half of the country has low precipitable water. The eastern half features a roughly zonal pattern, with the maximum of around 30 mm occurring in southern Florida and Texas, and decreasing steadily northward. Only in the northeast are daily values of precipitable water relatively variable, as illustrated by the higher scale parameter in this area. The southernmost portions of the country see a nearly Gaussian distribution of daily precipitable water values around the mean, but toward the north the bulk of daily values are in the lighter range, and the distribution becomes more skewed. Although higher precipitable water is present in areas of higher precipitation (West coast and southeast), the maxima are not co-located. The areas with more variable and extreme precipitation, i.e., the scale-dominated precipitation areas, do not have a correspondingly high precipitable water scale parameter, implying that extreme precipitation does not have a strong link with high daily precipitable water.

Together with precipitation, vertically integrated moisture flux convergence (MFC) is one of the most relevant variables when analyzing the atmospheric water balance. The overall winter patterns of mean MFC and its scale parameter (Fig. 3.4, first row) closely resemble those of precipitation (Fig. 3.1). However, the winter pattern of the shape parameter of the MFC distribution generally does not bear a strong resemblance to that of precipitation across the country. Over the regions that receive the heaviest wet-day precipitation—in California and along the West coast and the central Gulf coast—MFC is strongest (maximum ~ 20 mm d^{-1}), and the gradient between the strongest MFC (southeast) and the weakest (northern Plains) is similar to the precipitation gradient. As well, the southernmost areas of the country, south Florida and south Texas, have lower mean precipitation and weaker MFC relative to the central Gulf coast. Central Arizona also has stronger MFC relative to its surrounding areas, similar to the precipitation. Regions of strong mean MFC are characterized by variable convergence with more daily values in the strong and extreme range, as illustrated by the similarity between the mean and the scale parameter.

Compared to winter, spring has much higher values of precipitable water across the country (Fig. 3.3, row 2). The general spatial pattern of the mean wet-day precipitable water is very similar to that of winter, with lower values at higher latitudes and elevations. The gamma distribution parameters show a distinct gradient between the Great Lakes region, with more high daily values of precipitable water (scale-dominated) and the south, with more consistent precipitable water and fewer

high daily values (shape-dominated). While the spring mean precipitable water has a similar pattern to that of mean precipitation, the precipitable water shape and scale do not have a strong resemblance to the precipitation gamma distribution parameters. Hence, while their spring seasonal mean patterns are similar, the variability of daily precipitation does not appear to be strongly related to the variability of precipitable water.

Mean MFC in spring has a maximum of around 12 mm d^{-1}, substantially less than during the winter, and the overall spatial pattern shows less variability (Fig. 3.4, row 2). The country can be roughly divided into the west (weak MFC) and east (strong MFC) regions. According to Fig. 3.4, MFC is generally characterized by lower variability (lower scale) of daily values, resulting in a shape-dominated distribution. Still, the area of strongest MFC, along the Mississippi River, has a larger scale parameter, or in other words, more variability. Central Florida, which has moderate mean MFC in the spring, exhibits consistent MFC with fewer high daily values (higher shape). Spatially the overall MFC pattern is similar to precipitation (Fig. 3.1, row 2), with stronger MFC corresponding to higher rainfall. Also, areas of the country that receive more variable and extreme rainfall (Fig. 3.1) have more frequent high daily values of MFC.

In summer, the precipitable water mean continues to increase (Fig. 3.3, row 3), especially in the eastern half of the country. The effect of the North American Monsoon can be seen in the southern portions of Arizona; however, this area of high precipitable water extends further west, into southern California, than does the

enhanced precipitation signal of the NAMS (e.g. Douglas et al. 1993). The mean precipitable water is not dependent on high daily values: the shape parameter over much of the country is greater than 20, indicating the frequency distribution is close to Gaussian.

During summer the mean MFC maxima, again around 12 mm d^{-1}, occur in the northern Midwest and along the northeast Atlantic coast (Fig. 3.4, row 3). This pattern likely reflects the moisture transport from the Gulf of Mexico into the central U.S. by the GPLLJ (Higgins et al. 1997b; Mo et al. 2005). The other area of relatively strong MFC is in southern Arizona, likely due to the North American Monsoon (Berbery and Fox-Rabinovitz 2003; Becker and Berbery 2008). Like winter and spring, the scale parameter of summer MFC corresponds well to the scale parameter of precipitation (Fig. 3.1). For the most part, summer MFC over the southwest and the Florida peninsula is shape-dominated, meaning that the daily values exhibit less variability.

The pattern of autumn precipitable water (Fig. 3.3, row 4) is very similar to that of winter, with somewhat stronger magnitude—a maximum of about 40 mm in Florida and southern Texas. The eastern half of the country, except for Florida, is scale-dominated, with high daily values contributing substantially to the mean. The West coast shows higher precipitable water, owing to consistent daily values of precipitable water (shape-dominated). Florida shows a much more normal precipitable water frequency distribution than the rest of the country. In autumn, the gradient between strong MFC in the southeast and weak MFC in the northern Great

Plains has strengthened (Fig. 3.4, row 4), the pattern of mean wet-day MFC is very similar to winter, and most of the pattern of mean MFC is due to the presence or absence of strong daily values.

Lastly, the seasonal evolution of CAPE was examined (Fig. 3.5). The frequency distribution of CAPE does not fit a gamma distribution well, and therefore only the wet-day mean has been analyzed. CAPE is relatively weak over most of the country during winter, except over the warmer regions of south Texas and Florida where somewhat stronger values are noticed. CAPE is largest in spring and summer. During spring, an area of stronger CAPE intrudes from the Gulf of Mexico into the central Great Plains. This area is at its strongest in the summer, and resembles the spring and summer precipitable water mean (Fig. 3.3). Also in summer, the effect of the North American Monsoon can be seen in an area of higher CAPE in southern Arizona, again similar to the summer precipitable water mean. During autumn, CAPE drops to very low values over most of the country, with the exception of the Gulf of Mexico coast.

3.3 Decadal variability in the 1979-2005 record

Future projections using coupled GCMs with a business-as-usual climate policy scenario predict increases in the proportions of precipitation contributed by extreme, heavy, and moderate daily totals, and decreases in the contribution from light events, when comparing the end of the 20th century to the end of the 21st century (Wilby and Wigley, 2002; Semenov and Bengtsson, 2002). These studies have found

that the scale parameter is more sensitive (spatially and temporally) than the shape parameter to increased atmospheric CO_2 from anthropogenic contributions (Wilby and Wigley 2002; Semenov and Bengtsson 2002; Groisman et al 2001). Wilby and Wigley (2002) explain the importance of this result, saying "changes in mean wet-day amounts are strongly correlated with, and hence primarily determined by, changes in the scale parameter." Their projections suggest that the proportion of total precipitation derived from extreme and heavy events will continue to increase relative to moderate and light precipitation events, and the absolute extremes of daily precipitation amount are also projected to increase.

While 27 years is an insufficient time period to identify a climate trend, it is of value to analyze the decadal changes within the NARR record. This achieves two goals: the identification of variations between the first half (1979-1992) and second half (1993-2005) of the record, and testing the relative sensitivities of the mean and scale parameter. The change in the mean between the first and second halves of the precipitation record is shown in Fig. 3.6. The mean, scale, and shape parameters are shown as the percent change from the first half to the second, and the frequency (col. 2) is the increase in percentage points (e.g. an increase from 40% to 46% is 0.06 on the scale). During all four seasons, there is a general pattern of lower (higher) wet-day mean precipitation in the western (eastern) portion of the country during the second half of the record.

In winter (row 1), the Rocky Mountains have the largest reduction in the wet-day mean. This area accumulates snowpack during the winter, which provides an

important source of water to many areas when it melts in spring and summer. The frequency of precipitation, on the other hand, increases. This fact, the decrease in the scale parameter, (which indicates fewer heavy and extreme events), and the general increase in the shape, all point to more-frequent, lighter-to-moderate daily precipitation over the Rockies during the second half of the record. Also during winter, the Midwest and Atlantic coast regions have a somewhat higher scale parameter and a lower shape, suggesting the distribution has become more skewed, with a greater contribution of extremes.

Spring (Fig. 3.6, row 2) does not have large areas with decadal changes in the mean, except for a portion of the southern Plains, which can be attributed to an increase in heavy/extreme events (increased scale). The substantial increase in the wet-day frequency over much of the north and west, including the northern Rockies, is for the most part *not* accompanied by large changes in the scale or shape of the distribution. Similarly, the decreased frequency in the south does not change the gamma distribution, implying that while these regions may have more or fewer wet days during the second half of the record, the proportion of light, moderate, and extreme events is generally unchanged.

Summer (Fig. 3.6, row 3) shows a clear divide along the Rocky Mountains: to the west, decreased mean wet-day precipitation and extremes, and a less-skewed shape. To the east of the Rockies, there is an increased wet-day mean, with a greater contribution of extremes, and a more-skewed shape to the distribution. The change in the frequency, on the other hand, shows a decreased number of days with

precipitation throughout much of the country, with the exception of the northern Rockies, where the frequency increases. The changes over the northern Rockies are similar in structure to those during winter (see above).

In autumn (Fig. 3.6, row 4), the increased frequency over the Rockies is accompanied by decreases in the mean and both the scale and shape parameters, meaning a more-skewed distribution with fewer extremes: the increased frequency in the NARR record is due to very light daily precipitation. However, there is a lot of variation in scale and shape trend patterns over this region, meaning the changes in the frequency distribution are localized.

Turning to the precipitation-related variables, no change was found in the precipitable water mean or gamma distribution parameters (not shown). The changes in winter MFC in the NARR record (Fig. 3.7) show some regions with increased mean daily MFC, with the greatest increase over California. The scale and shape of the MFC gamma distribution exhibit stronger changes: much of the west, which has little trend in mean MFC, shows a reduced number of strong daily values and an increase in weaker convergence. A similar pattern occurs in the south. The winter changes in mean MFC do not have a strong resemblance to the changes in mean daily precipitation (Fig. 3.6). However, the decadal changes in the scale parameter of both MFC and precipitation are more similar, although MFC changes are weaker. This pattern appears in spring, summer, and fall as well: weak trends in mean MFC, stronger changes in the scale and shape parameters, and similarity between the trend in MFC and precipitation scale parameters. Hence, while mean MFC may not change

substantially over the course of the NARR record, the frequency and intensity of strong daily MFC does, and where it increases (decreases) extreme precipitation increases (decreases).

3.4 Summary

The frequency distribution of precipitation has a seasonal dependence that was examined in detail, and can be summarized as follows: during winter, the mean precipitation is dominated by daily heavy and extreme precipitation events, particularly in California and along the Gulf of Mexico coast. Winter mean daily precipitation in the Pacific Northwest, the highest winter mean in the country, has a contribution from extremes that is similar to that in California, but a greater contribution from light/moderate events. During summer, the southeastern U.S. mean precipitation is dominated by frequent light and moderate events, while over the Great Plains it is dominated by heavy and extreme events. The autumn precipitation mean and the frequency distribution are very similar to those of winter, suggesting a fast transition between the warm season and the cold season. Areas of the country that receive more variable and extreme rainfall throughout the year have more frequent large daily moisture flux convergence, suggesting a strong link with precipitation. This is unlike the frequency distribution of precipitable water, which does not appear to have similarities to the frequency distribution of precipitation. Comparing the second half of the NARR record (i.e., 1993-2005) to the first (1979-1992), there is a general pattern of lower (higher) wet-day mean precipitation in the

western (eastern) portion of the country in the second half of the record during all four seasons. The MFC field has its greatest decadal changes in the frequency and intensity of strong daily MFC, and where it increases (decreases) extreme precipitation increases (decreases).

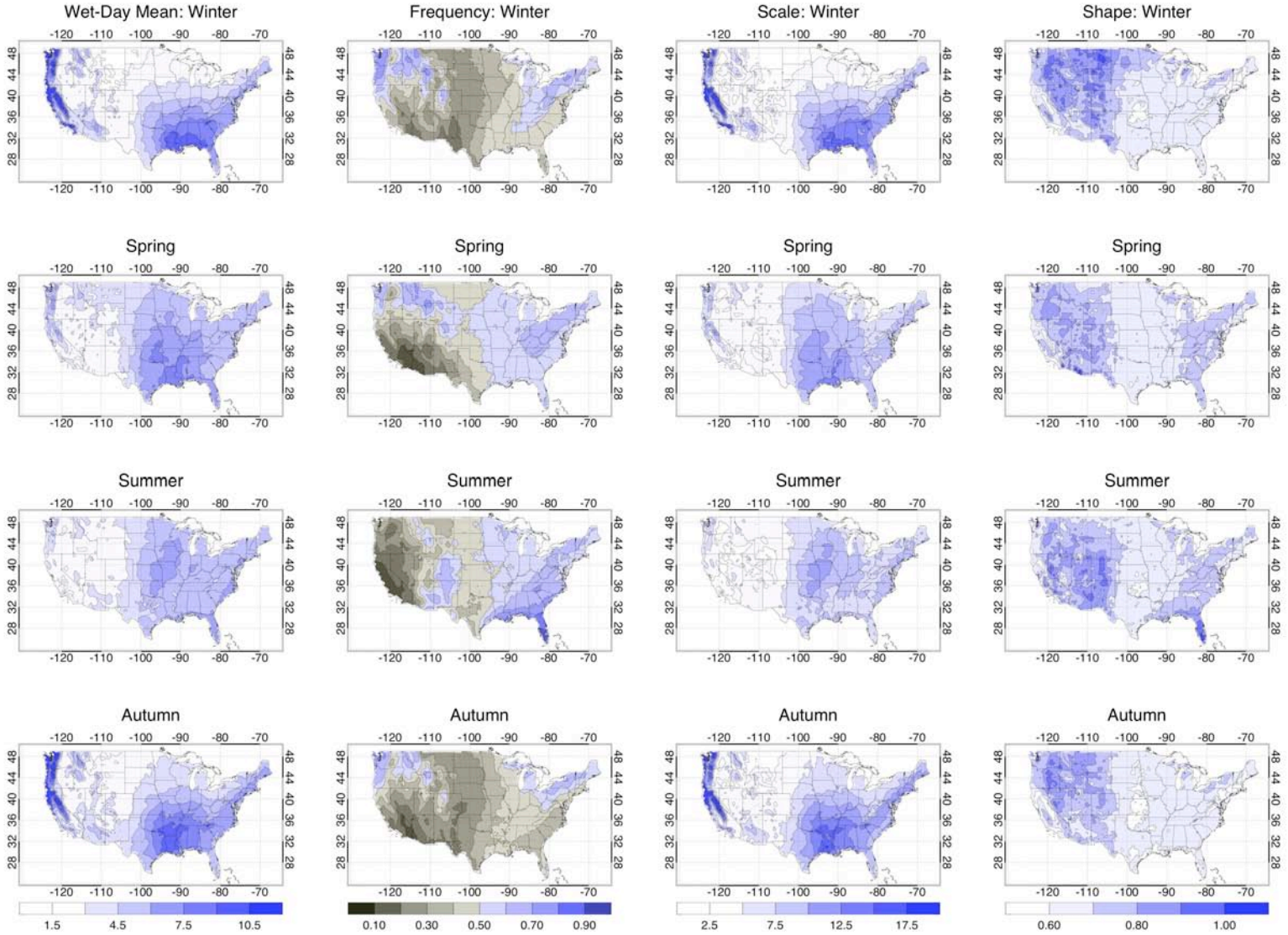
Wet-Day Mean: Winter
Frequency: Winter
Scale: Winter
Shape: Winter
Spring
Spring
Spring
Spring
Summer
Summer
Summer
Summer
Autumn
Autumn
Autumn
Autumn
-120 -110 -100 -90 -80 -70
48 44 40 36 32 28
1.5 4.5 7.5 10.5
0.10 0.30 0.50 0.70 0.90
2.5 7.5 12.5 17.5
0.60 0.80 1.00

Figure 3.1 (preceding page): Mean precipitation wet-day amount, frequency, and gamma distribution scale and shape parameters for winter (JFM), spring (AMJ), summer (JAS), and autumn (OND) over the contiguous United States, from NARR.

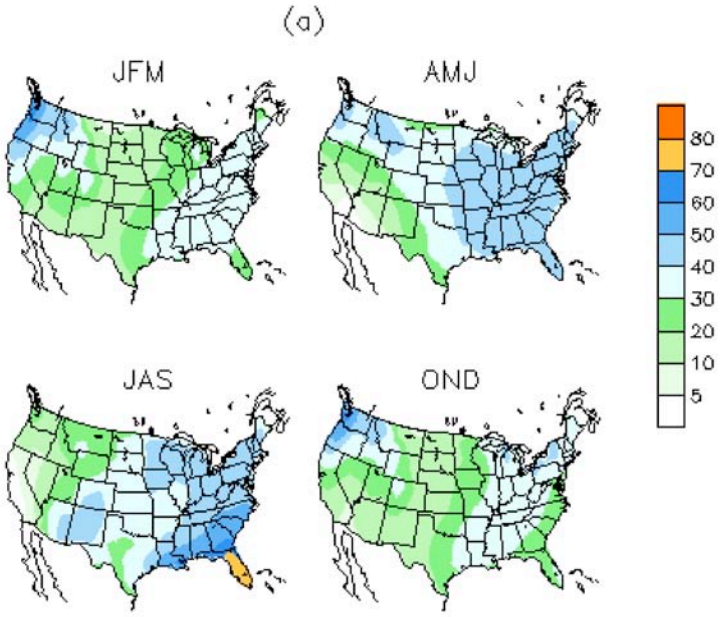

Figure 3.2: Average observed number of days per season with precipitation greater than 1 mm during 1981-2005. From Higgins et al. (2008) Figure 1.

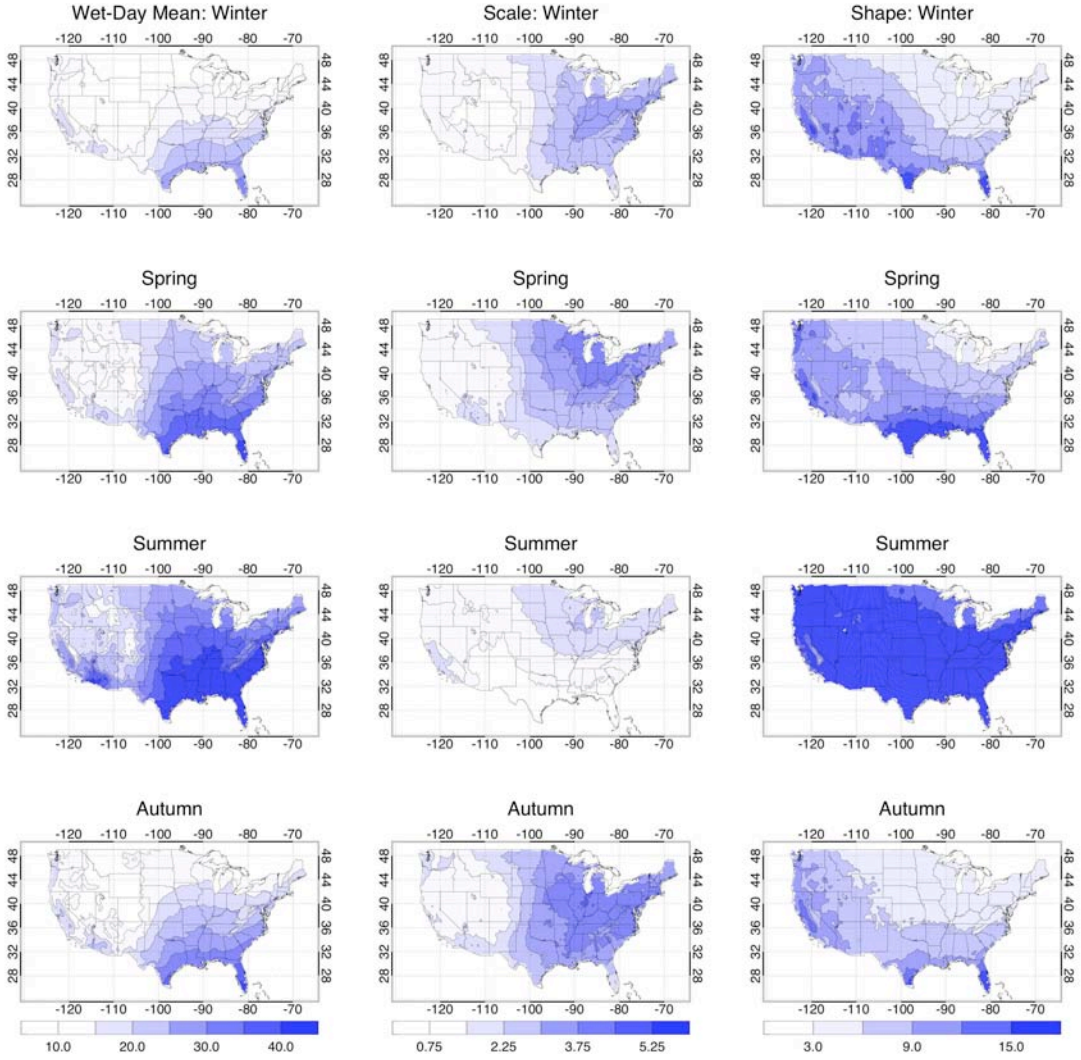

Figure 3.3: Mean precipitable water wet-day amount and gamma distribution parameters for winter, spring, summer and autumn, from NARR, 1979-2005.

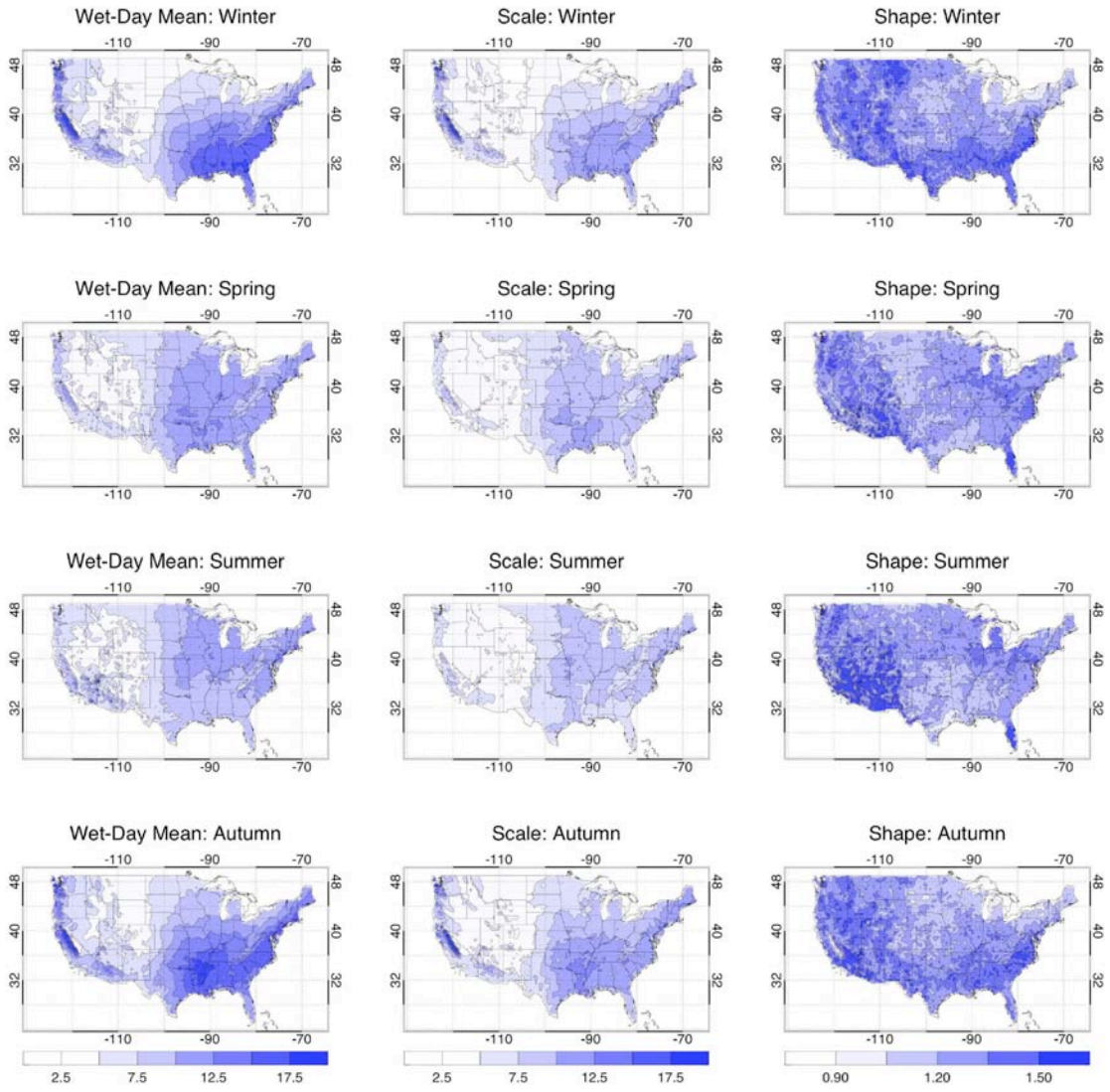

Figure 3.4: As in Figure 3.3, for moisture flux convergence.

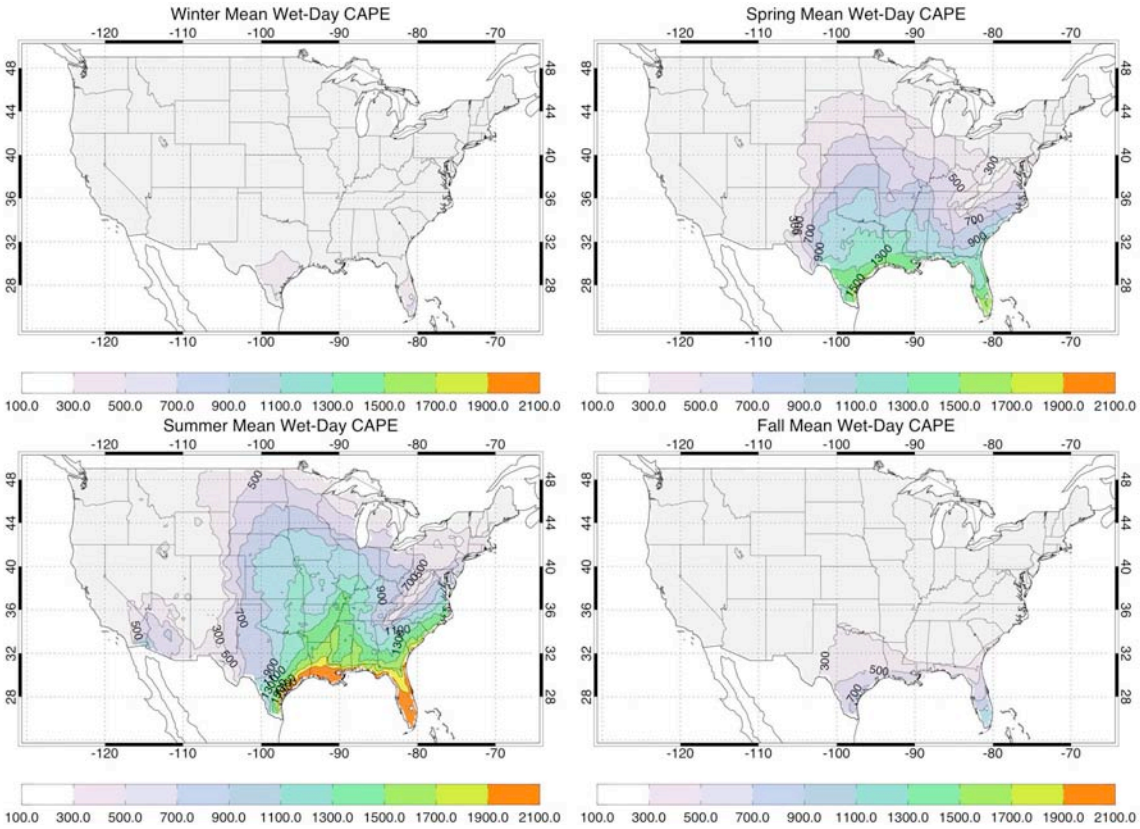

Figure 3.5: Mean seasonal convective available potential energy (CAPE), from NARR.

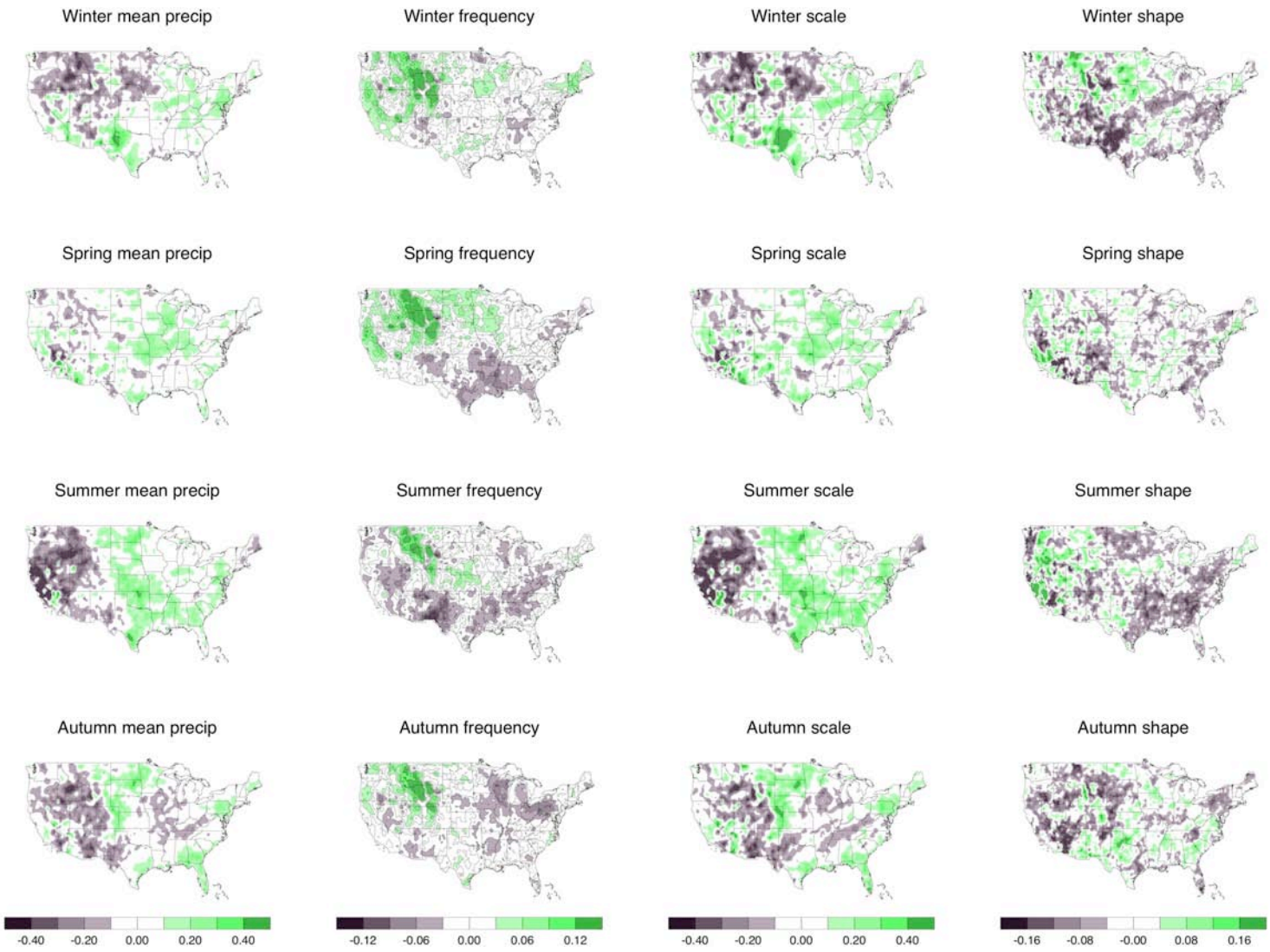
Winter mean precip
Winter frequency
Winter scale
Winter shape
Spring mean precip
Spring frequency
Spring scale
Spring shape
Summer mean precip
Summer frequency
Summer scale
Summer shape
Autumn mean precip
Autumn frequency
Autumn scale
Autumn shape
-0.40 -0.20 0.00 0.20 0.40
-0.12 -0.06 0.00 0.06 0.12
-0.40 -0.20 0.00 0.20 0.40
-0.16 -0.08 -0.00 0.08 0.16

Figure 3.6 (preceding page): Changes in precipitation between the first (1979-1992) and second (1993-2005) halves of the NARR record. Green (brown) indicates where values in the second half are greater (less) than the first.

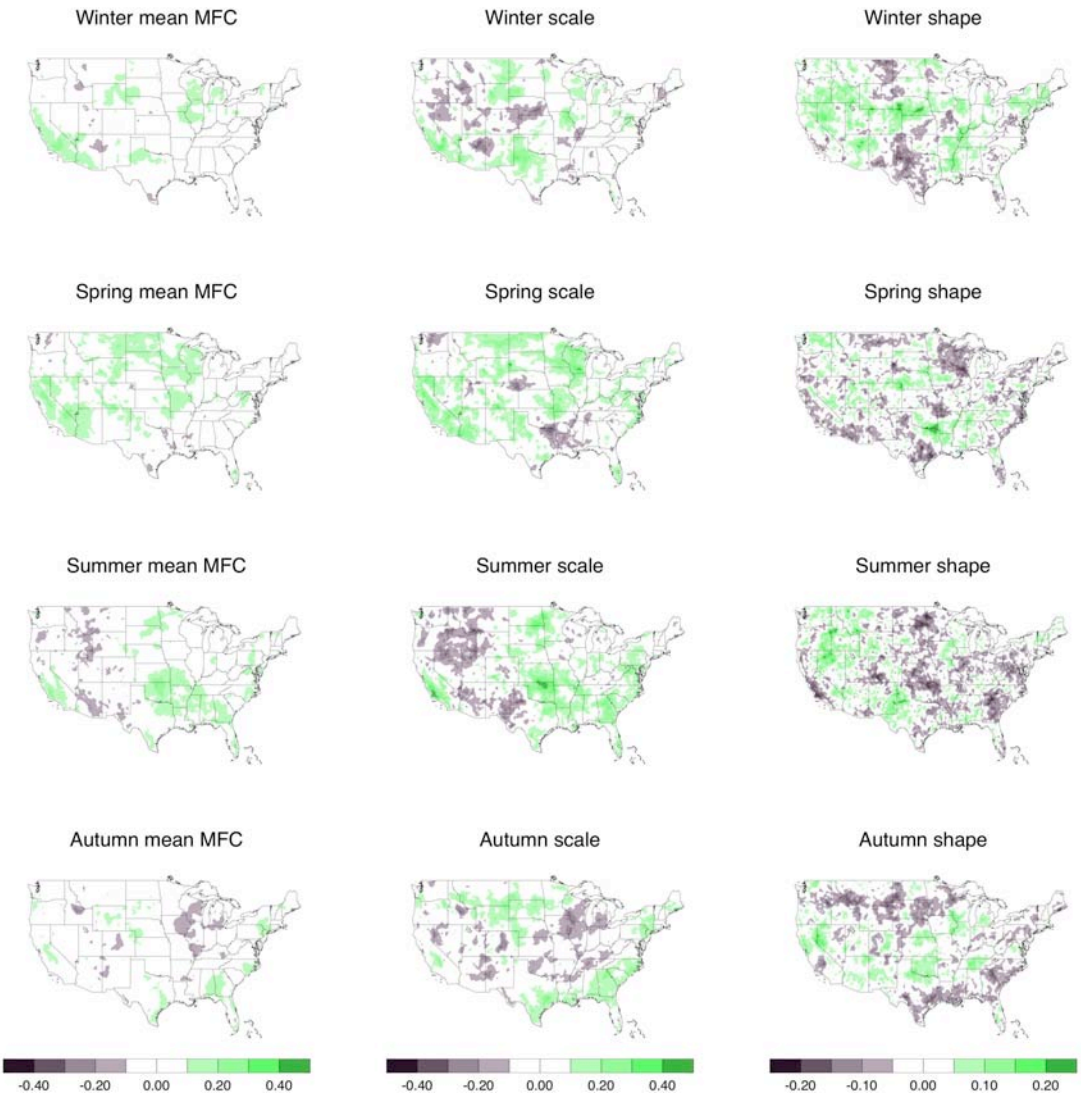

Figure 3.7: As in Fig. 3.6, for vertically-integrated moisture flux convergence.

Chapter 4: ENSO and the Statistics of Precipitation

This chapter examines the changes in the frequency distribution of precipitation during winter with the El Niño/Southern Oscillation (ENSO) climate mode, using the gamma distribution. The precipitation frequency distribution is known to be sensitive to changes in climate, and examination of its modulation by the well-known ENSO mode will reveal the response of shape- and scale-dominated regions (such as those identified in the previous chapter). The effect of the warm, cold, and neutral phases of ENSO are considered. The ENSO-related changes in the precipitation-related fields of moisture flux convergence and precipitable water are also studied. Spring and summer do not have a sufficient number of strong El Niño/La Niña events within the NARR record for this analysis. Examination of autumn ENSO-related modulation of daily precipitation (not shown) found only weak differences between the phases; hence, this discussion focuses on winter, which features several prominent ENSO-related effects.

4.1. Introduction

To the first order, the El Niño/Southern Oscillation (ENSO) is characterized by an abnormal warming of the equatorial Pacific, weakening or reversal of the trade winds, and a deepening of the thermocline in the Eastern Pacific. Through atmospheric teleconnections, the effects of ENSO are felt throughout the world. Anomalous warming of the Pacific waters results in increased convective clouds and

equatorial Pacific rainfall, leading to shifts of the subtropical jet stream (Hoerling and Kumar 2000 and references therein), excitation of waves, and modulation of midlatitude storm tracks, all of which lead to temperature and precipitation anomalies in the midlatitudes (Hoerling and Kumar 2000; Nakamura et al. 2004).

Earlier studies have found linkages between ENSO and wet conditions in the west and central regions of the United States (Ting and Wang 1997; Higgins et al. 1999; Barlow et al. 2001). Recent research has found that ENSO, which has significant effects on seasonal average precipitation and surface temperature in various regions of North America (e.g. Ropelewski and Halpert 1986, 1996), also affects the character of daily precipitation. According to Schubert et al. (2005), La Niña years tend to produce considerably fewer extreme storms than El Niño years along the Gulf and East Coasts. Higgins et al. (2007) found that during winter the Southwest averages up to 15% more days with measurable (> 1 mm) precipitation per season during El Niño phases, compared to La Niña. On the other hand, the Pacific Northwest and Ohio Valley average up to 15% fewer wet days per winter season for El Niño than for La Niña. During summer, the northern U.S. averages up to 15% more wet days per season during El Niño, compared to La Niña (Higgins et al. 2007).

Gershunov (1998) found for Northern California that, on average, La Niña winters tend to experience more frequent drizzle and less frequent heavy rains, while during El Niño winters the frequency of all rain events tends to increase, including both heavy and light rains. However, the greatest difference between El Niño, neutral, and La Niña phases in California is seen in the heavy and extreme rainfall

events (Gershunov 1998). Looking at the Ohio-Kentucky-Tennessee region, Gershunov (1998) found El Niño winters were associated with a strong and consistent decrease in the frequency of very heavy rainfall events, while La Niña winters in this region saw average rainfall conditions. The Eastern Gulf Coast experiences a higher frequency of precipitation in the entire range during El Niño and lower frequency in the cold phase (Gershunov 1998). A predilection for enhanced storm activity in the Gulf Coast and East Coast regions during El Niño winters has been seen in both observations and simulations (Schubert et al. 2005). In general, the strongest ENSO signals are in the heavy tail of the precipitation PDF (Gershunov 1998).

The effects of ENSO are not limited to the warm and cold phases. In particular, there are documented differences between El Niño and the neutral phase as well as between La Niña and the neutral phase. For example, during the warm phase of ENSO wintertime precipitation in several regions of the United States shows a higher frequency of heavy and extreme rainfall compared to the cold and neutral phases; during the cold phase Northern California experiences more light rain days and fewer heavy events than average (Gershunov 1998). Along the west coast of the United States, the largest fraction of extreme precipitation events occurs during a neutral winter before onset of the warm phase (Higgins et al. 2000b).

4.2 ENSO phase identification

In order to examine the changes in the seasonal distribution of daily precipitation due to low frequency variability associated with ENSO, the Oceanic

Niño Index (ONI), compiled by NOAA's Climate Prediction Center (CPC), is employed. The index is computed from three-month running values of SST departures from average in the Niño 3.4 region. El Niño is characterized by a positive ONI greater than or equal to +0.5°C, and La Niña is characterized by a negative ONI less than or equal to -0.5°C. This index can be found on the CPC website, http://www.cpc.ncep.noaa.gov/products/analysis_monitoring/ensostuff/ensoyears.shtml. A portion of it is reprinted here as Fig. 4.1.

The CPC ENSO index has been used to identify the five strongest El Niño (warm phase) and five strongest La Niña (cold phase) winters in the NARR record (see Chapter 2, section 2.1 for discussion of the NARR dataset). To confirm that the ten winters (five each El Niño and La Niña) used for the current analysis are representative of the typical atmospheric patterns of each phase, the NARR 200 hPa zonal wind was examined (Fig. 4.2). The strong Pacific jet stream of the warm phase is clearly visible in the left panel. The weaker jet stream of the cold phase, which is positioned further north than during the warm phase, can be seen in the right panel. This is consistent with previous studies (Arkin 1982; Ropelewski and Halpert 1986, 1996) that show that the extended Pacific jet stream characteristic of the warm phase leads to wetter-than-mean conditions in the south and warmer conditions in the north, while the weaker, further-north Pacific jet stream of the cold phase tends to bring wetter conditions to the northwest.

4.3 ENSO modulations during winter

a. Precipitation

The differences between El Niño and La Niña winters for mean wet-day precipitation, frequency, and the gamma distribution scale and shape parameters are presented in Fig. 4.3 (see Chapter 2, section 2.2 for discussion of the gamma distribution). The values in Fig. 4.3 have been normalized by the mean of the ten winters (El Niño and La Niña). To consider the potential hydrologic effect of ENSO-modulated precipitation change, several basins at sub-continental scales are examined (see boundaries in Fig. 4.3a). According to Fig. 4.3a, the southwest U.S. during El Niño has a mean wet-day precipitation about 80% greater than during La Niña. This is likely due to the extended Pacific jet stream and amplified storm track characteristic of an El Niño winter (Kousky et al. 1984; Nakamura et al. 2004). Mean precipitation increases by as much as 40-60% along the Gulf of Mexico and southeastern coast. Both the southwest U.S. and the Gulf coast are scale-dominated areas in winter, where the seasonal total is very sensitive to the contribution of heavy and extreme daily precipitation events. We also see up to 60% greater mean precipitation over the Lower Missouri River basin, in the central U.S. Reduced precipitation during El Niño is found over the Ohio River basin and to a lesser extent over the Texas panhandle, aligned with the Red River basin.

To assess the sensitivity of the ENSO composites, the mean of each individual winter was compared to the average of the ten years (not shown). While substantial

differences exist from year to year, for the most part it does not appear that one or two years dominate the composites. In four of the five El Niño years, the Lower Missouri River basin has a higher mean wet-day precipitation than the average, and all five La Niña years, it has a lower mean. The Ohio River basin mean wet-day precipitation is lower than the average in all five El Niño years, and higher in four of the five La Niña years. The mean in the southwest is higher in four of five El Niño years, and lower during four of the five La Niña years, but the strong positive in the El Niño winter of 1992 is likely the dominant effect. Shifts across the southeast are generally consistent, with a higher mean over most of the region during four El Niño years, and lower during four La Niña years. However, the shift to a lower mean during El Niño over the area of western Texas (see Fig. 4.3a) is dominated by the composite of one strong negative in 1995's El Niño and two strong positives in the La Niña winters of 1999 and 2000.

Figure 4.3b shows an increased wet-day frequency during El Niño over much of the south and southwest, again, likely attributable to the extended Pacific Jet Stream. This is also in general spatial agreement with Higgins et al. (2007), but we see an increase in wet-day frequency of greater than 60% in some areas of the southwest, a greater increase than in their study. As Higgins et al. (2007) use a higher wet-day threshold (1.0 mm d^{-1}), this may mean we see a greater increase in the number of days with very light precipitation (0.1 – 1.0 mm d^{-1}).

The spatial pattern of the changes of the scale parameter (Fig. 4.3c) are very similar to the changes in the mean spatial pattern (Fig. 4.3a), but substantially greater

in magnitude. For example, the Lower Missouri River basin has up to 60% increased daily mean precipitation, with an 80% or greater increase in extremes. This result is in agreement with Gershunov (1998) and Cayan et al. (1999) that found that the heavy/extreme range of daily precipitation magnitude is often more sensitive to ENSO phase than is the mean. The contribution to the mean precipitation from light and moderate daily events shows a small change between ENSO phases, i.e., the shape parameter, Fig. 4.3d, does not change much (note that the contour interval in Fig. 4.3d is smaller than in the other panels). The exception to this is the Lower Missouri River basin, where the shape decreases noticeably. This is a shape-dominated region when the winter mean is considered (Fig. 4.3.1), but during El Niño it becomes more scale-dominated. Several studies have found that changes in overall climate affect the scale of the gamma distribution of precipitation more than the shape (Wilby and Wigley, 2002; Watterson and Dix, 2003). Recalling that the mean is the product of the shape and scale, in general, this study finds that areas which experience an increased mean have a larger increase in the scale parameter, offset by a small decrease in the shape parameter.

While the El Niño – La Niña difference is a useful composite, earlier studies have found different effects between each of the phases and the neutral state (e.g. Higgins et al. 2000b), and an examination of the relative effects of the warm and cold ENSO phases on precipitation allows a greater understanding of the composite. To this end, the comparison of each phase to the non-ENSO mean is shown in Fig. 4.4. As the response of the gamma distribution parameters holds to the pattern seen in Fig.

4.3 (that is, the change in the scale parameter is of the same sign and a stronger magnitude than the change in the mean, with attendant smaller change in the shape), only the mean and frequency are shown in Fig. 4.4. This analysis reveals that mean precipitation in the central U.S. and along the southeastern coasts is higher than the mean during El Niño and lower than the mean during La Niña. However, the difference in the southwest is largely due to a decrease during La Niña (Fig. 4.4, top right), with little change appearing between El Niño and the neutral state (top left). The difference in Ohio River basin mean precipitation is mostly due to a decrease during El Niño compared to the neutral state. On the other hand, the change over northern Texas is primarily an increase in mean precipitation during La Niña over the neutral state. The lower panels of Fig. 4.4 demonstrate that the shifts in wet-day frequency in the southwest represent both an increase in frequency during El Niño and a reduction in La Niña.

To illustrate the frequency distribution shifts between the warm and cold phases, Fig. 4.5 presents the histograms of five points around the country. Table 1 contains the mean, scale, and shape parameters corresponding to the distribution that fit each of these histograms. Four of these areas, Southwest California (Fig. 4.5a), the Pacific Northwest (Fig. 4.5b), the Great Plains (Fig. 4.5c), and Florida (Fig. 4.5d), have greater mean precipitation during El Niño, compared to La Niña. Of these, nearly all of the heavier precipitation events occur during El Niño, and the scale parameter is accordingly greater. Southwest California, the Pacific Northwest, and the Great Plains all have a greater increase in the scale than in the mean, offset by a

smaller decrease in the shape. Florida owes all the increased mean during El Niño to extreme events. Fig. 4.5e shows the opposite case: the Ohio River Valley has fewer extreme events during El Niño than during La Niña, and these account for a lower mean daily precipitation.

b. Precipitation-related factors

The ENSO-related effects on the frequency distribution of precipitable water and moisture flux convergence (MFC) were examined for the same time period as the previous section. (Please see Chapter 2.3 for a review of precipitable water and MFC.) The mean precipitable water (Fig. 4.6a) exhibits very little change between El Niño and La Niña. The most noticeable pattern is an increase in precipitable water over the northern half of the country and a small part of Maine. This area sees about a 20% increase in mean wet-day precipitable water during El Niño compared to La Nina.

Figure 4.6 also depicts the change in the precipitable water gamma distribution scale and shape parameters. It is instructive to look at Figs. 4.6b and 4.6c at the same time: the change in scale and shape parameters between the two ENSO phases are of nearly the same spatial pattern and magnitude and of opposite signs. Where the scale decreases over much of the west during El Niño, the shape increases: in other words, there is a decreased contribution of high precipitable water daily values to the mean and an increased contribution of low values of precipitable water to the mean. Along the Gulf of Mexico coast, the opposite pattern appears, with an

increased contribution of high precipitable water and a more skewed distribution during El Niño.

The changes seen in precipitable water between the warm and cold ENSO phase do not appear to correspond to the patterns seen in precipitation (Fig. 4.3). In fact, the areas that show the greatest change in mean wet-day precipitation amount between the two phases do *not* show a noticeable change in either the precipitable water mean daily amount or in the gamma distribution parameters. Rather, looking at the normalized change in precipitable water scale and shape parameters (Figs. 4.6b and c), we see a long stretch of the country from the Northwest along the Rocky Mountains and into the southern Great Plains that feature less-variable daily precipitable water values during El Niño. This area for the most part shows little change between the ENSO phases in mean daily precipitation (Fig. 4.3a) or in extreme precipitation (Fig. 4.3c).

The moisture flux convergence is a more relevant term to understand the changes in the precipitation distribution. Unlike precipitable water, the pattern of change in mean wet-day MFC between El Niño and La Niña (Fig. 4.7) resembles that of mean precipitation (Fig. 4.3), although the magnitude of the change in MFC over most of the country is about half that in precipitation. For example, Southern California, where the mean wet-day precipitation increases more than 60% between the two ENSO phases, exhibits an increase in MFC of about 20-40%. When the MFC of each phase was individually compared to the non-ENSO state to examine the

relative effects of the warm and cold phases (not shown), the results were very similar to those of precipitation (see the discussion of Fig. 4.4).

The change in MFC extremes (as represented by the scale parameter, Fig. 4.7b) is greater than the change in the mean, suggesting that the tail of the MFC distribution, (i.e., strong and extreme convergence), are more sensitive than the mean to changes in climate, similar to precipitation. However, like the mean, the magnitude of the change in the MFC scale parameter is about half that of the precipitation scale, throughout the country. The shape of the MFC distribution (Fig. 4.7c, note smaller contour interval in this panel) shows little change between El Niño and La Niña, confirming that the most substantial contribution to the change in mean MFC is from the extremes rather than in the overall distribution, in agreement with the behavior of the precipitation shape parameter.

4.4 Summary

During winter many regions of the U. S. have a daily precipitation frequency distribution that has a strong dependence on ENSO variability. The southwest and central U.S., particularly the Lower Missouri River basin, exhibit a mean daily precipitation as much as 80% greater during El Niño, compared to La Niña. The increase over the Gulf of Mexico and southeastern coast is on the order of 40-60%. On the other hand, reduced daily mean precipitation during El Niño is found over the Ohio River and Red River basins and, to a lesser extent, over northern Texas. Most areas that see a large change in the daily mean precipitation between ENSO phases

have a change in heavy and extreme daily events that is greater than the change in the mean (for example, a 60% greater mean during El Niño, and 80% greater scale parameter). This is offset by a small decrease in contribution to the mean from lighter and moderate events, seen in the shape parameter.

The pattern of change in mean wet-day MFC between El Niño and La Niña resembles that of mean precipitation, although the MFC does not change as much as precipitation. Similar to precipitation, the change in MFC extremes is greater than the change in the mean, suggesting that the frequency of strong convergence is more sensitive than the mean to changes in climate. The variability of daily precipitation does not appear to be strongly related to the variability of precipitable water: areas that show the greatest change in mean wet-day precipitation between the two phases do not show a noticeable change in either the precipitable water mean daily amount or frequency distribution.

TABLE 1

	SW California	Pacific NW	Great Plains	Florida (west)	Ohio River Valley
	El Niño				
Mean	10.3	21.0	3.8	7.8	4.8
Scale	16.2	29.5	6.1	12.5	7.5
Shape	0.63	0.71	0.62	0.62	0.64
	La Niña				
Mean	5.4	16.3	1.7	4.8	7.8
Scale	8.0	20.1	2.0	7.9	13.4
Shape	0.68	0.81	0.83	0.61	0.58

Table 1: Mean and gamma distribution scale and shape parameters corresponding to the histograms in Figure 4.5.

Year	JFM	AMJ	JAS	OND		Year	JFM	AMJ	JAS	OND
1979	0.0	0.1	0.2	0.5		**1993**	0.4	**0.8**	0.4	0.2
1980	0.3	0.3	0.0	0.0		**1994**	0.3	**0.6**	**0.6**	**1.2**
1981	-0.4	-0.3	-0.3	-0.1		**1995**	**0.9**	0.2	-0.3	**-0.7**
1982	0.1	**0.6**	**1.0**	**2.2**		**1996**	**-0.7**	-0.2	-0.2	-0.3
1983	**2.0**	**1.0**	-0.2	**-0.9**		**1997**	-0.3	**0.9**	**2.0**	**2.5**
1984	-0.3	-0.5	-0.2	**-1.0**		**1998**	**2.0**	0.4	**-1.0**	**-1.3**
1985	**-0.8**	**-0.7**	-0.4	-0.2		**1999**	**-1.2**	**-0.8**	**-0.9**	**-1.4**
1986	-0.4	-0.1	**0.5**	**1.1**		**2000**	**-1.5**	**-0.7**	-0.3	**-0.7**
1987	**1.2**	**1.0**	**1.6**	**1.3**		**2001**	**-0.5**	-0.1	0.1	-0.2
1988	**0.5**	**-0.8**	**-1.1**	**-1.9**		**2002**	0.1	**0.7**	**0.9**	**1.5**
1989	**-1.5**	**-0.6**	-0.3	-0.2		**2003**	**0.8**	-0.1	0.4	0.6
1990	0.2	0.3	0.4	0.3		**2004**	0.2	0.3	**0.8**	**0.9**
1991	0.4	**0.6**	**0.9**	**1.4**		**2005**	**0.5**	0.5	0.0	-0.4
1992	**1.7**	**1.1**	0.2	0.0						

Figure 4.1: Historical El Niño (red) and La Niña (blue) episodes. From the Climate Prediction Center.

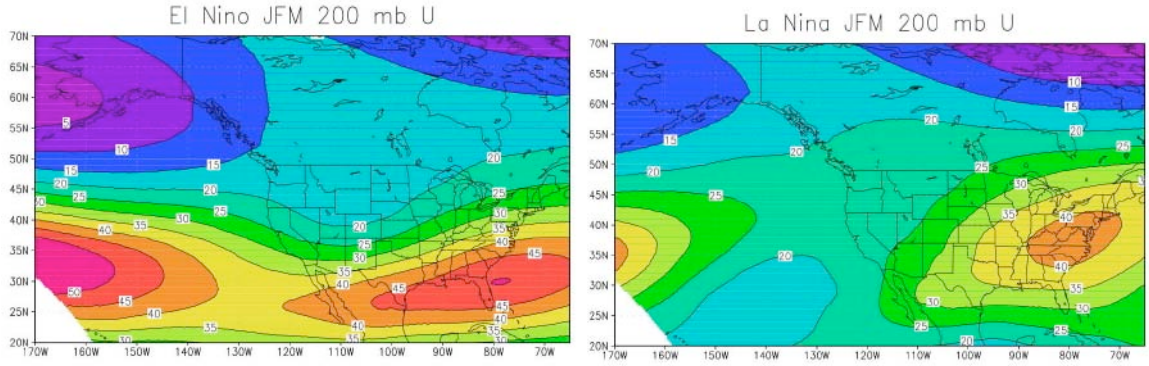

Figure 4.2: Mean 200 hPa zonal wind for the five El Niño winters (left) and five La Niña winters (right) that were examined for this study. The extended Pacific jet stream characteristic of El Niño is clear in the left panel, and the weaker Pacific jet stream of La Niña in the right.

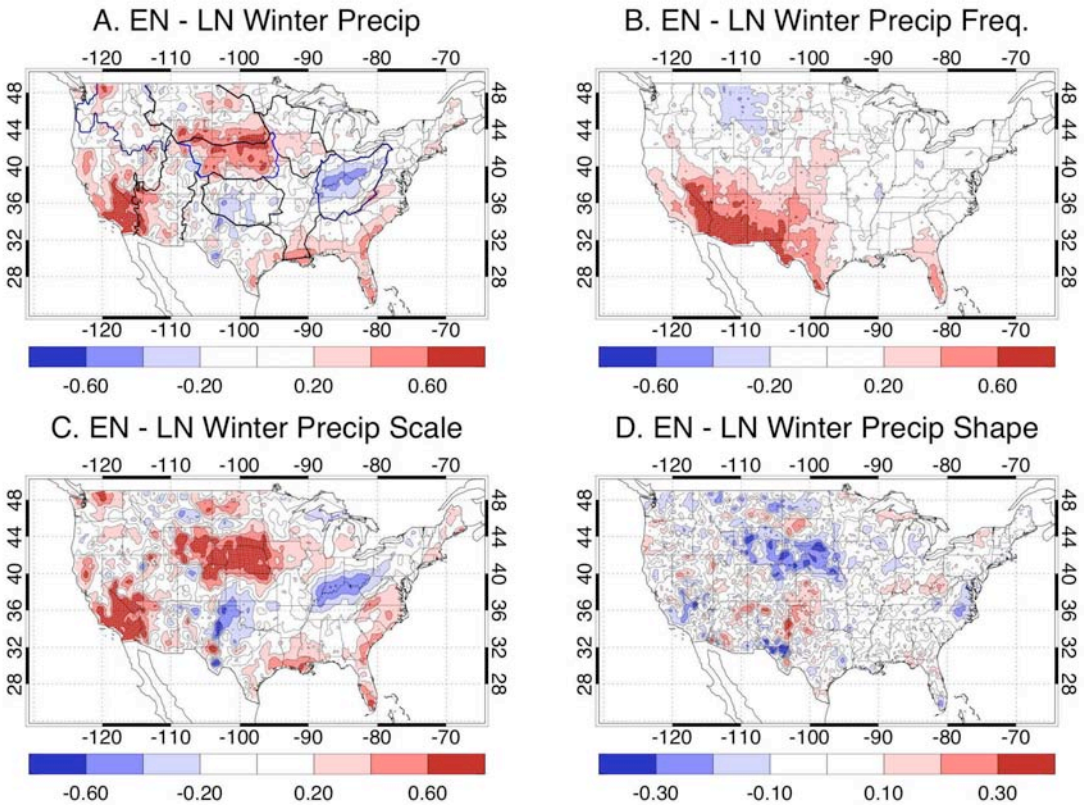

Figure 4.3: Normalized difference between El Niño and La Niña winters, for precipitation mean wet-day amount, frequency, and the gamma parameters. The contour interval is 20% for the mean daily amount, frequency, and the scale parameter, and 10% for the shape parameter. Panel A includes the contours of several hydrological basins.

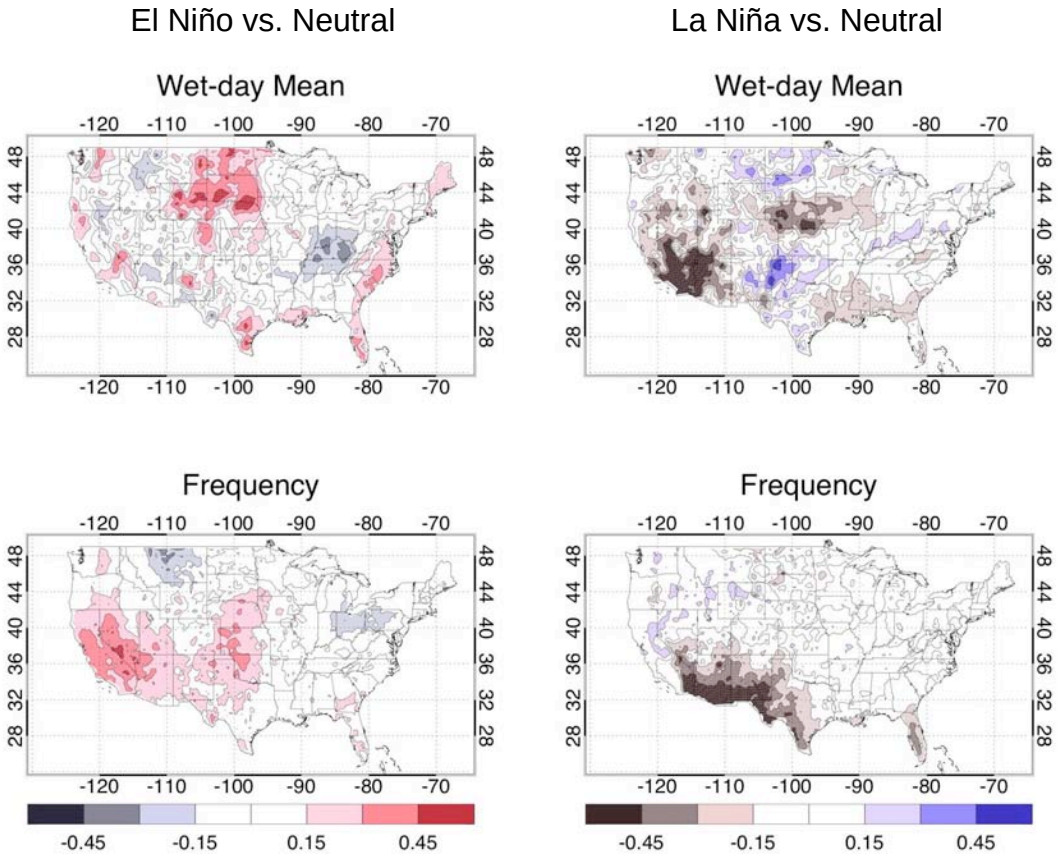

Figure 4.4: Normalized winter precipitation difference between El Niño and the neutral state (left column) and La Niña and the neutral state (right), for mean precipitation (top) and the wet-day frequency. The contour interval is 15%.

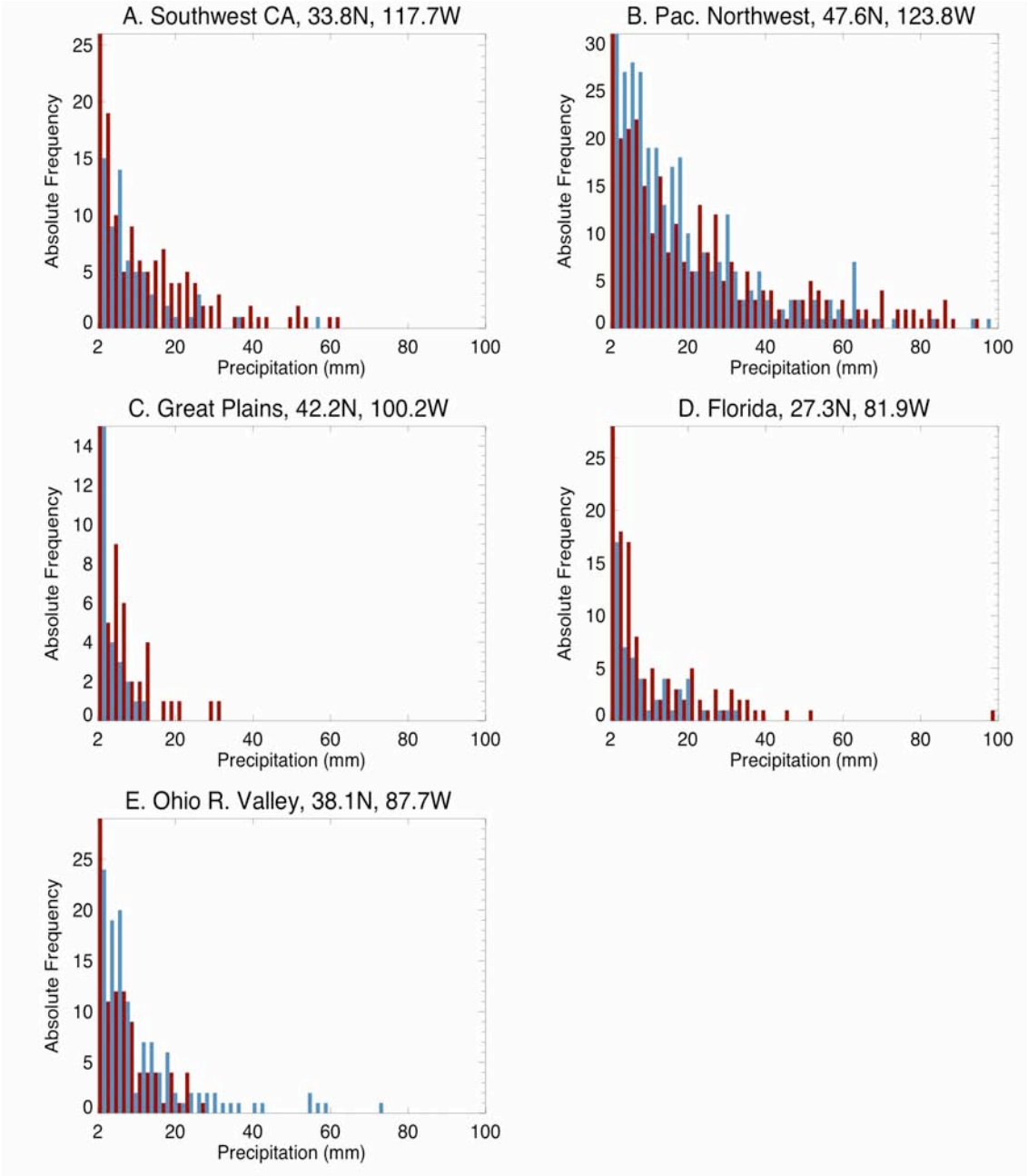

Figure 4.5: Histograms of El Niño (red) and La Niña (blue) precipitation for five points in the U.S: Southwestern California, the Pacific Northwest, the Great Plains, Florida, and the Ohio River valley. See Table 4.1 for mean and gamma distribution parameters corresponding to these distributions.

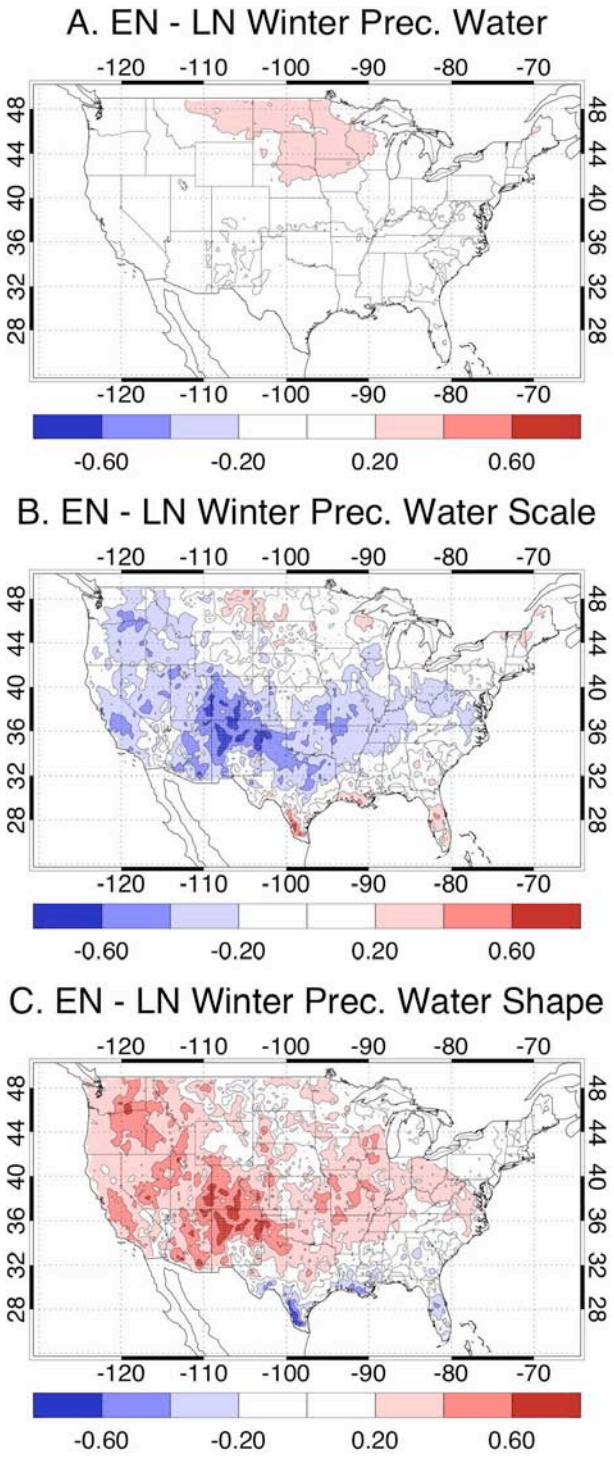

Figure 4.6: Normalized difference between El Niño and La Niña winters, for precipitable water mean wet-day amount and scale and shape parameters. The contour interval for all panels is 20%.

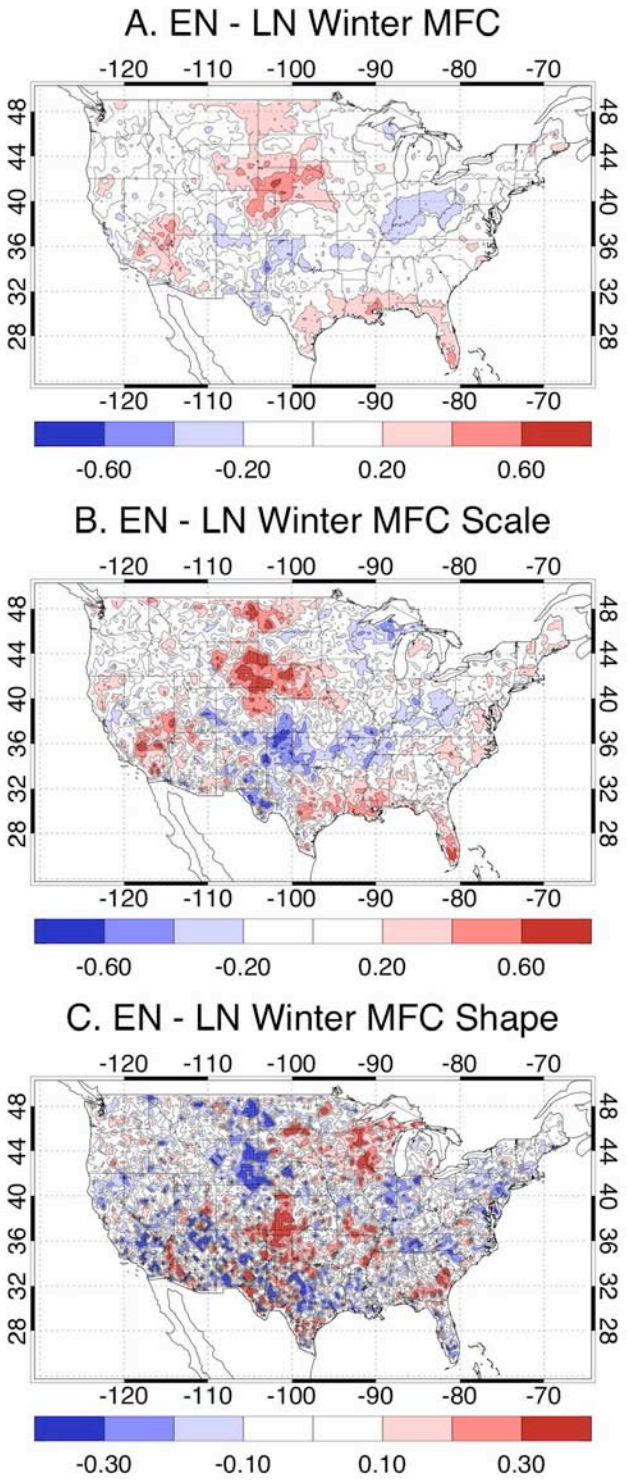

Figure 4.7: as in Figure 4.6, for moisture flux convergence. The contour interval for the mean daily amount and the scale parameter is 20%, and 10% for the shape parameter.

Chapter 5: Modulation of U.S. daily precipitation by the Madden-Julian Oscillation

The Madden-Julian Oscillation (MJO) and the precipitation frequency distribution are the focus of this chapter. The large-scale atmospheric conditions associated with an MJO event are examined. Next, MJO modulation of precipitation and its related variables, including precipitable water and moisture flux convergence is investigated, as well as the streamflow component of the hydrological cycle.

5. 1 Introduction

The Madden-Julian Oscillation (MJO) is a large-scale pattern of coupled atmospheric circulation and deep convection. First documented by Madden and Julian (1971, 1972), the pattern features a prominent area of enhanced deep convection and rainfall that propagates eastward along the equator through the Indian and Pacific oceans at a speed of about 5 m/s, flanked by areas of weak convection and suppressed rainfall to the east and west, with an intraseasonal period of between 30 and 90 days (see Zhang 2005, and references therein). The episodic behavior of this system has been characterized as pulse-like, rather than a true oscillation (Yano et al 2004). Many other climate variables are affected by the MJO, including water vapor, temperature, divergence, and diabatic heating, and exhibit variations coherent with the pattern of deep convection and enhanced rainfall (Zhang 2005).

The relatively slow eastward propagation of the system distinguishes the MJO from other tropical phenomena (Zhang 2005). To the immediate east of the center of convection are low-level convergence, ascending motions, and higher humidity, while immediately to the west are low-level divergence, descent, and lower humidity. This structure favors convective development in front of the system, and hence the eastward movement of the MJO (Zhang 2005).

The enhanced convection signal can be identified through satellite outgoing long-wave radiation (OLR) readings. Figure 5.1, from the CPC, shows the progression in the OLR anomaly. As the MJO propagates into the western hemisphere, the enhanced convection signal decreases. The MJO is still identifiable in the velocity potential (Fig. 5.2, from CPC) and upper- and lower-level winds, however, and continues to move eastward at an increased rate of approximately 10 m s^{-1} (Hendon and Salby 1994). As can be seen in the velocity potential field (Fig. 5.2), the upper-level divergence signal remains very clear throughout the cycle, and moves along the equator through the western hemisphere into the Indian Ocean.

The effects of this system reach far beyond the equatorial Indian and Pacific Oceans. Several studies have tied MJO activity to altered precipitation patterns in North America (e.g. Mo and Higgins 1998a,b; Jones 2000). As well, an increased frequency of extreme precipitation during active MJO has been identified in areas of Africa, the Middle East, eastern China, eastern South America, and parts of North America (Jones et al. 2004). Jones et al. (2004) found that, for areas with an MJO signal, the number of extreme precipitation events occurring during the active MJO

was about 40% higher than the number occurring during the quiescent phase. Some differences exist in the results of these studies, possibly due to different methods of MJO identification. For example, Jones (2000) finds a slight tendency for increased extreme events in California when enhanced convection is located over the Indian Ocean, while Mo and Higgins (1998b) finds no significant precipitation anomaly over the U.S. for this condition.

Most studies of MJO effects on the continental U.S. have focused on the western U.S. Mo and Higgins (1998b) found dry conditions in the southwest and wet conditions in the Pacific Northwest during winter when enhanced convection is located in the western Pacific. Higgins et al. (2000a) examined extreme 3-day precipitation events along the West coast during neutral winters prior to the onset of El Niño, and found a link between these events and the location of the enhanced tropical convection associated with intraseasonal oscillations (IO), including the MJO. During the precipitation events, the enhanced convection was located in Indonesia and the western Pacific. Bond and Vecchi (2003), looking at Oregon and Washington State during early winter, found as much as a 200% difference between precipitation rates, depending on MJO phase. They found that the increased precipitation in this region corresponded to when peak westerly wind anomalies of the MJO are located near the date line, versus when peak easterly wind anomalies are located between the Indian Ocean and the Pacific, and found substantial differences between “early winter” (OND) and “late winter” (JFM). Bond and Vecchi (2003) also looked at OND streamflow and flooding in western Washington and their

relationship with MJO phase, and found that half of floods occurred during one-eighth of the MJO cycle, and zero floods occurred during two consecutive phases. Interestingly, the peak flooding occurs during the phase before the peak in precipitation rate.

Several studies using the Rossby wave vorticity source have revealed links between tropical enhanced convection and midlatitude circulation in both hemispheres (Berbery and Nogues-Paegle, 1993; Higgins and Mo, 1997; Mo and Higgins, 1998b). IO-related enhanced convection centered over 5°S, 135°E (western Pacific) is associated with a stronger Hadley cell in the western Pacific: stronger 200 hPa divergence in the tropics, and stronger 200 hPa convergence in the midlatitudes (Mo and Higgins 1998b, see their Fig. 5.12b, reprinted here as Fig. 5.3a). This leads to midlatitude divergence and negative Rossby wave vorticity source anomalies in the central Pacific, and the Pacific jet stream (zonal winds above about 30 m s^{-1}, Fig. 5.3b) extends only to the central Pacific. As the enhanced convection system moves eastward, anomalous divergent outflow generates an anomalous Rossby wave vorticity source in the subtropics, the Pacific jet stream extends eastward and the North American jet stream moves northward (Figs. 5.3b,c). As the area of enhanced convection moves in the western hemisphere, the two jets connect (Mo and Higgins, 1998b; Higgins et al., 2000a). Figure 5.3e presents a CPC schematic of possible MJO interaction with the Northern Hemisphere jet streams and storm tracks.

Our understanding of the relationship of the MJO to other intra- and inter-annual climate modes is still developing. Recently, L'Heureux and Higgins (2008) found several links between the MJO and the Arctic Oscillation (AO). Specifically, the eastward propagation of the MJO signal is associated with a corresponding shift in the tendency and sign of the AO, and the surface temperature field shows similar responses to specific phases of both modes. Links to ENSO have been somewhat elusive, but very strong MJO activity has been observed prior to the peak of El Niño, with weak activity after the peak and during La Niña (Zhang and Gottschalk (2002); Zhang 2005 and references therein), and Hendon and Wheeler (2007) found MJO activity in the late boreal spring leads El Niño in the subsequent autumn-winter.

5.2 MJO indices and data

Over the past few decades, many different methods have been used to identify the presence, strength, and phase of the MJO, often relying on simultaneous or lagged OLR and wind measurements. Wheeler and Hendon (2004) established an MJO indexing method that is based on the first two empirical orthogonal functions (EOFs) of the combined fields of near-equatorially-averaged 850 hPa zonal wind, 200 hPa zonal wind, and satellite-observed outgoing longwave radiation (OLR) data. Before the EOFs are computed, ENSO variability and the 120-day mean of the most recent 120 days at each point are removed. The two EOFs, Real-Time Multivariate MJO series 1 and 2 (RMM1 and RMM2) make up the x- and y-axis of a phase space, and the state of the MJO is diagnosed as a point in this space (Fig. 5.4). The phase space

is divided into 8 regions, signifying the approximate location of the enhanced convective signal of the MJO; these phases are numbered 1-8. The magnitude of the index, $(RMM1^2 + RMM2^2)^{1/2}$, indicates the amplitude of the MJO: a magnitude of greater than one is considered a strong index. The panels in Figs. 5.1 and 5.2 are labeled with their approximate phase according to the Wheeler and Hendon (2004) index.

The CPC has recently developed an MJO event classification using a pentad-averaged version of the MJO index of Wheeler and Hendon (2004). The CPC classification system sets three criteria for an MJO event (L'Heureux and Higgins 2008; M. L'Heureux, personal communication):

i) The MJO index must have a magnitude greater than one for consecutive pentads.

ii) The phases must be in numerical order (to indicate eastward propagation), e.g. 5, 6, 7, 8, 1, and 2.

iii) The MJO must meet the first two criteria for more than five pentads and not remain stationary (in one phase) for more than four pentads.

As the Wheeler and Hendon (2004) indexing method relies on satellite-derived OLR, the event classification includes the satellite era only (1979—present). Fig. 5.5 provides a chart of 1979-2005 boreal winter (JFM) MJO events. Years are color-coded to indicate strong and weak El Niño (red and pink, respectively) and La Niña (blue and light blue). No color is accorded to ENSO neutral years. MJO phases present during each winter are marked with shading; this chart shows how many MJO

events occurred during each winter and what phases they spanned. For example, the winter of 1979, an ENSO-neutral year, included two MJO events, with phases 2-5 and 1-3.

This event classification was used to create composites for several fields of the NARR dataset (see Chapter 2 for a description of NARR). For example, all MJO Phase 1 days during JFM were isolated in the 1979-2005 NARR daily precipitation data. The Phase 1 mean was then calculated, and the seasonal mean (all 1979-2005 JFM) was subtracted to find the Phase 1 anomaly. Large-scale atmospheric circulation features related to the MJO were studied through the analysis of 200 hPa zonal and meridional wind. U.S. precipitation and temperature anomalies were examined, as well as the moisture flux convergence field, and the runoff anomaly was studied to look for links between MJO-related precipitation and high streamflow. Filtering has not been applied to the atmospheric and surface variables. During the JFM period of the 1979-2005 record, the MJO is active about 60% of the time. Each phase occurs with a frequency ranging from 5 – 10%. This translates to around 130-200 days per phase per season over the 27-year record.

5.3 MJO modulations during winter

The objective of this section is to describe how the Madden-Julian Oscillation modulates winter precipitation and the winter precipitation frequency distribution over the U.S. The first part of this section examines the large-scale atmospheric conditions during the eight phases of the MJO through analysis of upper-level winds,

surface temperature, and the moisture flux convergence. The second part studies the modulation of precipitation and other elements of the hydrological cycle, including moisture flux convergence and NARR-derived runoff.

a. Large-scale circulation

Several earlier studies (e.g. Mo and Higgins 1997a,b; Higgins et al. 2000b) discuss the relationship between enhanced convection in the tropical western Pacific and the extratropical winter jet stream and storm track. The composite winter 200 hPa zonal wind provides some insight into the activity of the subtropical jet stream (Fig. 5.6a). For clarity, the corresponding 200 hPa zonal wind anomalies are included as Fig. 5.6b. While only the eastern Pacific can be seen in these figures due to the domain of NARR, the eastward extent of the Pacific jet core is visible. In Phase 1, when MJO-related enhanced convection is located over Africa, the Pacific jet extends into the central Pacific, and is located close to its mean position. The anomaly pattern over North America during Phase 1 (Fig. 5.6b) shows the North American jet is displaced somewhat to the south of its mean position. During Phases 2-4, as the MJO signal propagates through the Indian Ocean and over the Maritime Continent, the Pacific jet's eastward extent is limited, due in part to the negative Rossby wave vorticity source anomaly generated by the MJO (see section 5.1) In Phases 5-7, the North American jet weakens, and moves northward, to a center over the mid-Atlantic coast; in Phases 6 and 7, the Pacific jet begins to extend eastward. When the enhanced convection signal of the MJO is in the Western Hemisphere (Phase 8), the

North American jet strengthens, and the Pacific jet extends eastward until it connects to the North American jet.

To study storm track activity with MJO phase, the 200 hPa meridional wind anomalies have been examined (Fig. 5.7). The mean meridional wind is small, and so large anomalies indicate storminess. As the enhanced convection signal of the MJO propagates eastward, a wave train, accompanied by westerly zonal wind anomalies, emanates from the tropical western Pacific and into the North Pacific, interacting with the storm track (Higgins et al. 2000a). The effect of this on North America is clearest during Phases 5 and 6 (Fig. 5.7), as the MJO signal moves off the Maritime Continent and through the western Pacific.

In Chapters 3 and 4, the link between the vertically-integrated moisture flux convergence (MFC) and precipitation was defined. The composite MFC anomalies, by MJO phase, are shown in Fig. 5.8. Most of the water vapor in the atmosphere is contained in the surface-to-700 hPa layer, so these composites give a picture of the lower troposphere. In the first three MJO phases, while the enhanced convection signal moves off Africa and through the Indian Ocean, MFC anomalies in the midlatitude eastern Pacific are mostly negative, and anomalies over the North American continent are generally small, with some substantial negative anomalies over the Pacific Northwest in Phases 1-2. In Phases 4 through 6, there is an alternating pattern of positive MFC anomalies in the central Pacific, negative anomalies near the West coast, and positive anomalies over the central U.S. As the enhanced convection moves over the dateline and into the western hemisphere

(Phases 7 and 8), weak positive anomalies form in the eastern Pacific, with negative anomalies over the U.S.

The standardized anomaly in the composite winter temperature field, by MJO phase, was also examined (Fig. 5.9). The standardized anomaly, computed by dividing the anomaly by the standard deviation of the sample, puts the anomaly in the context of the variance of the field. A standardized anomaly < 1 would indicate that the anomaly is less than one standard deviation. All of the standardized anomalies in the temperature field are fairly small (less than ~0.5), but some interesting patterns are revealed by the evolution through the MJO. Phases 2, 3, and 4 show little change over the country in the temperature field, with the exception of a small warm anomaly over New England in Phase 4. A warm anomaly appears in Phase 5 throughout the eastern half of the country. In Phase 6, the warm anomaly covers much of the Ohio River valley and the Southeast, and there is a small cool anomaly in the West. Phase 7 shows only a small positive anomaly in Arizona/New Mexico, and a cool anomaly in the Northwest. In Phase 8, a warm anomaly appears over most of the western half of the country, with the largest values in the northern Great Plains. The warm anomalies in Phases 5-8 may be related to the shifts in the North American jet core, which is weaker and displaced to the north of its seasonal mean during these phases (see Fig. 5.6b). L'Heureux and Higgins (2008), in their comparison of the MJO and the AO, composited Phases 2, 3, and 4 winter temperature anomalies and subtracted them from a composite of Phases 7 and 8, and found that the eastern (western) half of

the country was cooler (warmer) than the other half during Phases 2/3/4 than during Phases 7/8.

b. Precipitation

Modulation of the winter precipitation frequency distribution by the MJO is studied through analysis of the composite winter mean anomaly (Fig. 5.10), gamma distribution scale parameter, β (Fig. 5.11; see Chapter 2 for discussion of the gamma distribution), and wet-day frequency (Fig. 5.12). The scale parameter indicates the contribution to the mean from heavy and extreme precipitation events. The gamma distribution shape parameter, α, does not exhibit substantial variations and for simplicity is omitted. A black contour line in Fig. 5.10 indicates where the mean anomaly is significant at the 95% level, using a t-test. Based on the following results and those of others (e.g. Mo and Higgins 1998b, Higgins et al. 2000a) that show the major MJO-related effects on North America occur when the MJO is in Phases 5-8, the discussion is divided into "Phases 1-4" and "Phases 5-8".

i. Phases 1-4

For the most part, MJO Phases 1-4 do not feature large signals in the mean precipitation (Fig. 5.10), in keeping with earlier studies (e.g. Mo and Higgins 1998a,b) that found few effects on North America when MJO-related enhanced convection is located over Africa or the Indian Ocean. However, there are some interesting details that bear mention. Florida has a mean anomaly on the order of 1-

3 mm d^{-1}, and the southwest a significant anomaly on the order of 1 mm d^{-1}. Examination of the scale parameter (Fig. 5.11) reveals more about these anomalies. In Phase 1, the southern half of Florida has an increased scale parameter, indicating more precipitation events on the heavy and extreme end of the spectrum during this phase, likely contributing to the positive mean anomaly in this area. Also during Phase 1, a slight negative anomaly in the area of the Lower Mississippi is associated with a large decrease in the scale parameter (Fig. 5.11), indicating this area sees fewer heavy precipitation events during Phase 1 than the winter mean. Referring to the composite MFC anomalies (Fig. 5.8) for Phase 1, we find a strong resemblance between the MFC anomaly and the scale parameter anomaly, reflecting the link between strong MFC and extreme precipitation that was identified in Chapters 3 and 4 of this study.

Turning to the winter wet-day frequency anomaly (Fig. 5.12) for Phase 1, the southeast and portions of the southwest show small positive anomalies (~5-10 percentage points), and the northern half of Florida sees an increase of 10-15 points during this phase. This result tells us that the positive mean anomaly over all of the Florida peninsula seen during Phase 1 (Fig. 5.10) is due to different changes in the frequency distribution: the northern half has a higher frequency of daily precipitation, but does not have an increase in heavy/extreme events, while the southern half has more events on the heavy/extreme end of the spectrum, with a smaller increase in wet-day frequency. During Phase 1, the North American jet stream is centered further south than during the rest of the MJO cycle (Fig. 5.6), likely contributing to

the increased wet-day frequency and mean precipitation in the southwest and Florida. Both the position of the jet stream and the precipitation anomalies during Phase 1 bear a resemblance to the El Niño case (see Chapter 4, Figs. 4.2 and 4.3), although the jet stream during Phase 1 is substantially weaker than during El Niño.

Phases 2-4, when MJO enhanced convection is located over the Indian Ocean, do not show large anomalies in the mean precipitation field, although there are some fluctuations in the scale parameter along the west coast (Fig. 5.11). This is a strongly scale-dominated area (see Chapter 3, Section 2), meaning precipitation is highly variable, with many heavy and extreme events. The changes in the scale parameter for the most part are not accompanied by significant anomalies in mean precipitation. However, again the scale parameter anomalies correspond to the MFC anomalies (Fig. 5.8).

ii. Phases 5-8

During Phase 5, when the MJO enhanced convection is in the far western Pacific, the most prominent feature in the mean precipitation field is a large anomaly over the eastern and southern Plains, including Indiana, Mississippi, Arkansas, Oklahoma, and eastern Texas (Fig. 5.10). During this phase, the MJO enhanced convection signal is moving over the Maritime Continent, the jet core over North America (Fig. 5.6) is centered relatively far north, and the storm track activity is enhanced (Fig. 5.7).

This is the largest anomaly that appears over the U.S. during the entire MJO cycle. The magnitude of the anomaly over most of this area is between 2 and 3 mm d^{-1}. Also during Phase 5, significant negative anomalies in mean precipitation are present in the west over Northern California and part of Oregon, and in the east over Florida and the mid-Atlantic. This pattern is largely reflected in the scale parameter (Fig. 5.11), meaning the central U.S. has more heavy and extreme precipitation events during Phase 5 than the long-term average, and the west coast and Florida have fewer. The wet-day frequency (Fig. 5.12) is as much as 15-20 points higher during Phase 5 in the central and eastern Plains (the area with the large change in mean precipitation), and there is decreased wet-day frequency in Northern California, Oregon, and Washington State, as well as portions of the southeast.

In Phase 6, a positive mean anomaly of around 1 – 2 mm d^{-1} is evident over portions of the Midwest and South (Fig. 5.10). The storm track is still enhanced in Phase 6 (Fig. 5.7). The scale parameter (Fig. 5.11) also has an anomaly in the same area, indicating an increase in extreme events. The wet-day frequency (Fig. 5.12), on the other hand, does not have an anomaly over the Midwest and South. Also during Phase 6, eastern Washington State, which features a positive mean anomaly, does *not* show an anomaly in the scale parameter, telling us that this anomaly is not primarily due to an increase in extreme events. However, the wet-day frequency is higher than the long-term average over much of the Northwest, so this area is seeing more days with precipitation, but not more extreme one-day events. Phase 6 also shows an

increased mean and incidence of extreme events over New England, and decreased mean precipitation over Florida.

In Phases 7 and 8, the enhanced convection of the MJO has diminished, but the signal is still clear in the velocity potential field (Fig. 5.2), as it travels over the date line and into the Western hemisphere. The Pacific jet extends eastward, and in Phase 8 connects to the North American jet (Fig. 5.6). Also, the 200 hPa meridional wind anomalies (Fig. 5.7) show the storm track activity has relaxed. Precipitation anomalies in these two phases are mostly negative over the country. The exception to this is during Phase 7, when a small positive anomaly is located in the Midwest and South (Fig. 5.10).

Phase 8 has a large negative anomaly over California and western Oregon and Washington. Only a small portion of this area, along the Sierra Nevada mountains, shows an anomaly in the scale parameter, indicating that the decrease in the mean is not due to a large decrease in extreme events. The wet-day frequency during Phase 8 over most of the West is reduced by as much as 15 percentage points during Phase 8 (Fig. 5.12). For the Northwest, this means the frequency of days with > 0.1 mm precipitation declines from an average of about 60% to around 45%, while California's wet-day frequency declines from around 45% to 35% (see Chapter 3, Fig. 3.1 for seasonal means).

c. NARR-derived runoff

The composite winter runoff anomaly, by MJO phase, is presented in Fig. 5.13; the data source for this is the combined NARR surface runoff and baseflow. Areas shown are significant at the 95% level, using a t-test, and several hydrologic basins are outlined in black. Phases 1-3 show few appreciable anomalies. In Phase 4, a positive runoff anomaly appears in the area of the Ohio River basin. Phase 5 shows an anomaly pattern similar to that seen in the mean precipitation field (see Fig. 5.10): positive runoff in the area west of the Mississippi River, with a negative anomaly in Northern California and Oregon. Phase 6 shows the largest, strongest runoff anomaly, over the western Ohio River basin and eastern Lower Mississippi basin. This area has a positive anomaly in the mean precipitation, during Phase 6, and the scale parameter anomaly shows this area receives more daily precipitation events on the heavy/extreme end of the spectrum. Phases 7 and 8 feature mostly weak, localized anomalies.

Figure 5.14 shows the area-averaged precipitation (dark) and runoff (light) by MJO phase for three of the water resource basins depicted in Fig. 5.13: the Ohio River, Lower Mississippi River, and Upper Mississippi River basins. Only precipitation and runoff values significant at the 95% level (using a t-test) contributed to the area averages shown in Fig. 5.13. All three basins have very small average precipitation and runoff anomalies in Phases 1-3. The Ohio River basin sees highest runoff in Phases 4, 6, and 7, with only Phase 6 showing a noticeable positive precipitation anomaly. The Lower Mississippi River basin area-averaged runoff is

highest in Phases 4-7, with a large positive precipitation anomaly in Phase 5. The Upper Mississippi River basin has smaller values of averaged runoff than the other two basins, but does see the highest values during Phases 5-7, with maximum precipitation anomaly in Phase 5.

5.4 Summary

The most prominent MJO-related anomalies in U.S. precipitation occur over the central and southern U.S. during MJO Phases 5 and 6, when enhanced tropical convection is located in the Western Pacific. The seasonal mean in the regions which show the strongest precipitation anomalies is scale-dominated. During these two phases, the North American jet stream is weaker and centered further north than the winter mean. The Pacific jet, which is confined to the eastern Pacific during earlier MJO phases, begins to extend eastward across the Pacific. The storm track, as detected in the 200 hPa meridional wind anomalies, is enhanced during Phases 5 and 6 over North America. Positive MFC anomalies are located over the U.S. in the area of the increased precipitation, and the temperature field over the eastern half of the U.S. has a small warm anomaly. Phases 5 and 6 also feature positive anomalies in the NARR-derived runoff in the area of the precipitation anomalies, particularly in the Lower Mississippi and Ohio River Basins.

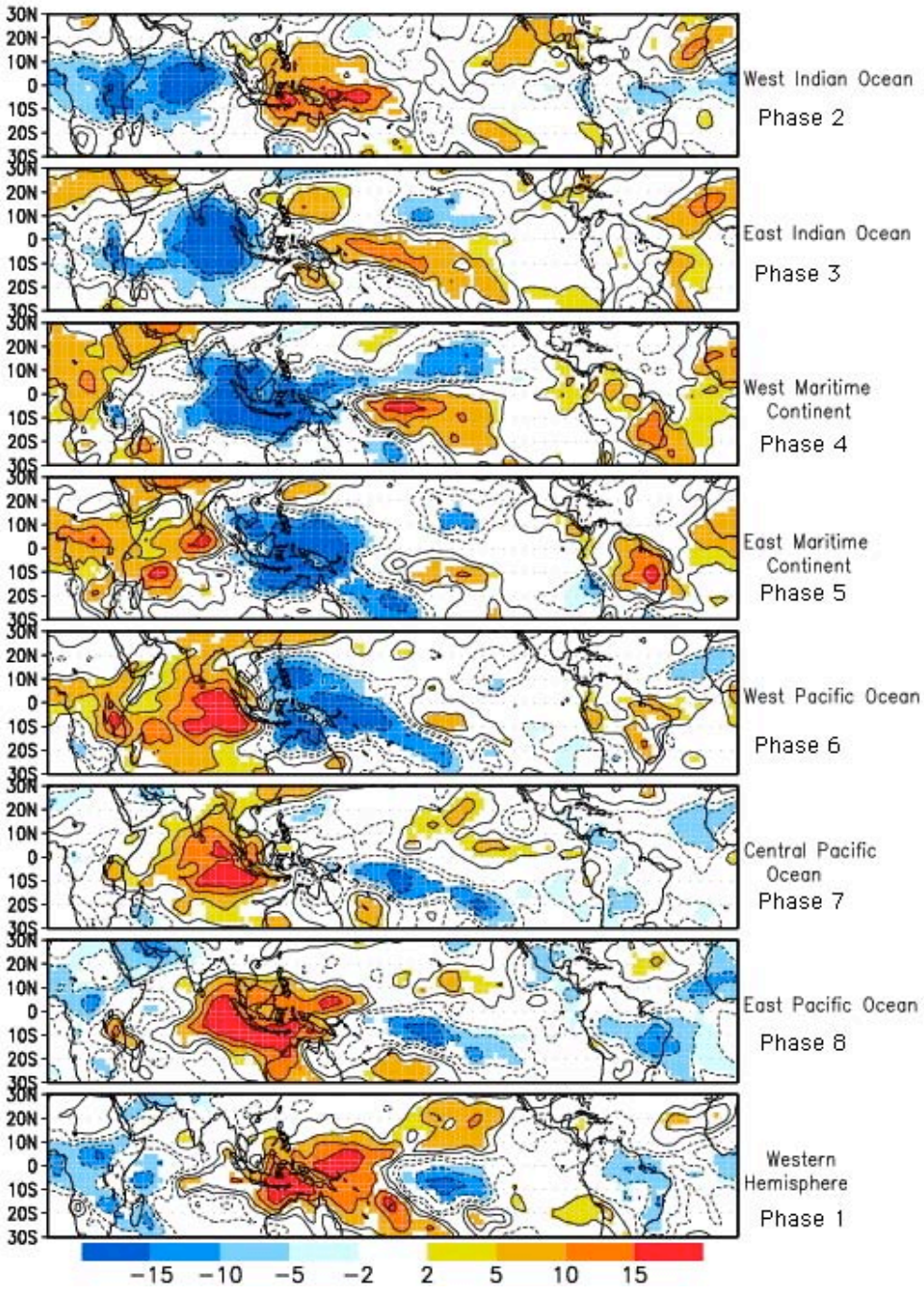

Figure 5.1: Composites of OLR anomalies for eight phases of the MJO, November-March. Figure from the Climate Prediction Center.

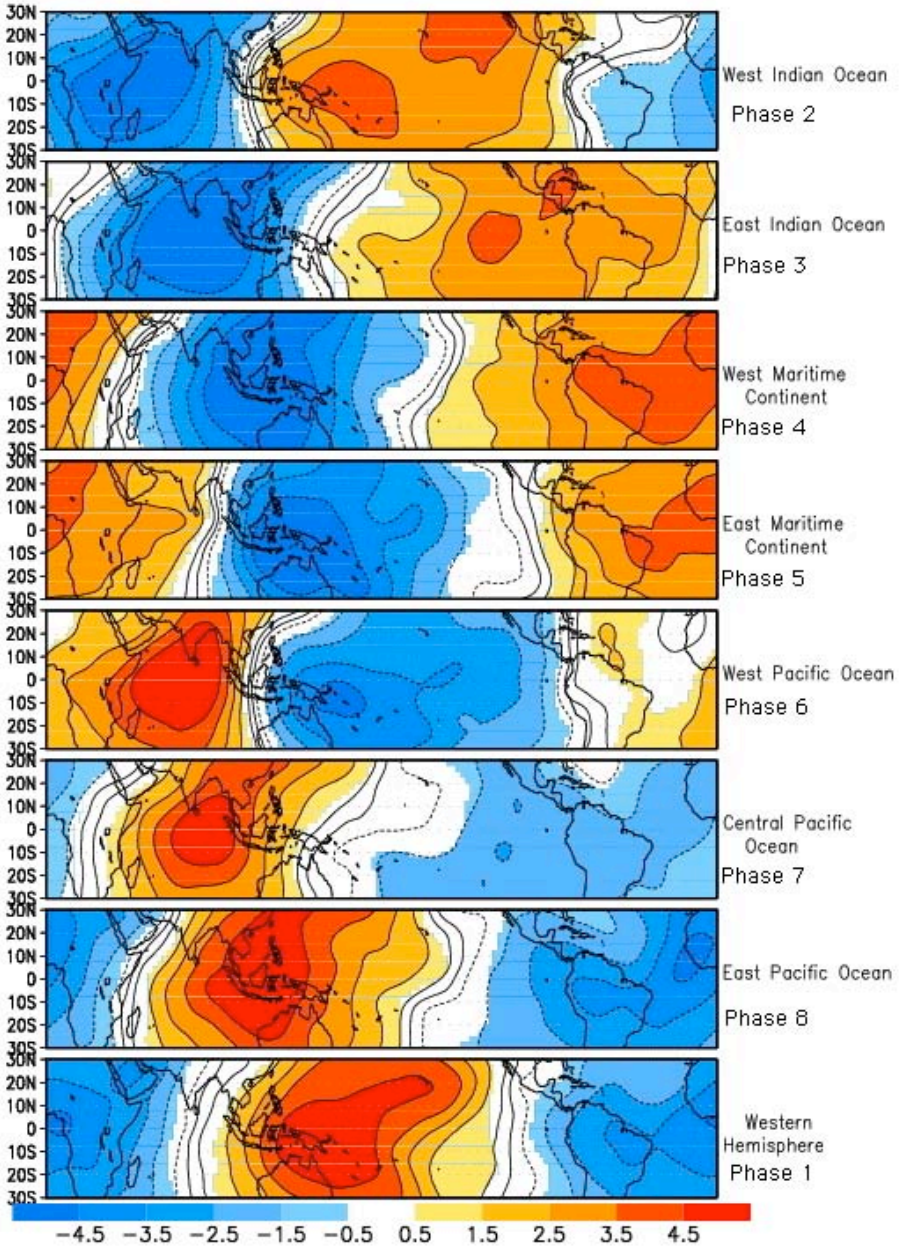

Figure 5.2: As in Fig. 1, for 200 hPa velocity potential. Figure from the Climate Prediction Center.

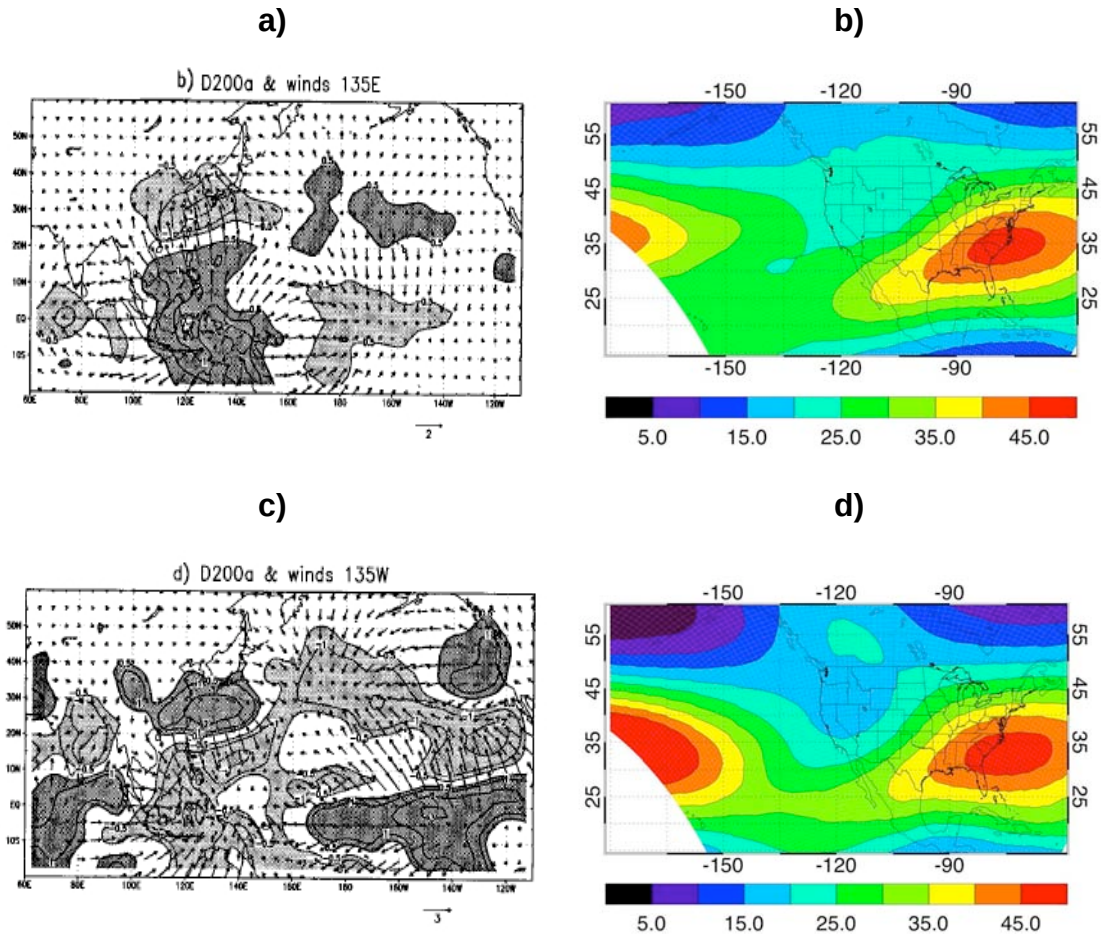

Figure 5.3. (a) Divergence (contours) and divergent wind (arrows) anomalies when enhanced convection is centered over 135°E. Values greater than 0.5E-6 s^{-1} are dark shaded, and values less than -0.5E-6 s^{-1} are light shaded. From Mo and Higgins (1998b), their figure 12b. (b) Winter 200 hPa zonal wind when IO-related enhanced convection is centered over approximately 135°E. (c) same as (a) but for enhanced convection centered at 135°W. From Mo and Higgins (1998b), their Fig. 12d. (d) Same as (b), for convection centered at 135°W.

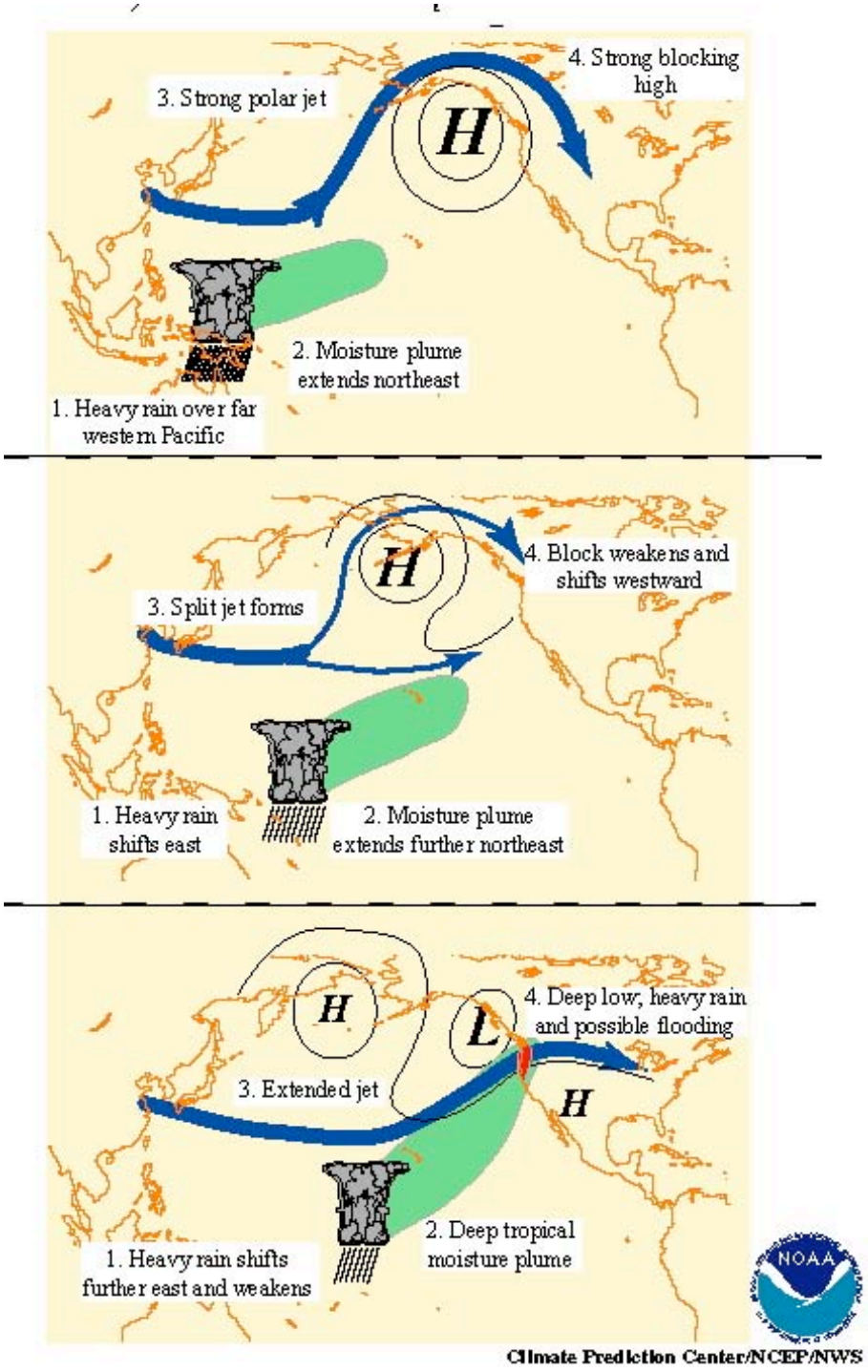

Figure 5.3 (e): schematic representation of MJO interaction with Northern Hemisphere jet streams and storm tracks. Figure from the Climate Prediction Center.

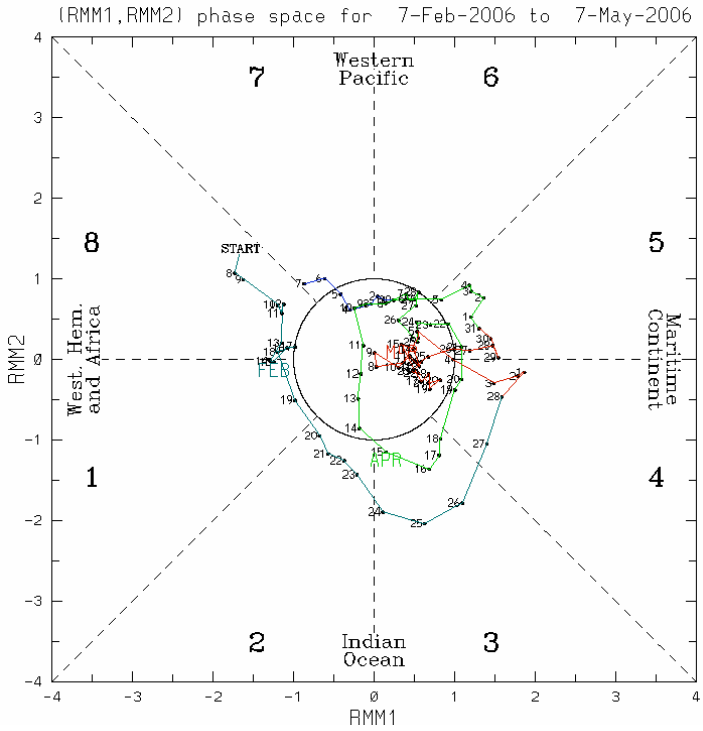

Figure 5.4: An example of a Madden-Julian Oscillation phase diagram. The distance from the center of the diagram indicate the strength of the enhanced convection, and the sector (1-8) indicates the approximate location (Figure from the Climate Prediction Center).

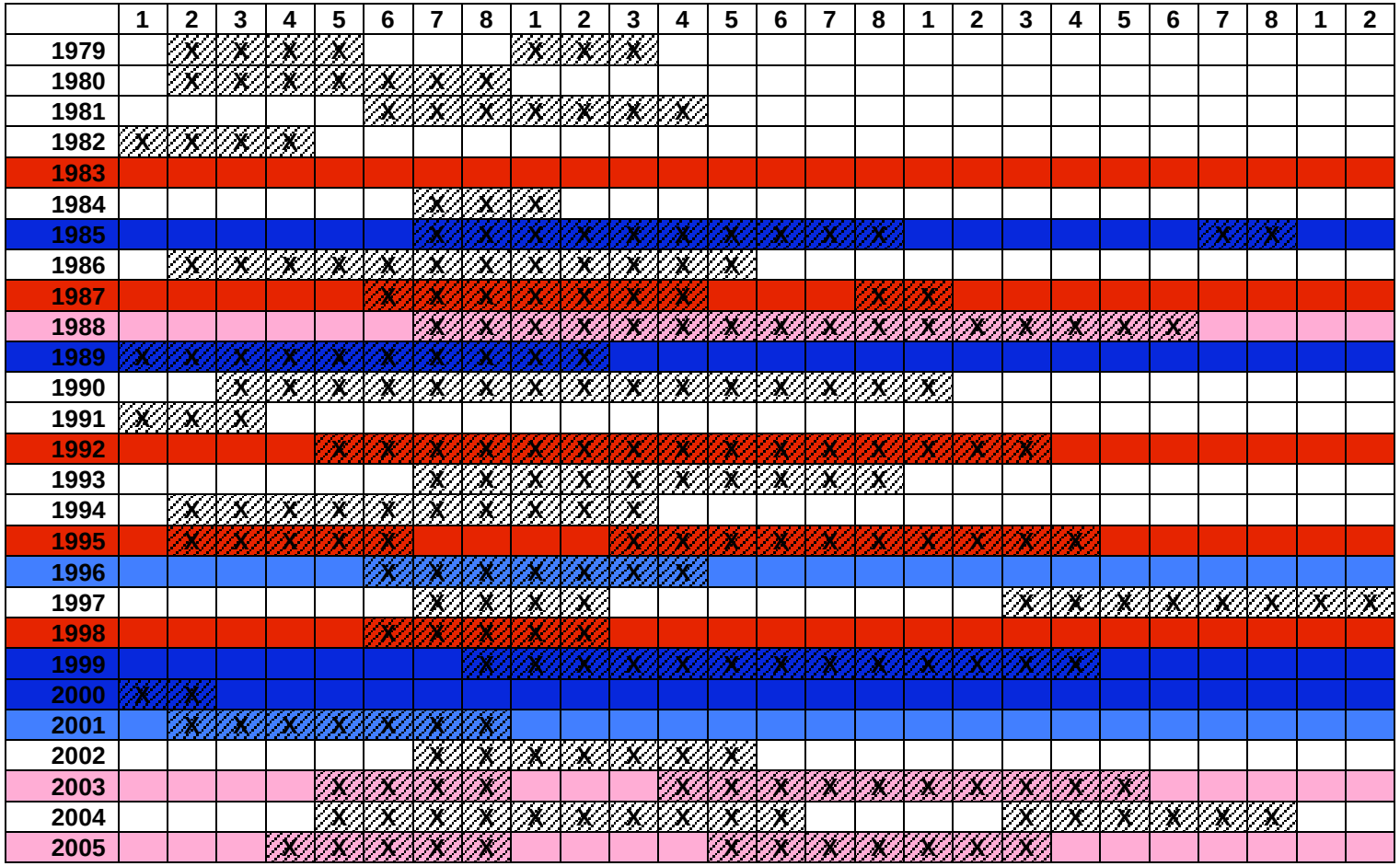

Figure 5.5: Chart indicating MJO phases that occurred during each of the 27 winters (JFM) in the NARR record, and the corresponding ENSO phase for that winter. Red (pink) indicates strong (weak) El Niño, blue (light blue) indicates strong (weak) La Niña, and white is for neutral. ENSO defined according to the CPC ENSO index (see Chapter 4).

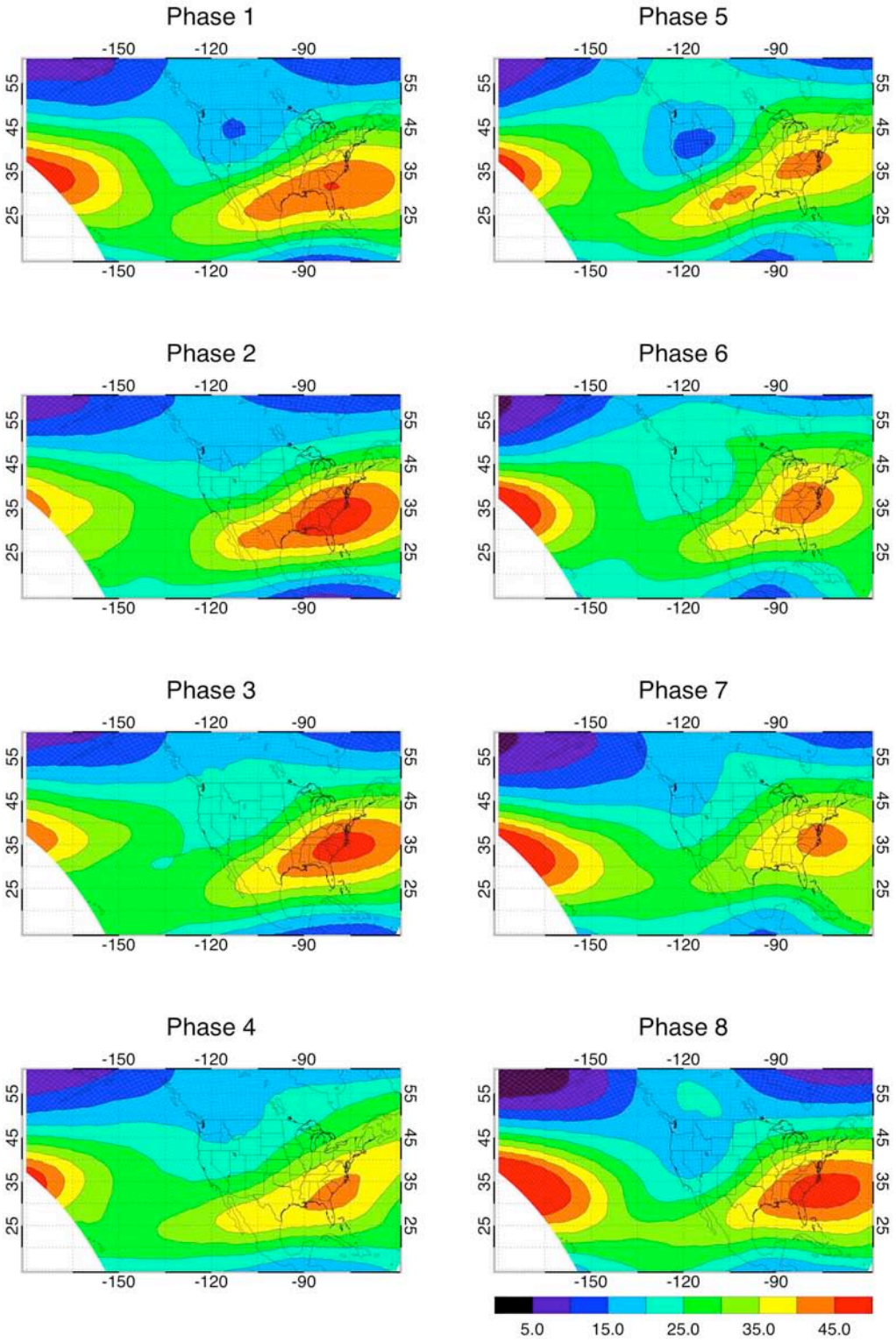

Figure 5.6a: Composite mean winter 200 hPa zonal wind for each of the eight MJO phases.

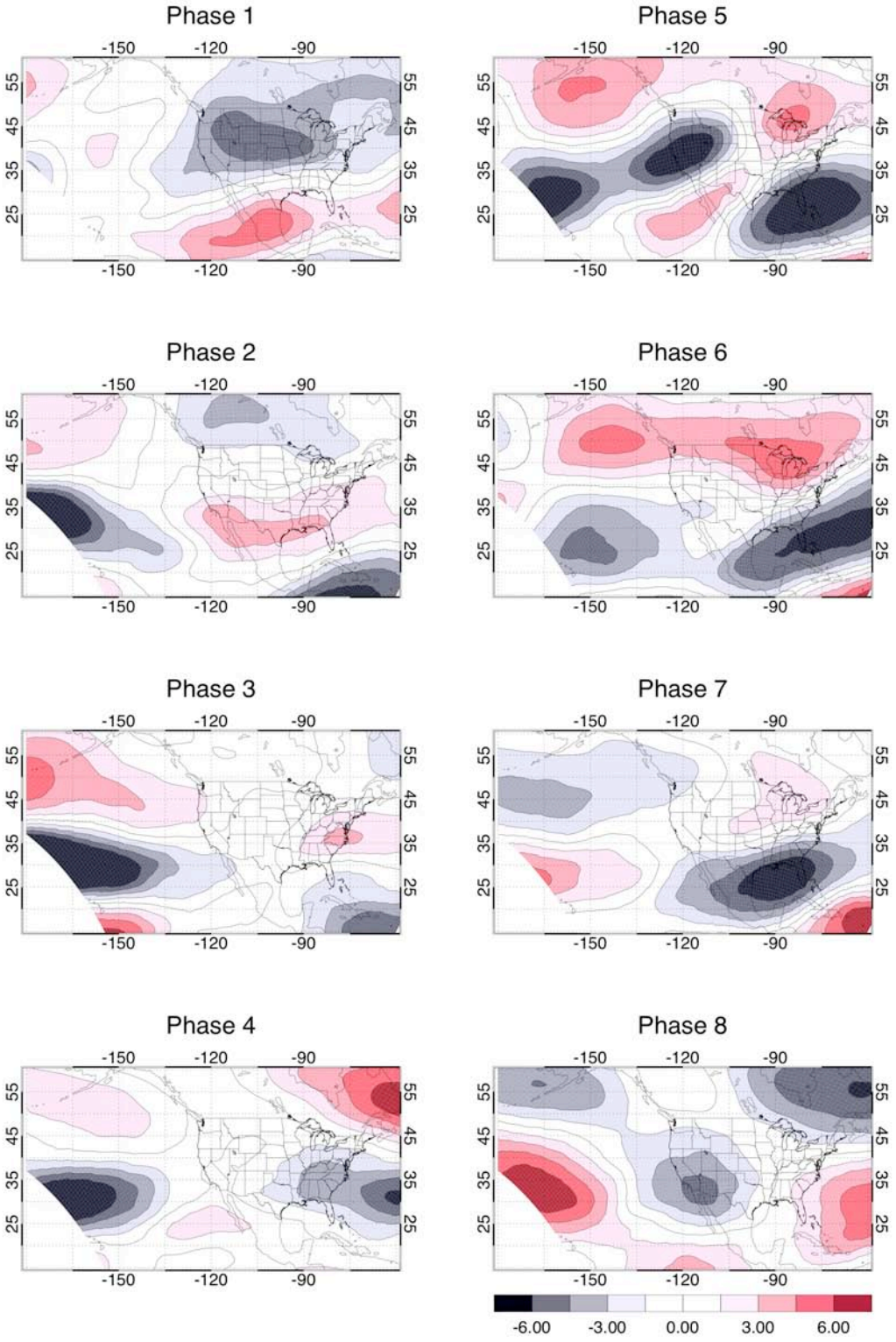

Figure 5.6b: Composite winter 200 hPa zonal wind anomaly, by MJO phase.

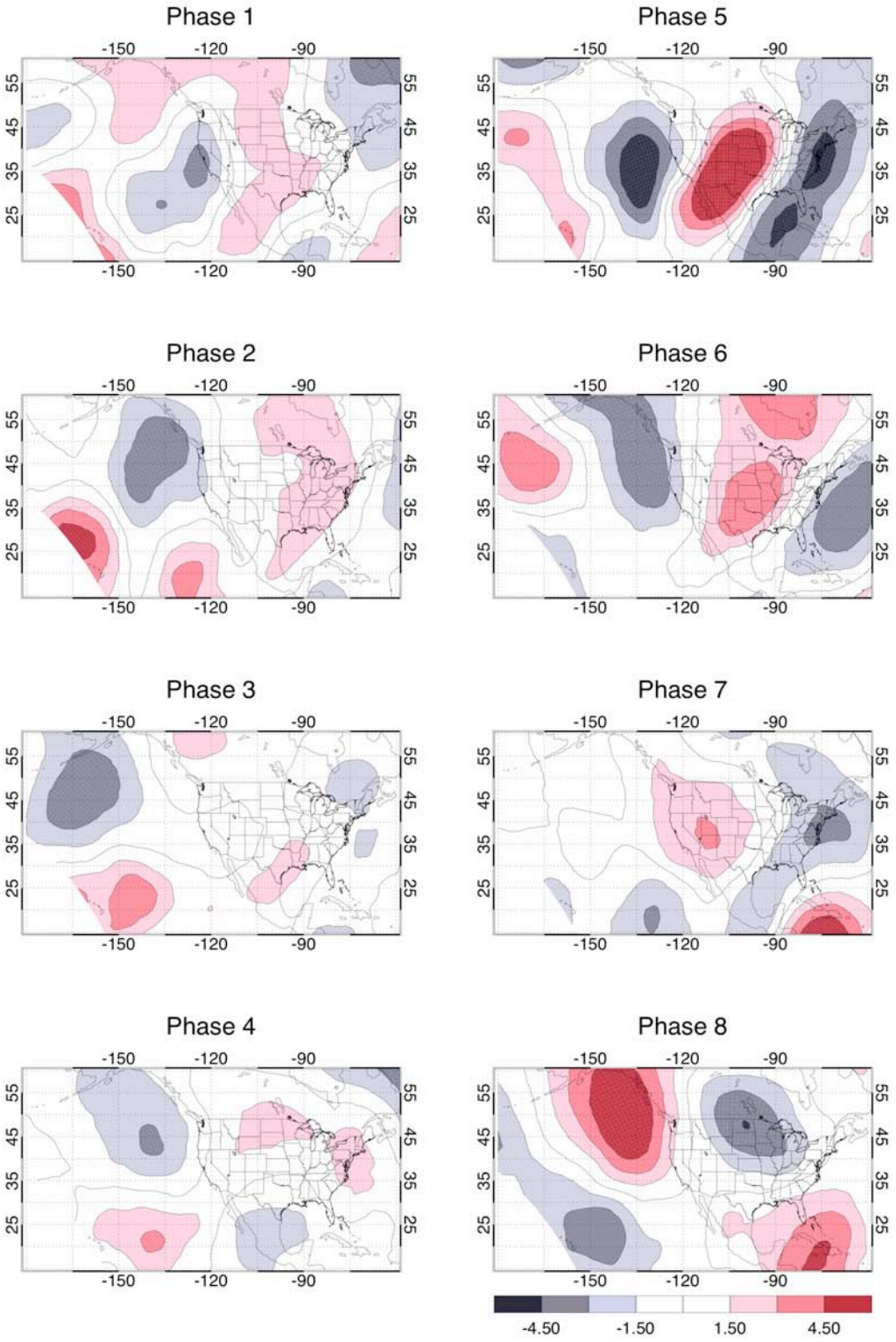

Figure 5.7: Composite winter 200 hPa meridional wind anomaly, by MJO phase.

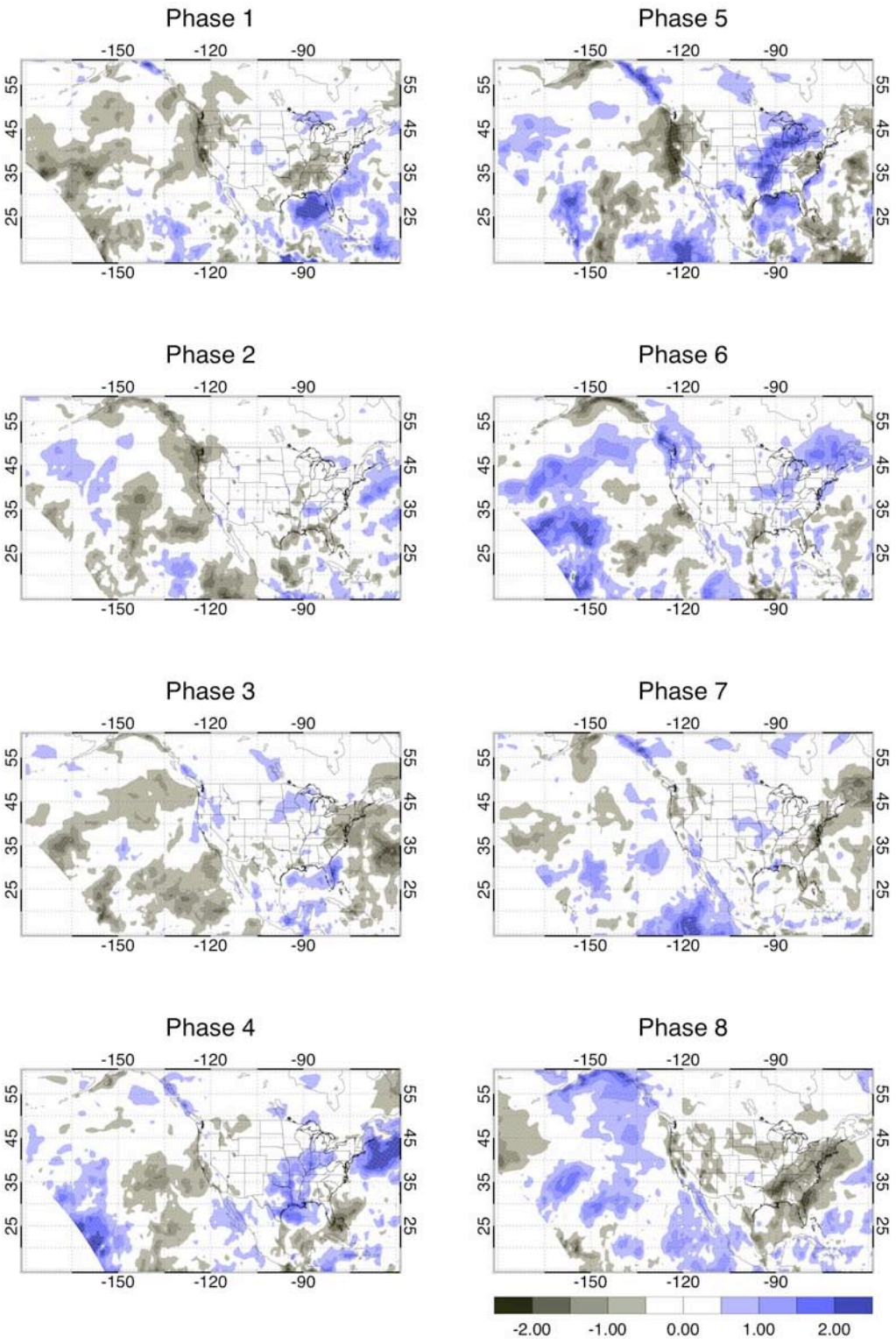

Figure 5.8: Composite winter vertically-integrated moisture flux convergence anomaly, by MJO phase.

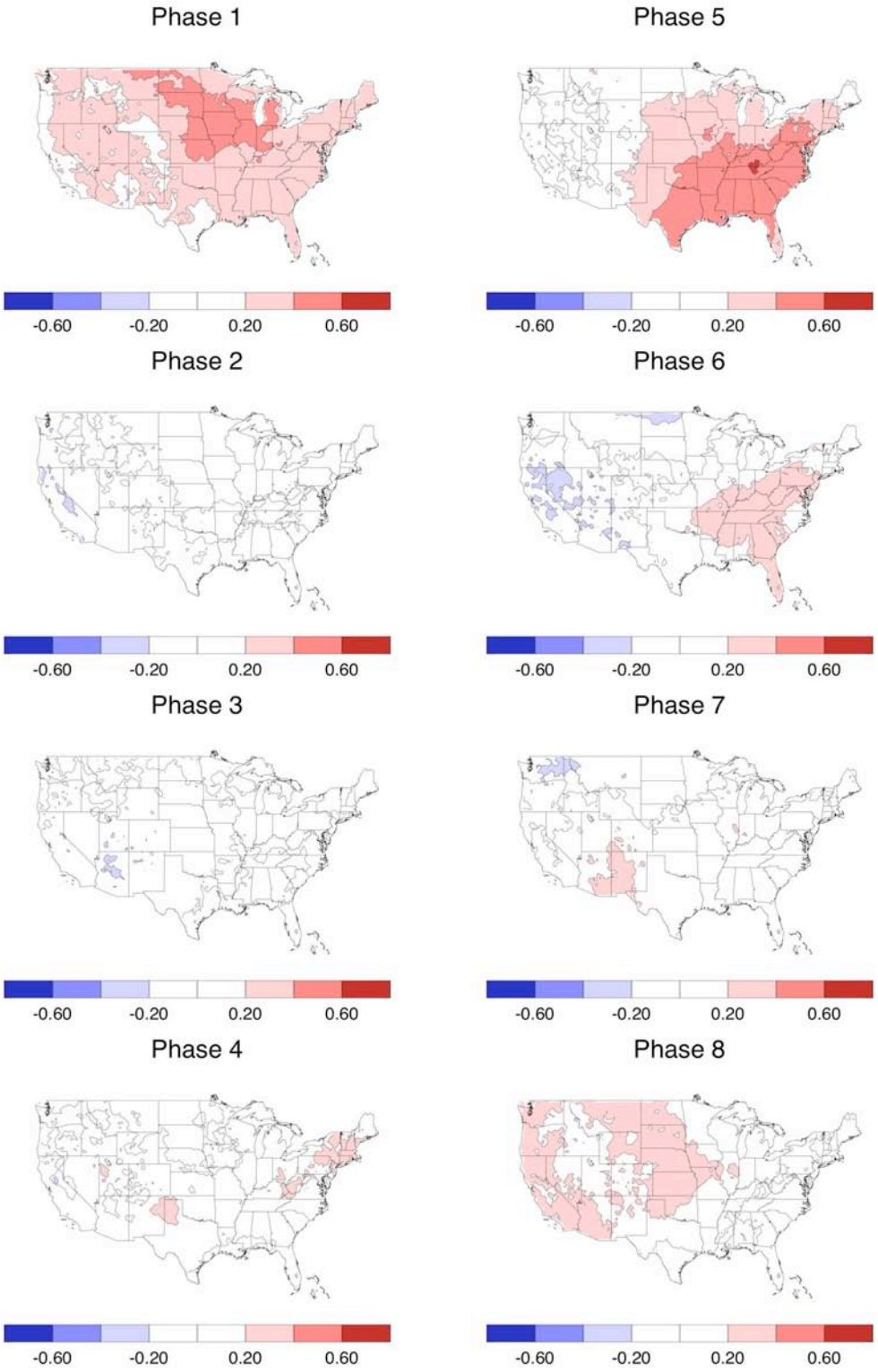

Figure 5.9: Composite winter temperature standardized anomaly, by MJO phase.

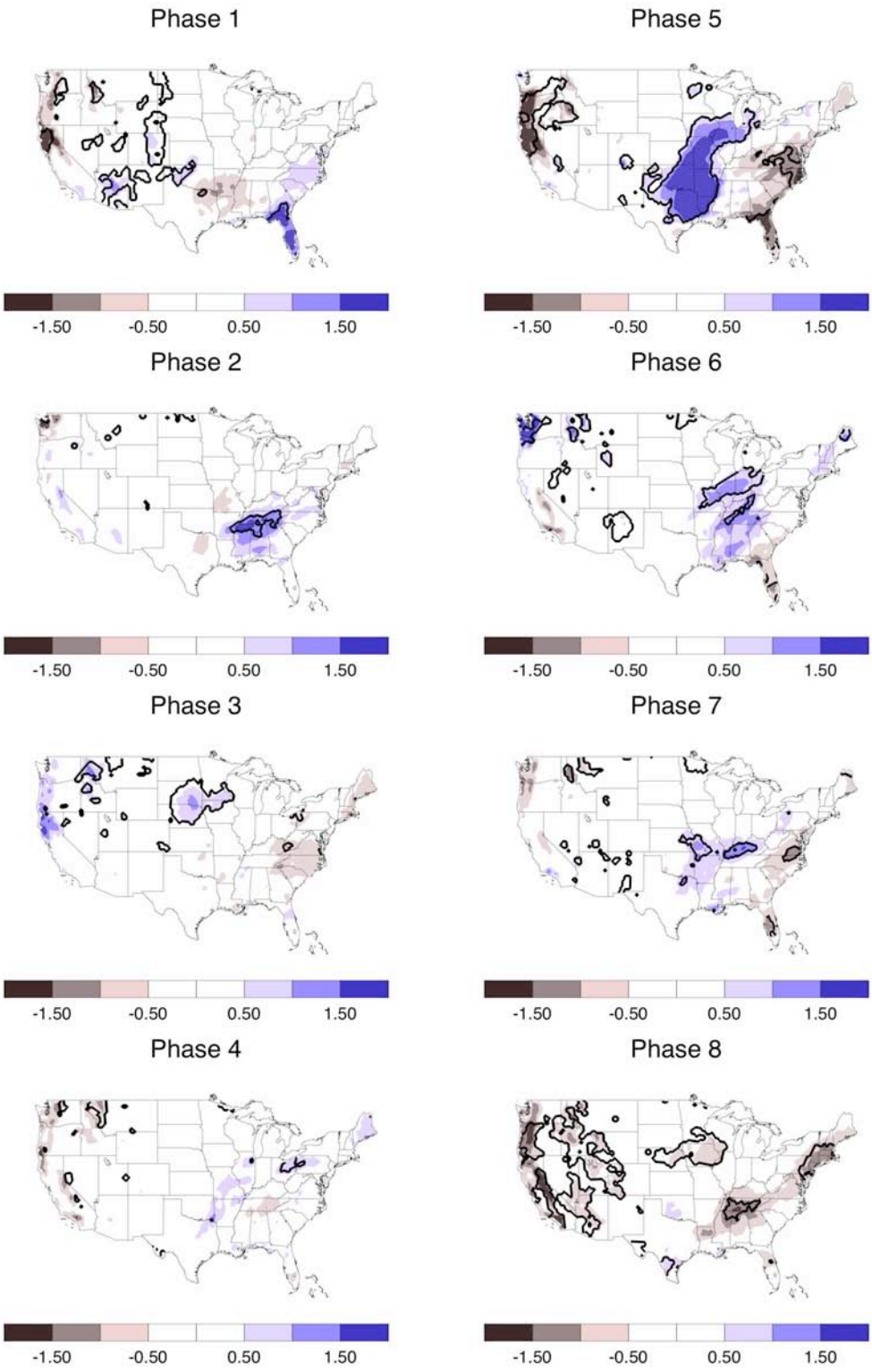

Figure 5.10: Composite precipitation anomaly by MJO Phase. The black contour indicates anomalies significant at the 95% level.

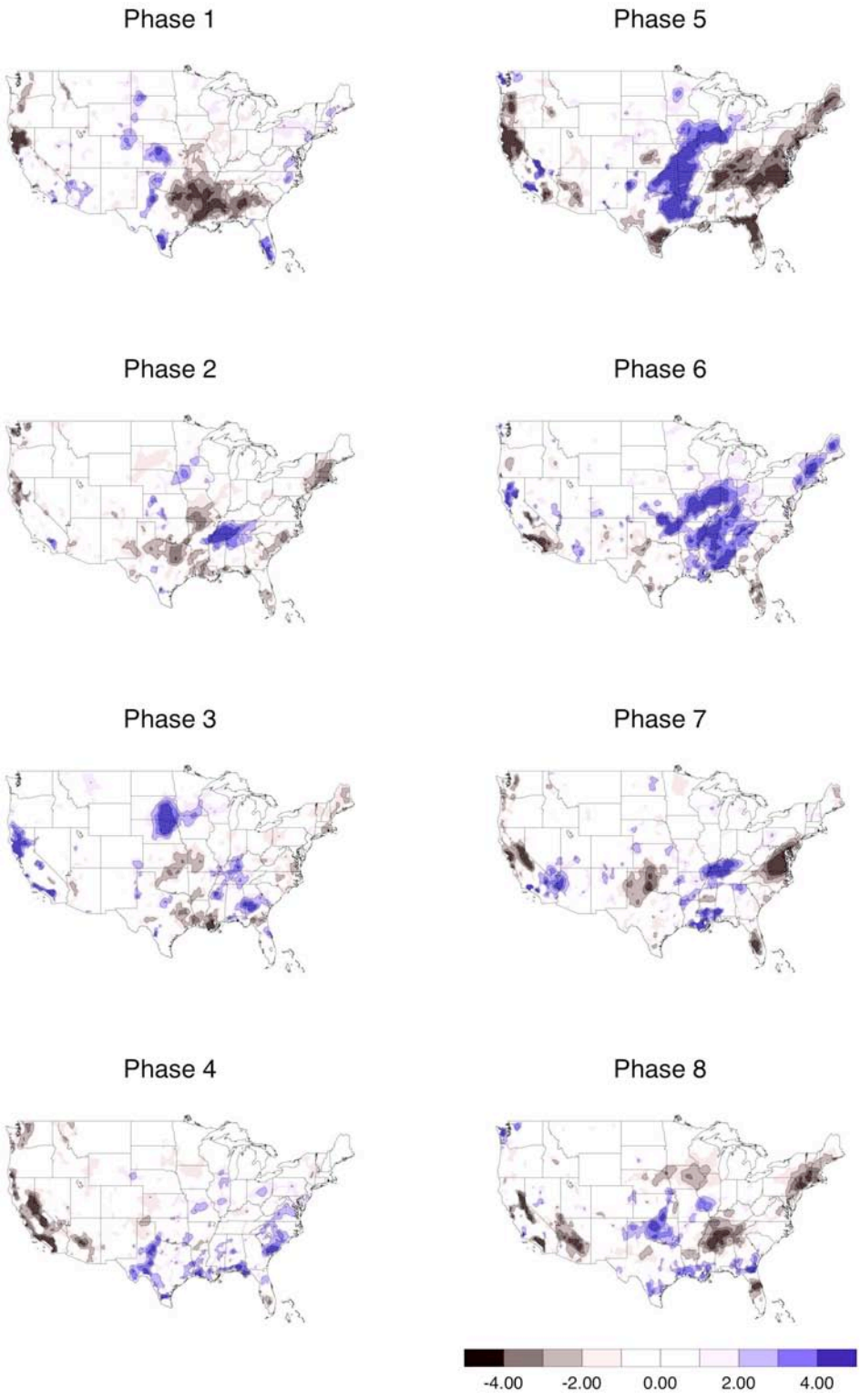

Figure 5.11: Winter gamma-distribution scale parameter anomaly, by MJO phase.

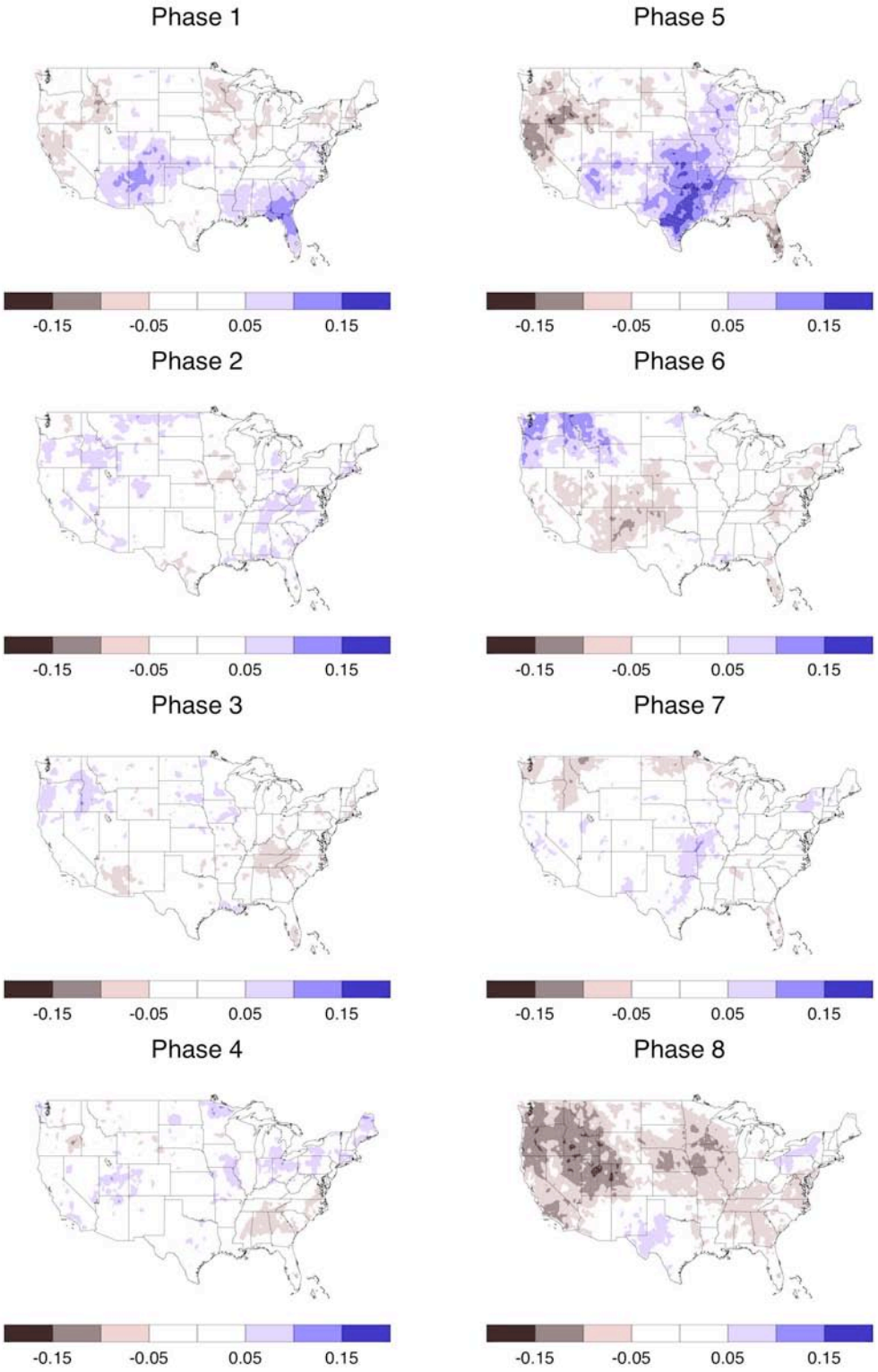

Figure 5.12: Winter wet-day frequency anomaly, by MJO phase.

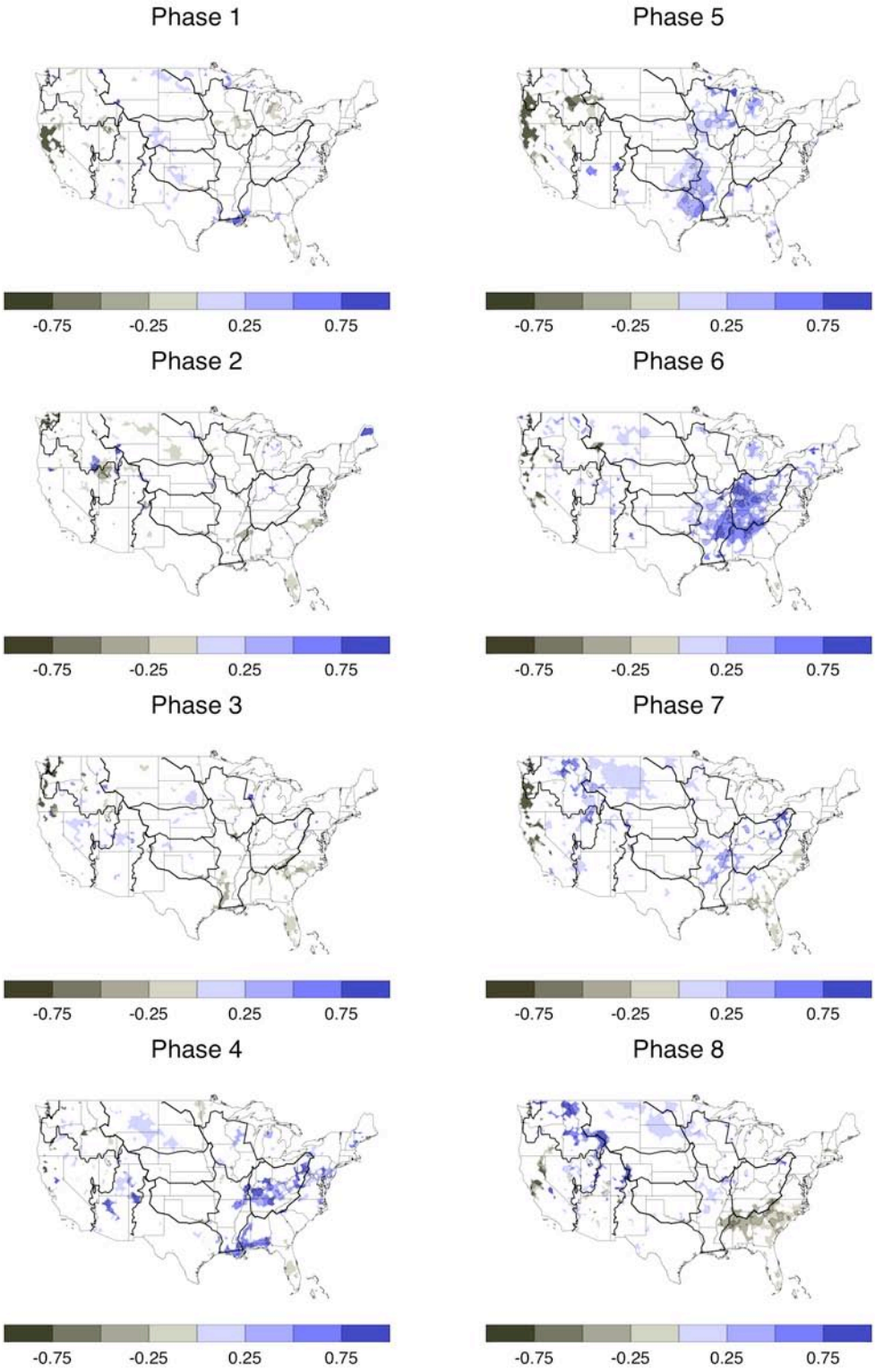

Figure 5.13: Composite winter surface runoff anomaly, by MJO phase. Anomalies are significant at the 95% level. USGS Water Resource Basin contours are overlain.

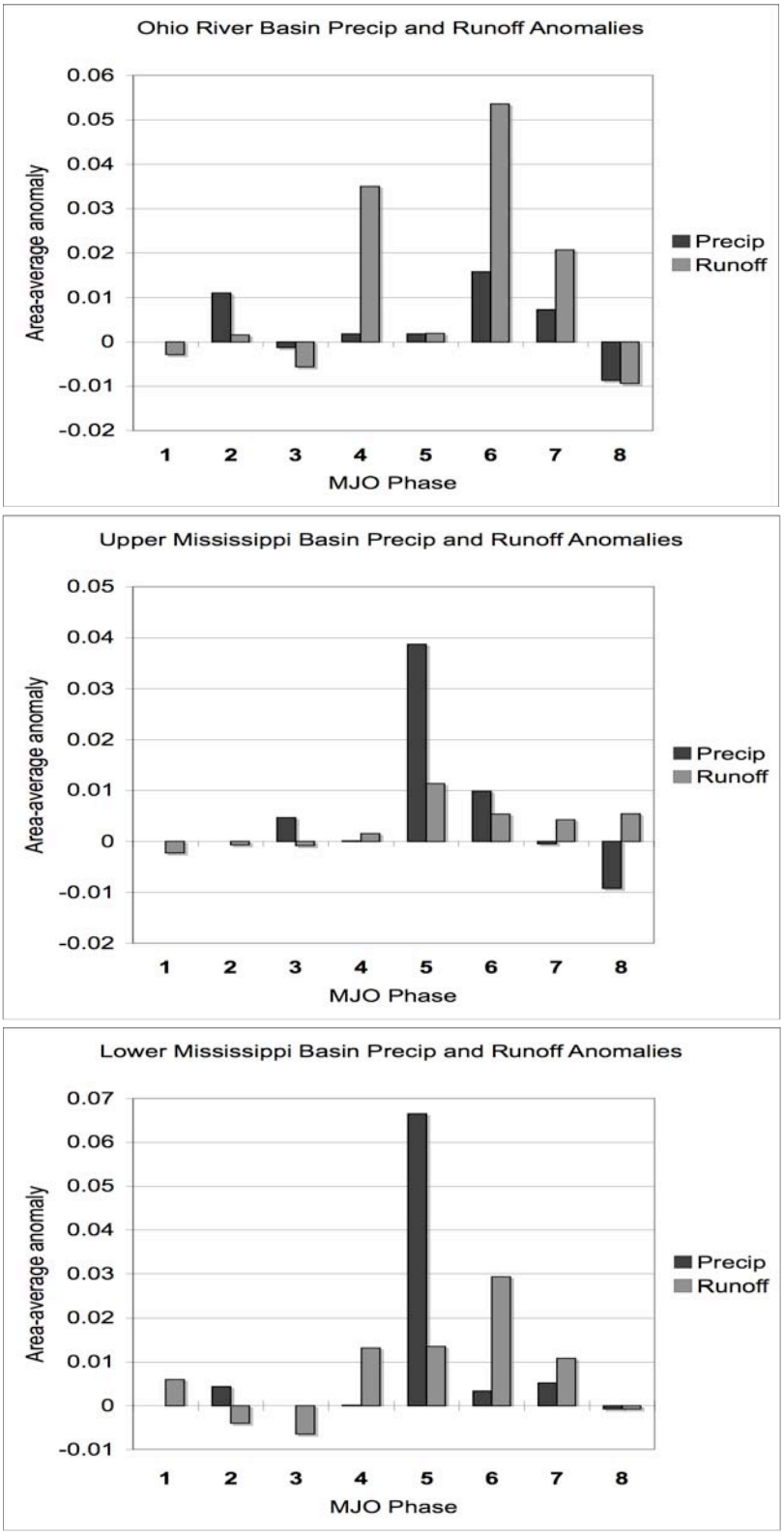

Figure 5.14: Precipitation (dark gray) and runoff (light gray) anomalies by MJO phase, for three USGS hydrologic basins: Ohio River (top), Lower Mississippi (center), and Upper Mississippi.

Chapter 6: Summary, Conclusions, and Future Work Plan

6.1 Summary

Advances in climate prediction on seasonal time scales are highly dependent on improved understanding of the expected variability within the season. With this motivation, this work examined the frequency distribution of daily precipitation and precipitation-related variables over the United States, and its modulation by lower-frequency climate modes, including the El Niño/Southern Oscillation (ENSO) and the Madden-Julian Oscillation (MJO). The primary objective is an improved understanding of the variability of daily precipitation, and the following questions are considered: What regions are sensitive to changes in extreme precipitation? What are the relationships between precipitation and related hydrologic fields such as precipitable water and moisture flux convergence? How do major climate modes affect the climate, mean precipitation, and the precipitation frequency distribution? How do other components of the hydrologic cycle, and their relationship with precipitation, change with climate modes?

The daily precipitation frequency distribution, which is bounded on the left by zero, is assumed to fit a gamma distribution. By examining the shape and scale parameters of the gamma distribution, we can diagnose regions where the seasonal mean is dominated by the contribution of more-variable precipitation with more extreme events (scale-dominated: large scale, small shape) and where the major contribution to the mean is from more-consistent, light/moderate events (shape-

dominated: large shape, small scale). These regions are likely to respond differently to changes in climate, and to require different water resource management or other infrastructure concerns.

This study uses several fields from the North American Regional Reanalysis (NARR), including precipitation and the precipitation-related fields of precipitable water, moisture flux convergence (MFC), and CAPE. Examination of the precipitation-related factors can reveal more about the processes behind precipitation variability, and has potential to contribute to improved model prediction of daily precipitation extremes. The period of record for this study is 1979-2005. To test for decadal variations within the NARR record and to further understand the frequency distribution of precipitation, the first half of the NARR record (1979-1992) and the second half (1993-2005) were compared.

The frequency distribution of precipitation is known to be sensitive to changes in climate, especially along the extremes. Examination of its modulation by ENSO and the MJO reveals the response of shape- and scale-dominated regions to specific climate conditions. ENSO provides insight into interannual variation, while the MJO influences the climate on intraseasonal timescales.

The spatial structure and seasonal evolution of the frequency distribution of precipitation and related fields were examined. In winter, mean precipitation patterns are very similar to the scale parameter patterns; i.e., where the mean wet-day precipitation is high, there are more extreme events, and these regions are scale-

dominated. This is particularly the case along the West coast and the Gulf of Mexico coast. During spring, mean wet-day precipitation over the West coast decreases as the winter storm track weakens, and increases in the central U.S., likely due to the onset of the Great Plains Low-Level Jet (GPLLJ). In summer, the daily mean in both the wettest and the driest areas of the country (the southeast and the west, respectively) is dominated by more frequent light and moderate rainfall days, i.e., shape-dominated. On the other hand, the central U.S., where moisture is brought in from the Gulf of Mexico by the GPLLJ, is scale-dominated. The North American Monsoon does not appear as a strong feature in the average wet-day amount in summer, but it is evident in the higher frequency of rainfall in Arizona, New Mexico, and Colorado. The Monsoon contributes consistent light and moderate rains to this area (Douglas et al. 1993) and this is illustrated by the strong dominance of the shape parameter. Fall precipitation patterns over much of the U.S. appear largely similar to winter. The similarities between fall and winter suggest that, regarding the daily precipitation frequency distribution, the transition between the warm season and the cold season occurs faster than the transition between the cold season and the warm season (i.e., spring).

Over all four seasons, regions where precipitation is scale-dominated (more variable and extreme precipitation events), do not have a correspondingly high precipitable water scale parameter. This implies that extreme precipitation does not have a strong link with high daily precipitable water. On the other hand, mean MFC and the MFC scale parameter closely resemble the mean and scale of precipitation,

with stronger mean MFC corresponding to higher precipitation, and regions with more variable and extreme daily precipitation having more frequent strong daily MFC. This suggests a strong relationship between the variability of MFC and that of precipitation. In summer, the Monsoon is evident in both the precipitable water and MFC fields in southern Arizona and New Mexico.

The examination of decadal changes in the NARR record revealed a general pattern of lower (higher) wet-day mean precipitation in the western (eastern) portion of the country during the second half of the record. This was the case for all four seasons. For winter, this investigation found more-frequent, lighter-to-moderate daily precipitation over the Rockies during the second half of the record, as well as a more-skewed distribution with a greater contribution of extremes in the Midwest and Atlantic coast regions. In spring, several regions have a changed wet-day frequency between the two halves of the record, but the gamma distribution parameters are largely unaltered, implying that the proportion of light, moderate, and extreme events is generally unchanged. Summer precipitation west (east) of the Rocky Mountains shows decreased (increased) wet-day mean precipitation and extremes. Autumn decadal changes in the NARR record are similar to those seen in winter. The mean precipitable water does not change substantially between the two halves of the record, nor does the precipitable water frequency distribution. The mean MFC also does not exhibit large changes. However, the frequency and intensity of strong MFC does, and where it increases (decreases) extreme precipitation increases (decreases).

In El Niño winters, the southwest U.S. has a mean wet-day precipitation about 80% greater than during La Niña. The Lower Missouri River basin and the Gulf of Mexico coast receive 40-60% greater mean precipitation, while Ohio River basin precipitation is reduced during El Niño. The extended Pacific jet stream characteristic of an El Niño winter is the likely cause of the higher wet-day frequency over much of the south and southwest. The spatial pattern of the changes of the scale parameter is very similar to that of the changes in the mean, but substantially greater in magnitude, meaning the response of the extremes is stronger than that of the mean. Most of the regions showing prominent changes between the ENSO phases have a mean winter frequency distribution that is scale-dominated, except for the Lower Missouri River basin. This area, which is shape-dominated in the seasonal mean, becomes more scale-dominated during El Niño. The mean precipitable water exhibits very little change between El Niño and La Niña. However, the pattern of change in mean wet-day MFC between the two phases resembles that of mean precipitation, and, similar to precipitation, the most substantial contribution to the change in mean MFC is from the extremes.

For the most part, MJO Phases 1-4, when MJO-related enhanced convection is located over Africa or the Indian Ocean, do not feature large signals in the mean precipitation. The Pacific jet stream is confined to the western Pacific during these phases, and the midlatitude storm track does not show enhancement over the North American continent. The most prominent MJO-related anomalies in U.S. precipitation occur over the central and southern U.S. during MJO Phases 5 and 6,

when enhanced tropical convection is located in the Western Pacific. During these two phases, the North American jet stream is weaker and centered further north than the winter mean, the Pacific jet begins to extend eastward across the Pacific, and the midlatitude winter storm track is enhanced over North America. Positive MFC anomalies are located over the U.S. in the area of the increased precipitation, and the temperature field over the eastern half of the U.S. has a small warm anomaly. The NARR-derived runoff in the Lower Mississippi and Ohio River Basins also has positive anomalies during Phases 5 and 6. A small positive precipitation anomaly in the Midwest and south persists into Phase 7, but otherwise precipitation anomalies over the U.S. during Phases 7 and 8, when the MJO signal crosses over the date line and into the western hemisphere, are mostly negative. The Pacific jet reaches its furthest eastward extension during these two phases.

6.2 Conclusions

Several conclusions can be drawn from this study of the frequency distribution of daily precipitation.

The moisture flux convergence frequency distribution is a potential alternative to assess precipitation. This study found close resemblances between the gamma distribution parameters of both precipitation and MFC, and similar responses to ENSO and the MJO. Regions of the U.S. that are subject to more extreme precipitation events also have more strong daily MFC. While the frequency distribution of daily precipitation can be determined from observations or reanalyses

that assimilate precipitation, its reliability in a model's seasonal forecasts is in doubt due to the model's biases, which are the product of uncertain parameterizations. Given that MFC has a lesser dependence than precipitation on parameterizations, it is speculated that its frequency distribution is a good alternative to assess frequency distributions in the more biased-affected seasonal forecasts.

The variability of daily precipitation is not strongly linked to the variability of daily precipitable water. Large values of precipitable water do not seem to have a very strong link to heavy and extreme precipitation (unlike MFC), nor does the modulation of precipitable water by ENSO or the MJO closely resemble that of precipitation. Hence, precipitable water is unlikely to be a good alternative for assessing precipitation.

Scale-dominated areas in winter are susceptible to changes in climate. ENSO-related changes in winter total precipitation are largely due to changes in the heavy and extreme events; regions where the seasonal mean depends on these events (i.e., scale-dominated regions) were affected. Most of the regions of the U.S. that exhibited substantial modulation of the precipitation frequency distribution by ENSO or the MJO were scale-dominated (mean precipitation is dependent on extreme events), including the West coast and the southeast. The exception to this is the Lower Missouri River basin, a normally shape-dominated region that experienced large increases in mean precipitation and the scale parameter, and a substantial decrease in the shape parameter: this region became significantly more scale-dominated during El Niño.

The MJO modulates the frequency distribution of daily precipitation on intraseasonal timescales. When MJO-related enhanced tropical convection is located in the western Pacific, mean precipitation in the central U.S. experiences is anomalously high. An increase in the scale parameter accounts for this, indicating increased heavy and extreme precipitation events. Barlow and Salstein (2006) suggest that their findings regarding rainfall in Central America and Mexico relative to the MJO, in combination with the relatively high medium-term predictability of the MJO (Waliser et al. 2003), could lead to sub-seasonal rainfall prediction.

The response of the frequency distribution of daily precipitation to climate variability is relevant for studies of climate change and long-term trends. Some previous modeling studies have suggested that climate change due to increased atmospheric CO_2 may take the form of an El Niño-like response (Meehl and Washington 1996; Meehl et al. 2006). If this is the case, the proportion of heavy/extreme rainfall days to light/moderate days should be expected to change (Katz and Brown 1992, Wilby and Wigley 2002, Watterson and Dix 2003). Also, in the United States a century-long precipitation increase has been identified, with a nationwide increase in mean total precipitation of 7-15% per 100 years, and a significantly greater increase in heavy and very heavy precipitation (Groisman et al. 2001, 2005; Higgins et al. 2007). In examining the response of the frequency distribution to ENSO, this study can contribute to our understanding of the response to future climate change. The methods and results of this work, and particularly the

strong relationship between precipitation and moisture flux convergence, should have value for the Intergovernmental Panel on Climate Change (IPCC) scenarios.

6.3 Future work

The work accomplished in this project presents the opportunity to pursue several lines of study. These include:

- Investigation of the response of the gamma distribution of precipitation in the upcoming NCEP Climate Forecast System (CFS) reanalysis.
- Development of model bias corrections for precipitation outlooks. The relationship between the frequency distributions of precipitation and MFC and between strong MFC and extreme precipitation raise the possibility of using MFC as a proxy for precipitation.
- Examination of the modulation of the frequency distribution by other major climate modes, including the Pacific-North American teleconnection pattern (PNA), the North Pacific Oscillation (NPO), the North Atlantic Oscillation (NAO), and others. A related examination focus, which would require a longer timeseries than that of NARR, is the behavior of the precipitation frequency distribution during developing or decaying El Niño events.
- Investigation of the susceptibility of shape- or scale-dominated regions to drought, dry spells, and multi-day rain events. The results of the MJO focus of study, which find contemporaneous anomalies in the NARR-generated runoff and the precipitation scale parameter, suggest a link between the scale

parameter and runoff that would bear further examination. Also, a study of soil moisture data, such as that of Fan and van den Dool (2004) and related anomalies in the precipitation frequency distribution would discover the relationship between drought and shape- and scale-dominated regimes.

The concepts developed in this work are relevant for both near-term and long-term climate modeling, climate change studies, and a more extensive investigation into the response of the hydrologic cycle to changes in climate.

The diurnal cycle of precipitation over the North American monsoon region during the NAME 2004 field campaign

Emily J. Becker and Ernesto Hugo Berbery*

Department of Atmospheric and Oceanic Science/ESSIC,
University of Maryland,
College Park, Maryland

Journal of Climate **21**, 771-787

*Corresponding author address: Ernesto Hugo Berbery,
Department of Atmospheric and Oceanic Science/ESSIC,
3427 Computer and Space Sciences Building,
University of Maryland,
College Park, MD 20742-2425.
Email: berbery@atmos.umd.edu

Abstract

The structure of the diurnal cycle of warm-season precipitation and its associated fields during the North American Monsoon are examined for the core Monsoon region and for the southwestern United States, using a diverse set of observations, analyses and forecasts from the North American Monsoon Experiment field campaign of 2004. Included are rain-gauge and satellite estimates of precipitation, Eta model forecasts, and the North American Regional Reanalysis (NARR). Daily rain rates are of about the same magnitude in all datasets with exception of the Climate Prediction Center (CPC) Morphing technique (CMORPH), which exhibits markedly higher precipitation values.

The diurnal cycle of precipitation within the core region occurs earlier in the day at higher topographic elevations, evolving with a westward shift of the maximum. This shift appears in the observations, reanalysis, and, while less pronounced, in the model forecasts. Examination of some of the fields associated with this cycle, including convective available potential energy (CAPE), convective inhibition (CIN), and moisture flux convergence (MFC), reveals the westward shift appears in all of them, but more prominently in the latter.

In general, warm-season precipitation in southern Arizona and parts of New Mexico shows a strong effect due to northward moisture surges from the Gulf of California. A reported positive bias in the NARR northward winds over the Gulf of California limits their use with confidence for studies of the moist surges along the Gulf, thus, the analysis is complemented with operational analysis and the Eta model short-term simulations. The non-surge diurnal cycle of precipitation lags the CAPE maximum by six hours and is simultaneous with a minimum of CIN, while the moisture flux remains divergent throughout the day. During surges, CAPE and CIN have modifications

only to the amplitude of their cycles, but the moisture flux becomes strongly convergent about six hours before the precipitation maximum, suggesting a stronger role in the development of precipitation.

1. Introduction

Rainfall during the North American Monsoon accounts for a majority of the annual total in the Southwestern United States and western Mexico. The precipitation produced during the Monsoon accounts for as much as 80% of annual rainfall in the area of western Mexico along the Gulf of California, and up to 60% in southern Arizona and New Mexico (Douglas et al. 1993). The Monsoon is characterized by a reversal in pressure and wind patterns resulting from the seasonal heating of land in the northern hemisphere summer (Adams and Comrie 1997). Midtropospheric flow shifts from dry and westerly in the late spring to moist and easterly/southeasterly in July (Douglas et al. 1993); a distinct pattern of increased convection and precipitation in northwestern Mexico and the southwestern United States is the primary effect of the system.

The core Monsoon region, lying along western Mexico between approximately 20°N and 30°N, receives the most intense precipitation of the geographical area directly affected by the Monsoon. This region exhibits a prominent diurnal cycle of precipitation due to the combined effects of the sea-breeze with upslope flows produced by diurnal heating and topographic forcing by the Sierra Madre Occidental (SMO) mountain range (Johnson et al. 2005). Low-level moisture evaporated from the Gulf of California is transported by this upslope flow to the core region (Stensrud et al 1995). The resulting moisture flux convergence over the western slopes of the SMO leads to heavy precipitation (Douglas et al. 1993; Stensrud et al. 1995; Berbery 2001). Mesoscale convective systems that form over the mountains of western Mexico and drift to the west throughout their lifespans are also believed to contribute to the heavy precipitation during the monsoon season (Howard and Maddox 1988; Smith and Gall 1989; Farfan and

Zehnder 1994). The general temporal structure of the diurnal cycle of precipitation in the core region of the monsoon is for precipitation to begin in the late afternoon, peak in the late evening to midnight, and reach a minimum in the morning (Gochis et al. 2003).

In the northern sector of the Monsoon, moisture is transported into Arizona and New Mexico via a nocturnal/predawn low-level jet from the Gulf of California (Douglas 1995; Berbery 2001). Douglas (1995) identified the presence of this jet, characterized by southerly winds below about 900 hPa, on about 75% of the summer days in his analysis. The southerly wind velocity is strongest in the late evening to early morning hours (Douglas et al. 1998), when the boundary layer is most stable, and is likely produced by the east-west temperature gradient created by nighttime cooling of the slopes of the SMO (Anderson et al. 2001). This jet transports significant quantities of water into northwest Mexico and southern Arizona (Fawcett et al. 2002).

Another occasional yet important feature of the monsoon is the northward surge of relatively cool, moist air through the Gulf of California, often linking precipitation in the southwestern United States to tropical disturbances in the Pacific Ocean (Hales 1972; Hales 1974). These surges are accompanied by decreases in temperature and increases in humidity and surface pressure in southern Arizona. Surges, as seen in the low-level wind field (Bordoni et al. 2004), usually originate in the southern Gulf of California and travel northward into the southwestern United States, and are usually associated with the passage of an easterly wave (Fuller and Stensrud 2000); tropical cyclones approaching the Gulf can create strong surges (Anderson et al. 2000; Higgins and Shi 2005). Moisture surges along the Gulf have a critical role for the development of precipitation in the southwestern United States. These surges have been found to accompany a majority

of the precipitation in Arizona during July and August (e.g., Berbery and Fox-Rabinovitz 2003; Higgins et al. 2004), but have only a modest effect on precipitation along northwestern Mexico (Douglas and Leal 2003).

The North American Monsoon Experiment (NAME) field campaign of 2004 has provided a valuable opportunity to analyze the variability of the Monsoon system at smaller scales than those allowed by previous datasets. NAME incorporates observational data sets (including satellite estimates and an extensive rain-gauge network) and empirical and modeling studies, and employs a tiered approach. Tier I covers the core monsoon area of northwestern Mexico, as well as southern Arizona and New Mexico, and is the focus area for this study. NAME has a stated goal of determining the sources and limits of predictability of warm season precipitation over North America (Higgins et al. 2006). This can only be achieved if physical mechanisms are properly represented, even at the mesoscale, including the diurnal cycle.

The objective of this study is to investigate the main features of the North American Monsoon diurnal cycle of precipitation, using remotely sensed precipitation estimates, rain-gauge measurements, Eta model forecasts, and regional reanalysis data. This article is structured as follows: Section 2 contains information about the model and data products used for the study, and Section 3 details the results for the main features of the diurnal cycle of precipitation, including the structure of the diurnal cycle, potential associated fields, and the effect of moisture surges, for both the core monsoon region and the southwestern United States. Section 4 presents a summary of the work and conclusions.

2. Empirical, model, and reanalysis products

The diurnal cycle of precipitation and associated fields during the NAME enhanced observing period of July and August, 2004 was analyzed using data from several sources. Precipitation data examined for this study include RMORPH, the "research-quality" version of the Climate Prediction Center morphing method (CMORPH) satellite estimates, and observations from the CPC US-Mexico rain-gauge network. Several fields, including precipitation and associated thermodynamic and dynamic fields, were obtained from the North American Regional Reanalysis (NARR) products, and from model forecasts produced using NCEP's workstation version of the Eta model, run at the University of Maryland.

a. Empirical precipitation data

The primary satellite-estimated precipitation data for this study comes from RMORPH, which produces high-resolution ($0.25° \times 0.25°$) precipitation estimates using passive microwave satellite rainfall estimates propagated by motion vectors from geostationary satellite infrared cloud motion estimates (Joyce et al. 2004). For precipitation estimates over land, RMORPH uses the Climate Prediction Center (CPC) daily rain-gauge analysis (Higgins et al. 2000), disaggregated by CMORPH satellite estimates (Janowiak et al. 2006). Although there may be several reasons for the CMORPH overestimation of precipitation, previous studies have suggested that in semi-arid regions this error can result from the fact that the estimate is drawn from the cloud top characteristics, while large evaporation may occur before the rainfall reaches the

surface, resulting in too much precipitation at the surface (see Rosenfeld and Mintz 1988; McCollum et al. 2002; Janowiak et al. 2004; and Shi et al. 2005).

Rain-gauge observations from the CPC US-Mexico daily precipitation analysis were also examined. CPC US-Mexico is available as daily total precipitation values only. The CPC US-Mexico daily analysis has 1° × 1° spatial resolution, with over 8000 rain-gauges covering a domain that includes all of the United States and Mexico (Higgins et al. 2000). Mexican precipitation data for the CPC US-Mexico analysis comes from about 900 rain-gauges, monitored by the Mexican National Weather Service (Shi et al. 2005). For comparison purposes, data from the NAME Event Rain-gauge Network (NERN) was also obtained. NERN consists of 87 tipping-bucket rain-gauges, installed in 2002 and 2003 in roughly east-west transects along the Sierra Madre Occidental between approximately 23°N and 30°N, for the purposes of NAME (Gochis et al. 2003; Gochis et al. 2004). NERN is available in 3-hour intervals.

b. Reanalysis and model products

The North American Regional Reanalysis (NARR) is a long-term, dynamically consistent, high-resolution, high-frequency, atmospheric and land surface hydrology dataset for the North American domain (Mesinger et al. 2006). Precipitation in NARR is assimilated, and over the continental U.S. and Mexico is obtained by the disaggregation of a daily rain-gauge analysis (see Shafran et al. 2004). Over the continental U.S., the daily analysis is disaggregated to hourly using temporal weights derived from a 2.5º x 2.5° latitude-longitude analysis of hourly rain-gauge data; over Mexico, the 24-hour analysis is disaggregated using the T62-resolution NCEP-DOE Global Reanalysis 2

precipitation forecasts (Kistler et al. 2001, Mesinger et al. 2006). NARR has a 32-km, 45-layer resolution, and the 3-hourly output is used for the present study. This fine horizontal and vertical grid allows for the study of features such as the Gulf of California, which the NCEP-NCAR or NCEP-DOE global reanalyses, with a resolution of about 2.5° latitude x 2.5° longitude, do not resolve. Originally completed for the period 1979-2002, NARR has been continued in near-real time, and the months of the NAME Field Campaign have recently become available. The seasonal evolution of the Monsoon obtained from NARR has been found to be largely consistent with observations (Mo et al. 2005). It has also been found (Mo et al. 2005) that NARR systematically overestimates the water vapor transport by the Gulf of California Low-Level Jet (GCLLJ). The too-strong meridional winds have largest bias on the northern Gulf of California. Nevertheless, NARR captures the diurnal cycle of the meridional wind quite well (Mo et al. 2005), with minimum wind speeds at about 1600 LT, and maximum at about 0100 LT.

Model forecasts for the 2004 summer season are produced with the workstation version of NCEP's Eta model, which was run at 22-km grid spacing, with 45 vertical levels; the output is available at 3-hour intervals. The model is initialized from the Global Forecasting System (GFS) analysis, and the domain covers the area between 15°N and 45°N, 120°W and 90°W—roughly the same domain as NAME Tier II (Higgins et al. 2006). The 12-36 hour forecasts are employed for this analysis, thus avoiding spin-up effects in the first 12 hours.

c. Daily rain rate from empirical, model, and reanalysis products

Figure 1 illustrates the average daily rainfall in the western Mexico/southwestern U.S. for the CMORPH, CPC US-Mexico, RMORPH, NARR, and Eta Model analyses. As the NERN domain is small relative to the other data sources, it is not shown, but has been examined to compare the intensity of daily rain rates. In all of the representations, the core monsoon region can be seen clearly, extending from about 20°N to 30°N along the Sierra Madre Occidental mountain range (SMO) and the coastal plain in western Mexico. There is reasonable spatial agreement between the five: all show the core region, the extension of the monsoon into southern Arizona, and another peak area of precipitation in northeastern New Mexico.

All five analyses report the highest daily rain rate of the entire NAME domain occurring along the western slopes of the SMO. Predictably, the rain rate of both RMORPH and NARR resemble the CPC US-Mexico daily precipitation analysis, as this rain-gauge data is used in the production of both. With the exception of CMORPH, all the analyses produce a daily rain rate in the range of 4-10 mm d^{-1} for most of the core region. Examination of the CMORPH estimates finds, as expected, a greater (and probably unrealistic) rain rate, with values of 8-22 mm d^{-1} throughout the core region. The Eta model forecasts are generally slightly greater than the rates in the central core region from the other estimates, except CMORPH.

While the core region appears clearly in all analyses, the distribution of rainfall intensity varies between the analyses. The region of most intense precipitation (greater than 10 mm d^{-1}) in the RMORPH, CPC US-Mexico, and NARR analyses is in the coastal region of 22°N, just to the south of the opening of the Gulf of California. Examination of precipitation time-series of the CPC US-Mexico rain-gauge data reveals this is unlikely to

be due to a single very high event, as this area records consistently higher precipitation than other regions. The area of maximum rain rate in the Eta model forecasts (about 8-9 mm d^{-1}) and in CMORPH (18-22 mm d^{-1}) occurs along the western SMO, between about 23°N and 27°N.

3. Main features of the diurnal cycle of precipitation and associated fields

Precipitation over the core region of the North American Monsoon, along the western slopes of the Sierra Madre Occidental, is considerably greater than in the northern reaches of the Monsoon, southern Arizona and New Mexico (see Figure 1). Therefore, the diurnal cycles of precipitation and some of its associated fields have been analyzed separately in the core region and in the southwestern US.

a. Structure and evolution of the diurnal cycle of precipitation in the core monsoon region

The diurnal cycle of the core region of the Monsoon is inspected using Hovmoeller (time-longitude) diagrams of observed and forecast precipitation, similar to the methods used by Lang et al. (2006) to analyze radar observations. The diurnal cycle is first identified using RMORPH satellite estimates, NARR, and Eta model forecasts. All figures are presented in local time, and the period of display is from local noon to local noon, in order to present the continuous diurnal cycle. Figure 2 depicts the diurnal cycle of precipitation in the core region of the monsoon, between 22°N and 30°N, 112°W and 102°W, for RMORPH satellite estimates (left-hand column), NARR (center column),

and Eta model forecasts (right-hand column). The precipitation has been averaged by 1° latitude bands; Figure 2 shows every other band.

The area near 22°N, the southern extent of the core monsoon area, was earlier found to have a heavier daily rain rate than the rest of the core monsoon region in NARR and RMORPH. This, and the geographic difference of this area lying to the south of the Gulf of California, suggests an analysis of the diurnal cycle in this area separate from the rest of the core region is in order. In this latitude band, the initiation of precipitation in RMORPH and NARR takes place around 1500-1800 LT, with NARR beginning slightly earlier than RMORPH. For these two analyses, the most intense average precipitation rate is about 1.0-1.2 mm hr^{-1}, and in RMORPH occurs between midnight and about 0300 LT; for NARR, about 1800-2400 LT. The Eta model differs from NARR and RMORPH in that it shows a lower (0.5-0.6 mm hr^{-1}) and later (0300-0600 LT) maximum 3-hr average rain rate.

In the region of 24°N-28°N, all three analyses show the diurnal cycle characterized by the initiation of precipitation, at an average rate of 0.1 mm hr^{-1}, over the crest of the Sierra Madre Occidental (SMO) in the afternoon, with NARR beginning earliest (about 1300 LT), RMORPH beginning around 1400-1500 LT, and the Eta model slightly after 1500 LT. NARR is the most consistent with the NERN rain-gauge results of Gochis et al. (2004), which show precipitation in the highest elevation bands beginning to increase at about 1300 LT.

The maximum precipitation rate for these latitude bands occurs along the western slopes of the SMO. RMORPH and NARR show peak rates of precipitation of around 0.7 mm hr^{-1} in this central core region, with the highest rates at 26°N to 28°N. For these two

analyses, the beginning of maximum precipitation rates take place over the range of 1800-2400 LT, with the NARR maximum precipitation rates starting earlier than RMORPH. Eta forecasts show a peak rate of 1.0-1.2 mm hr^{-1} in this region, slightly displaced to the south. The rainfall diurnal cycle is generally a minimum by about 0300 LT, over the coastal plain.

Previous studies have identified a downslope propagation of the diurnal maximum of precipitation over the western slopes of the Sierra Madre Occidental (Gochis et al. 2004, Yarosh et al. 2005, Lang et al. 2006). This behavior is noticeable here in the Hovmoeller diagrams of all three data sets. In this downslope propagation in the core Monsoon region, lighter precipitation occurs earlier in the day at higher elevations, while peak rates of precipitation occur later at lower elevations. The diurnal evolution is completed over the coastal plain and the Gulf of California. The downslope shift of precipitation throughout the course of the day is particularly visible in the RMORPH and NARR data, but can be seen as well in the Eta model output.

An approximation of the speed of the downslope propagation of this signal was obtained by drawing a line along the maximum values in each Hovmoeller diagram (See Fig. 2b, central panel, for an example); the slope of this line represents the speed of propagation. The slope of this line (speed) has been calculated for each degree of latitude. The results of this analysis are presented in Figure 3. RMORPH, NARR, and the Eta model all show speeds of downslope propagation near zero at 20°N. Maximum speeds occur between 22°N and 28°N, the area lying along the main body of the Gulf of California. NARR shows a speed over 6 m s^{-1} in most of the core region, with a peak speed of nearly 8 m s^{-1}, in line with the results of Lang et al. (2006). RMORPH shows

slower peak speeds, about 5 m s^{-1}. While NARR and RMORPH are produced using the same daily precipitation analysis, different disaggregation methods are used in their production, and differences appear between their diurnal cycles, such as the speed of the westward shift. The Eta model shows a yet slower speed of westward shift, around 2.5 m s^{-1}.

b. Associated fields of the diurnal cycle in the core region

The evolution of the diurnal cycle of precipitation, and the downslope propagation of the precipitation maximum observed in the diurnal cycle, have been further assessed by the combined analysis of several associated fields. These include convective available potential energy (CAPE), convective inhibition (CIN), and the moisture flux convergence. An additional factor, evaporation, has also been analyzed, in the interest of understanding the sources of atmospheric moisture. It is hypothesized that evaluating the strength of these associations will provide insight into the diurnal cycle of precipitation.

CAPE is the maximum energy available to an ascending air parcel, while CIN is the amount of energy required to lift a parcel of air from the surface to the level of free convection. In the core region, CAPE increases from near zero before Monsoon onset in early July to values well over 1000 J kg^{-1}, and considerably larger instant values, during its mature phase (Barlow et al. 1998). Vertically-integrated moisture flux convergence (MFC) represents dynamically transported moisture, while evaporation provides a local source of precipitable water in the atmosphere. The Gulf of California presents a large source of moisture for the northwestern Mexico region, and previous studies of the seasonal evolution of moisture flux (e.g. Higgins et al. 1997, Barlow et al 1998) have

found close agreement between the onset of the Monsoon and an increase in MFC in the core monsoon region. All of these fields, while interrelated, may be individually analyzed to assess the strength of association between their diurnal cycles and that of precipitation.

Figure 4 depicts Hovmoeller diagrams of the diurnal cycle of the previous terms. The July and August 2004 diurnal cycle of CAPE anomalies (left column) and of MFC for the core monsoon region were obtained from NARR. The daily average of CAPE, which ranges from about 3000 J kg^{-1} over the Gulf of California to about 200 J kg^{-1} over the coastal plain and western SMO, has been removed to highlight the diurnal variation. As in Figure 2, in order to present the continuous diurnal cycle, the figures are from local noon to local noon, and precipitation contours from NARR have been overlain.

In the afternoon and evening, a maximum in CAPE occurs over the western slopes of the SMO and the coastal plain, with a minimum over the Gulf of California. CAPE builds up over the land throughout the afternoon, and the maximum over land occurs around 1800 LT, shortly after the warmest part of the day. Between midnight and 0900 LT, when the waters of the Gulf of California are warmer than the land, higher CAPE forms over the Gulf of California, and a minimum appears over the land. The middle three panels of the left side of Figure 4 show latitudes 24°N-28°N, the area along the Gulf of California, where the diurnal cycle of CAPE has two maxima: one in the afternoon/evening over land, and one over the Gulf after midnight. This second maximum represents a much smaller variation from the average, as the daily average of CAPE over the Gulf of California is much greater than that over the land. The bottom panel, 22°N, is south of the Gulf of California, and there is no post-midnight second

maximum: rather, CAPE peaks over the land in the evening, and decreases steadily to the west throughout the rest of the night.

Figure 4 also shows mid-afternoon moisture flux divergence over the Gulf of California and MFC over the western slopes of the Sierra Madre Occidental, similar to the results of Berbery (2001). The core region experiences afternoon upslope flow (Stensrud et al. 1995; Johnson et al. 2005) that brings moisture in from the Gulf of California and converges against the western slopes of the SMO. MFC at all latitudes peaks around 1800-2100 LT. Figure 4 shows post-midnight MFC along the coastal plain: by midnight, upslope flow has dissipated and southerly flow has developed along the Gulf of California and the coastal plain (Douglas 1995), which, coupled with downslope flow off the SMO, leads to this pattern of MFC. The strongest MFC appears to precede the peak precipitation by about three hours. MFC is weakest at 30°N, where the slope of the SMO is the most gradual, and the distance to the Gulf of California the greatest. It is strongest at 22°N, where the coastal plain is very narrow and the slope of the SMO is steep. The diurnal pattern of MFC (Figure 4) shows evidence of a westward propagation similar to that of precipitation, with the MFC diurnal maximum occurring slightly before the precipitation maximum, and the area of MFC moving off to the west throughout the day, diminishing in magnitude. In the region of 24°-28°N, similar to CAPE, a smaller, secondary maximum in both precipitation and MFC can also be noted over the Gulf of California in the post-midnight hours.

In order to compare the timing of precipitation and the associated fields in the core region, the land-only mean diurnal cycle area average of precipitation, MFC, evaporation, CAPE, and CIN are shown in Figure 5. NARR results are complemented

with Eta model forecast computations. The area between 20°N and 30°N and 111°W to 104°W is shown. Intensities in the core region have been damped by the area averaging, as the core region is a narrow strip along the western slopes of the SMO and the coastal plain. NARR (left panel) shows MFC and precipitation both peaking at about 2100 LT. CAPE peaks about three hours before peak precipitation, and coincides with the minimum in CIN. Evaporation peaks during the warmest part of the day, about six hours before peak precipitation. Compared to the Eta model results, NARR shows higher evaporation and CAPE and lower MFC for the core region. The higher evaporation may be related to the higher sea surface temperatures along the Gulf of California that NARR employed (see Mesinger et al. 2006).

c. The diurnal cycle of precipitation and associated fields in southern Arizona and New Mexico

While the North American Monsoon is very important in the southwestern United States, supplying up to 60% of the annual precipitation (Douglas et al. 1993), the daily precipitation rain rate is only on the order of 1-2 mm d^{-1}, contrasted with the more than 8 mm d^{-1} in the core region. The southwestern U.S. is subject to neither land-water contrasts nor to the sloping of the SMO, and the average precipitation diurnal cycle does not exhibit a westward shift. Area averages of the region between 32°N and 36°N, 113°W-104°W have been used to analyze the diurnal cycle of precipitation and its associated fields in southern Arizona and New Mexico (Fig. 6). As stated earlier, Mo et al. (2005) found that NARR systematically overestimates the Gulf of California LLJ water transport, producing too-strong winds at the surface and aloft. As a result of this

bias, the corresponding MFC is much stronger in NARR than in the Eta model forecasts. For this reason, alongside NARR results, the Eta model forecasts are employed as a more realistic representation of the moisture fluxes.

The diurnal cycle in NARR (Fig. 6a) shows a minimum in all factors (precipitation, MFC, evaporation, CAPE, and a maximum in CIN magnitude) at about 0600-0900 LT, soon after the diurnal temperature minimum. As the surface temperature warms, evaporation and CAPE increase to their diurnal maxima at about 1500 LT. The precipitation rate peaks at about 1800 LT, and MFC also has a peak at this time, similar to the findings of Anderson and Kanamaru (2005). MFC decreases after 1800 LT, until about midnight, and peaks again at about 0300 LT. This second peak may be the result of the nocturnal low-level jet (LLJ) over the Gulf of California, which generally peaks at about 0100 LT (Douglas 1995; Douglas et al.1998; Mo et al. 2005). This LLJ brings moisture north from the Gulf into the southwestern United States (Douglas 1995).

For the reasons already discussed, the NARR diurnal cycle, with strong convergence around 0300 LT, values near zero during the morning and early afternoon, and convergence again in the late afternoon, may be biased. The Eta model, on the other hand, shows weak convergence in the morning and relatively strong divergence in the afternoon and evening. MFC peaks about 12 hours before precipitation peaks, suggesting a weaker association between these two fields than between CAPE and precipitation, as CAPE peaks three to six hours before precipitation. In summary, precipitation, CAPE, CIN, and evaporation are similar in timing and magnitude for both NARR and the Eta model forecasts, and the major difference between the two is found in MFC. However, in

order to better understand the links between precipitation and other variables, it is necessary to separate surge and no-surge cases, as will be discussed next.

d. Moist surges and precipitation in the core region and the southwestern U.S.

Thus far the discussion has been on time-mean conditions over the southwestern U.S. However, northward surges of cool, moist air along the Gulf play a critical role in the precipitation mechanisms in the southwestern United States (Douglas and Leal 2003; Higgins et al. 2004). Abrupt changes in the low-level moisture flux have been identified as a distinct component of moisture surges (Douglas and Leal 2003), and surges have been found to account for a majority of the precipitation in Arizona in model simulations (Berbery and Fox-Rabinovitz 2003) and in observations (Higgins et al. 2004). Surges are usually produced by the passage of an easterly wave; stronger surges are formed when a midlatitude disturbance occurs in conjunction with the passage of the easterly wave (Stensrud et al. 1997).

Moisture surges were identified here as when the 950-hPa meridional moisture flux of the Eta model forecasts in the northern Gulf of California equals or exceeds the mean plus 50% of the standard deviation, following the method of Berbery and Fox-Rabinovitz (2003). All other cases are deemed to be non-surge times. Due to the aforementioned overestimation of meridional moisture transport in NARR, Eta model forecasts were used for this calculation. Many surge indices have been proposed (e.g. Fuller and Stensrud 2000; Higgins et al 2004), and this definition simply takes into account strong moisture flux cases, which have traveled to the north of the Gulf of California. Tests with the meridional moisture flux threshold computed at points in the

southern and central Gulf of California (not shown) produced a greater number of high moisture flux periods, but these were of shorter duration than the four periods seen when the northern Gulf is analyzed.

Figure 7 presents the percentage of total July-August 2004 precipitation that occurred during surge events, estimated from the Eta Model forecast and RMORPH data. The total amount of precipitation that fell during surges was compared to the total precipitation of the entire two-month period to produce this figure. NARR precipitation is similar to RMORPH and thus for simplicity is not shown. In most of the core region, both the Eta model and RMORPH show only a moderate dependence on surges, with generally between 30% and 50% of precipitation occurring during surges, similar to the findings of Douglas and Leal (2003). In the southwestern United States, both the Eta model and RMORPH show high percentages of precipitation occurring during surges, (upwards of 70%), also in line with the results of Douglas and Leal (2003). During surges, both Eta forecasts and RMORPH show high percentages of precipitation occurring in southern California and Arizona. The major difference between the two datasets is in a small area of the western coastline of the northern portion of the Gulf of California, where RMORPH shows high percentages of precipitation occurring during surges. This percentage decreases to the east, with a minimum over the northern peaks of the SMO. Conversely, the Eta model shows lower percentages along the coast, increasing to the east.

The meridional moisture flux in the northern Gulf of California from the Eta model and NARR is shown in the top panel of Figure 8; as expected, NARR is generally (although not always) stronger than the Eta model, likely due to NARR's bias in

meridional winds of the Gulf of California LLJ. The lower two panels of Figure 8 illustrate the time-series of precipitation for both the Eta model forecasts and for NARR for the period of 10 July through 31 August 2004; surge times are marked with shaded areas. Two areas are shown: area-averaged southern Arizona and New Mexico, between 32°N and 36°N, 113°W and 104°W, and the core monsoon region, between 20°N and 30°N, from 111°W to 104°W. Both Eta model output and NARR are displayed as 8-point running means of 3-hour data, in order to remove the diurnal cycle of the time series. In this analysis, four surge periods are observed, covering approximately July 12-16, July 23-27, August 10-17, and August 23-24. Tropical Storm Blas, occurring 11-15 July 2004, appears as a strong meridional moisture flux and precipitation event, and produced a strong surge (Higgins et al. 2006). During the period 22 July to 26 July, widespread thunderstorms were observed in the Tier I NAME region (NAME Field Catalog), and this period featured a strong surge as well (Johnson et al. 2006).

In the core region, NARR tends to show a more uniform distribution of precipitation, giving less relevance to surge/no-surge cases. On the other hand, Eta model forecasts are more sensitive to surge/no-surge cases, generally showing more precipitation during surges than NARR, but less precipitation than NARR during non-surge times. While large amounts of precipitation occur in the core region during the two July surge periods, precipitation during the major August surge is not particularly strong, and several smaller but distinct periods of high precipitation occurred on days without a surge.

In southern Arizona and New Mexico, maximum precipitation occurs during surge times, as represented in both the Eta model forecasts and NARR. Eta model

precipitation forecasts are generally slightly higher than NARR in the Arizona and New Mexico area average, especially during surge times. Three of the four strong precipitation events in Arizona coincided with a moisture surge.

e. Dependence of the diurnal cycle in the southwestern U.S. on surges

Given the importance of surges for precipitation in the southwestern U.S., we now separately examine the diurnal cycle of precipitation and of its associated fields in southern Arizona and New Mexico for surge and non-surge times, as defined earlier in this section. In order to check how representative was the summer of 2004, with respect to other years, a four-year NARR climatology computed over July, August, and September of 2002 through 2005 is also presented for surge and non-surge times. In this case, in the absence of the Eta model forecasts to compute the moisture flux index that defines the surge and no-surge cases, the operational NCEP Eta Data Assimilation System (EDAS) analysis was employed.

First, the surge and non-surge daily average for precipitation, evaporation, MFC, CAPE, and CIN for NARR, including the 4-year climatology and the NAME 2004 field campaign season, and for the Eta Model are shown in Table 1. Looking at this table, some generalizations can be drawn from comparing the results for surges to the results of non-surge times, for all three datasets. The daily average for precipitation is about twice as high during surges than in no-surge cases, while evaporation has a very similar daily average during both surges and non-surge times. CAPE is also nearly doubled during surges, unlike CIN that exhibits a small increase in magnitude. The field that shows the greatest difference between surges and non-surge times is MFC, as expected. The daily

average magnitude of MFC is considerably higher during surges. Furthermore, examination of the 2004 season from NARR finds that the daily averages for both surges and non-surges are very similar to their counterparts in the four-year climatology of NARR, indicating that 2004 is a representative season.

As in Figure 6, Figure 9 shows the area-averaged diurnal cycle of precipitation, evaporation, MFC, CAPE and CIN, for NARR and for the Eta model. Figs. 9a and 9b show that the four-year NARR climatology is generally similar to the patterns during the NAME 2004 field campaign of July and August, i.e., Figures 9c and 9d. According to Figures 9c and 9d, the NARR precipitation rate peaks about three hours earlier in the day during surges (1800 LT) than in the non-surge cases (2100 LT), and at higher intensities. On the other hand, evaporation exhibits a very similar diurnal evolution and daily average (see Table 1) during surges as to non-surge times. CIN has a higher peak in the morning hours during surges, but drops off to a minimum by 1800 LT that is approximately the same magnitude as the minimum seen in the non-surge case. CAPE shows higher intensities throughout its diurnal cycle.

Table 1 showed an important increase in MFC during surges both in NARR and Eta model forecasts. Changes are found in the evolution of the diurnal cycle as well, as seen in Fig. 9. In the case of NARR, three MFC peaks are noticed: at 0300, 0900, and 1800 LT. When each of the four years used for the surge climatology (Fig. 9a) were analyzed individually (not shown) similar multi-peak patterns were found in the MFC diurnal cycles, with the peaks occurring at various times throughout the four cycles. On the other hand, when the non-surge MFC diurnal cycles were analyzed, all four years exhibited very similar patterns to each other and to the four-year average. While the

rather unclear, multi-peak pattern seen in the surge cases may be attributed to the effect of individual surge cases (four surge cases in the 2004 season, for example), it is also possibly due to the inaccurate representation of the meridional moisture fluxes in the north of the Gulf of California. Notice that the Eta model forecasts have a seemingly more consistent behavior: in the no-surge case (Fig. 9f) the MFC remains close to zero and even becomes negative (divergence) during part of the day. Therefore, it does not seem to have a strong association with the development of precipitation. However, during surges, MFC develops a better-defined diurnal cycle with a maximum preceding precipitation by about 6 hours, suggesting a stronger association between this field and precipitation during surges.

4. Summary and conclusions

The purpose of this study has been to analyze the structure of the diurnal cycle of precipitation and associated fields during the North American Monsoon Experiment (NAME) Field Campaign of July and August 2004. A proper representation of physical mechanisms, such as the diurnal cycle, is essential to understanding and predicting warm season precipitation in North America. The analysis was conducted using RMORPH satellite estimates, derived from the disaggregation of the Climate Prediction Center (CPC) US-Mexico daily rain-gauge analysis via CMORPH satellite estimates, model forecasts from the workstation version of NCEP's Eta model, and reanalysis data from the North American Regional Reanalysis (NARR). The CPC US-Mexico rain-gauge and NAME Event Rain-gauge Network (NERN) analyses were also examined for comparison purposes.

The Tier I NAME region was examined both as a whole and as two separate regions: the core monsoon region along the western side of the Sierra Madre Occidental, and the southwestern United States. Due to the importance of northward surges of moist air from the Gulf of California into the southwestern U.S., the effect of surges on the diurnal cycle was examined for this region as well. This study looked at the precipitation diurnal cycle and several associated fields, including evaporation, the convective available potential energy and convective inhibition, as well as the moisture flux convergence.

NARR, Eta model forecasts, and RMORPH satellite estimates produce very similar patterns and daily average precipitation, and correspond well to rain-gauge observations. On the other hand, CMORPH satellite precipitation estimates systematically produce high daily rain rates, up to three times as high as the other sources.

Comparison of RMORPH estimates, NARR, and Eta model forecasts revealed similar diurnal cycles in the core monsoon region. The 24-hour cycle of precipitation begins in the afternoon along the crest of the Sierra Madre Occidental (SMO), reaching peak rates around 2100 LT along the western slopes of the SMO, with precipitation ending in the early morning hours over the coastal plain. Consistent with previous studies, a westward shift of precipitation is seen in the core region: the precipitation cycle initiates and completes earlier at higher topographical elevations, and later towards the west. This westward shift moves at different speeds over the range of the core monsoon region depending on the latitude, with the highest speeds occurring in the region of 24°N-28°N, where the Sierra Madre Occidental reaches the highest elevations.

Although NARR and RMORPH start with the same daily rain-gauge database, the two use different methods to disaggregate the daily precipitation, and important differences can be noticed in their representation of the diurnal cycle. The NARR precipitation diurnal cycle generally begins earlier in the day than RMORPH, and NARR shows a faster westward shift of the precipitation maximum throughout the day than RMORPH. As stated, these differences may be in part related to the difference in resolution of the disaggregating methods: According to Mesinger et al. (2006) the sub-diurnal variability over Mexico is obtained from the NCEP-DOE Global Reanalysis 2. The diurnal cycle of RMORPH results from the satellite estimates derived by Joyce et al. (2004) for the 0.25° x 0.25° CMORPH dataset. The Eta model precipitation diurnal cycle generally starts later than the other two, and exhibits a slower, less distinct westward shift.

Several fields associated with the diurnal cycle of precipitation in the core monsoon region were examined using information from NARR, including CAPE and CIN and the vertically-integrated MFC. MFC exhibits a westward shift similar to that of precipitation, with the maximum occurring in the late afternoon, shortly before the precipitation maximum, and moving to the west throughout the evening. The CAPE diurnal cycle has two maxima, one in the afternoon over the coastal plain, and one in the early morning over the Gulf of California.

Northward moisture surges along the Gulf of California produce a noticeable increase in precipitation in the northern edge of the monsoon region, specifically the southwestern U.S. Generally, the diurnal cycle in non-surge cases resembles the overall average, probably reflecting the greater frequency of no-surge cases. Surges produce

higher precipitation and an altered diurnal cycle in some of the associated fields, especially MFC. In the Eta model, the moisture flux has a poorly-defined diurnal cycle in non-surge cases and remains divergent throughout the day, but during surges it becomes convergent and acquires a well-defined evolution with a peak about six hours before peak precipitation, suggesting that MFC has a greater role in precipitation during surges. During surges, as seen in both NARR and the Eta model, CAPE and CIN have modifications only to the amplitude of their cycles. As also seen in previous studies, NARR appears to overestimate the meridional transport of water in this region.

Acknowledgements

The authors would like to thank Dr. Bruce Anderson, Dr. Steve Nesbitt, and one anonymous reviewer for their thoughtful comments and suggestions that improved our manuscript. We are thankful to Drs. Wei Shi and John Janowiak for supplying the RMORPH dataset, and Dr. Wayne Higgins for his suggestions. We would like to thank Dr. David Gochis for supplying the NERN dataset, and for his comments. This work was supported by NOAA grants NA17EC1483 and NA04OAR4310164.

References

Adams, D.K, and A.C. Comrie, 1997: The North American Monsoon. *Bull. Amer. Meteor. Soc.*, **78**, 2197–2213.

Anderson, B.T., J.O. Roads, and S-C. Chen, 2000: Large-scale forcing of summertime monsoon surges over the Gulf of California and the southwestern United States. *J. Geophys. Res.*, **105**, 24,455-24,467.

----, ----, ----, and H-M.H. Juang, 2001: Model dynamics of summertime low-level jets over northwestern Mexico. *J. Geophys. Res.*, **106**, 3401-3413.

----, and H. Kanamaru, 2005: The Diurnal Cycle of the Summertime Atmospheric Hydrologic Cycle over the Southwestern United States. *J. Hydromet.*, **6**, 219-228.

Barlow, M., S. Nigam, and E.H. Berbery, 1998: Evolution of the North American Monsoon System. *J. Climate*, **11**, 2238-2257.

Berbery, E.H., 2001: Mesoscale Moisture Analysis of the North American Monsoon. *J. Climate*, **14**, 121-137.

----, and M.S. Fox-Rabinovitz, 2003: Multiscale Diagnosis of the North American Monsoon System Using a Variable-Resolution GCM. *J. Climate*, **16**, 1929-1947.

Bordoni, S., P.E. Ciesielski, R.H. Johnson, B.D. McNoldy, and B. Stevens, 2004: The low-level circulation of the North American Monsoon as revealed by QuikSCAT. *Geophys. Res. Lett.*, **31**, doi:10.1029/2004GL020009.

Douglas, M.W., R.A. Maddox, and K. Howard, 1993: The Mexican Monsoon. *J. Climate*, **6**, 1665-1677.

----, 1995: The Summertime Low-Level Jet over the Gulf of California. *Mon. Wea. Rev.*, **123**, 2334-2348.

----, A. Valdez-Manzanilla, and R.G. Cueto, 1998: Diurnal Variation and Horizontal Extent of the Low-Level Jet over the Northern Gulf of California. *Mon. Wea. Rev.*, **126**, 2017-2025.

----, and J.C. Leal, 2003: Summertime Surges over the Gulf of California: Aspects of Their Climatology, Mean Structure, and Evolution from Radiosonde, NCEP Reanalysis, and Rainfall Data. *Wea. Forecasting*, **18**, 55-74.

Farfan, L.M., and J.A. Zehnder, 1994: Moving and stationary mesoscale convective systems over northwest Mexico during the Southwest Area Monsoon Project. *Wea. Forecasting*, **9**, 630-639.

Fawcett, P.J., J.R. Stalker, and D.S. Gutzler, 2002: Multistage moisture transport into the interior of northern Mexico during the North American summer monsoon. *Geophys. Res. Lett.*, **29**, doi:10.1029/2002GL016593.

Fuller, R.D., and D.J Stensrud, 2000: The Relationship between Tropical Easterly Waves and Surges over the Gulf of California during the North American Monsoon. *Mon. Wea. Rev.*, **128**, 2983-2989.

Gochis, D.J., J.-C. Leal, C.J. Watts, W.J. Shuttleworth, and J. Gartuza-Payan, 2003: Preliminary diagnostics from a new event-based monitoring system network in support of the North American monsoon experiment (NAME). *J. Hydromet.*, **4**, 235-250.

----, A. Jimenez, C.J. Watts, J Garatuza-Payan, and W.J. Shuttleworth, 2004: Analysis of 2002 and 2003 Warm-Season Precipitation from the North American Monsoon Experiment Event Rain Gauge Network. *Mon. Wea. Rev.*, **132**, 2938-2953.

Hales, J.E., 1972: Surges of Maritime Tropical Air Northward Over the Gulf of California. *Mon. Wea. Rev.*, **100**, 298-306.

----, 1974: Southwestern United States Summer Monsoon Source—Gulf of Mexico or Pacific Ocean? *J. Applied Met.*, **13**, 331-342.

Higgins, R.W., Y. Yao, and X.L. Wang, 1997: Influence of the North American Monsoon System on the U.S. Summer Precipitation Regime. *J. Climate*, **10**, 2600-2621.

----, W. Shi, E. Yarosh, and R. Joyce, 2000: Improved United States Precipitation quality control system and analysis. NCEP/Climate Prediction Center ATLAS No.7, 40pp, http://www.cpc.ncep.noaa.gov/research_papers/ncep_cpc_atlas/7/index.html.

----, ----, and C. Hain, 2004: Relationships between Gulf of California Moisture Surges and Precipitation in the Southwestern United States. *J. Climate*, **17**, 2983-2995.

----, ----, 2005: Relationships between Gulf of California Moisture Surges and Tropical Cyclones in the Eastern Pacific Basin. *J. Climate*, **18**, 4601-4620.

----, and coauthors, 2006: The NAME 2004 Field Campaign and Modeling Strategy. *Bull. Amer. Meteor. Soc.*, **87**, 79-94.

Howard, K.W. and R.A. Maddox, 1988: Mexican mesoscale convective systems—A satellite perspective. Preprints, *Third Int. American and Mexican Congress of Meteorology*, Mexico City, Mexico, Mexican Meteorological Organization, 404-408.

Janowiak, J., P. Xie, R. Joyce, M. Chen, Y. Yarosh, 2004: Validation of daily satellite precipitation estimates over the U.S. Proceedings of the 29th Climate Diagnostics and Prediction Workshop, Madison, WI.

http://www.cpc.ncep.noaa.gov/products/outreach/proceedings/cdw29_proceedings/presentations.shtml

----, V.J. Dagostaro, V.E. Kousky, and R.J. Joyce, 2006: An Examination of Precipitation in Observations and Model Forecasts during NAME with Emphasis on the Diurnal Cycle. *J. Climate*, **20**, 1680-1692.

Johnson, R.H., P.E. Ciesielski, B.D. McNoldy, P.J. Rogers, and R.K. Taft, 2005: Multiscale Variability of the Flow During the North American Monsoon Experiment. *J. Climate*, **20**, 1628-1648.

Joyce, R.J., J.E. Janowiak, P.A. Arkin, and P. Xie, 2004: CMORPH: A Method that Produces Global Precipitation Estimates from Passive Microwave and Infrared Data at High Spatial and Temporal Resolution. *J. Hydromet.*, **5**, 487-503.

Kistler, R., E. Kalnay, W. Collins, S. Saha, G. White, J. Woollen, M. Chelliah, W. Ebisuzaki, M. Kanamitsu, V. Kousky, H. van den Dool, R. Jenne, M. Fiorino, 2001: The NCEP-NCAR 50-year reanalysis: Monthly means CD-ROM and documentation. *Bull. Amer. Meteor. Soc.*, **82**, 247-267.

Lang, T.J., D.A. Ahijevych, S.W. Nesbitt, R.E. Carbone, S.A. Rutledge, and R. Cifelli, 2006: RADAR-Observed Characteristics of Precipitating Systems During NAME 2004. *J. Climate*, **20**, 1713-1733.

McCollum, J.R., W.F. Krajewski, R.R. Ferraro, and M.B. Ba, 2002: Evaluation of biases of satellite rainfall estimation algorithms over the continental United States. *J. Appl. Meteor.*, **41**, 1065-1080.

Mesinger, F., and coauthors, 2006: North American Regional Reanalysis. *Bull. Amer. Meteor. Soc.*, **87**, 343-360.

Mo, K., M. Chelliah, M.L. Carrera, R.W. Higgins, and W. Ebisuzaki, 2005: Atmospheric Moisture Transport over the United States and Mexico as Evaluated in the NCEP Regional Reanalysis. *J. Hydromet.*, **6**, 710-728.

NAME Field Catalog, http://www.joss.ucar.edu/name/catalog/.

Rosenfeld, D., and Y. Mintz, 1988: Evaporation of rain falling from convective cloud as derived from radar measurements. *J. Appl. Meteor.*, **27**, 209-215.

Shafran, P., J. Woollen, W. Ebisuzaki, W. Shi, Y. Fan, R. Grumbine, and M. Fennessy, 2004: Observational data used for assimilation in the NCEP North American Regional Reanalysis. Preprints, *14th Conf. on Applied Climatology*, Seattle, WA, Amer. Meteor. Soc., 1.4.

Shi, W., R.W. Higgins, V.B.S. Silva, and J. Janowiak, 2005: Intercomparison of Characteristics of Daily Precipitation from the NAME Precipitation Assessment Project. *J. Climate*, submitted.

Smith, W.P., and R.L. Gall, 1989: Tropical Squall Lines of the Arizona Monsoon. *Mon. Wea. Rev.*, **17**, 1553-1569.

Stensrud, D.J., R.L. Gall, S.L. Mullen, and K.W. Howard, 1995: Model Climatology of the Mexican Monsoon. *J. Climate*, **8**, 1775-1794.

----, R.L. Gall, and M.K Nordquist, 1997: Surges over the Gulf of California during the Mexican Monsoon. *Mon. Wea. Rev.*, **125**, 417-437.

Yarosh, Y., P. Xie, M. Chen, R. Joyce, J.E. Janowiak, and P.A. Arkin, 2005: Diurnal Cycle in the North American Monsoon. *Bull. Amer. Meteor. Soc.*, **86**, 26-28.

Figure captions

Figure 1: Daily average precipitation (mm d^{-1}) over the North American Monsoon region from July and August, 2004. a) CMORPH satellite estimates, b) CPC US-Mexico daily rain-gauge analysis, c) RMORPH satellite estimates, d) North American Regional Reanalysis, and e) Eta model forecasts. The core monsoon region is clearly visible, along the western slopes of the Sierra Madre Occidental between approximately 30°N and 20°N.

Figure 2: Hovmoeller diagrams of the diurnal cycle of precipitation in the core monsoon region, averaged into 1°-latitude bands. This figure displays every other latitude. The diurnal cycle is shown from local noon to local noon, in order to show the complete cycle; the contour interval is 0.1 mm h^{-1}. From left to right: RMORPH, NARR, and Eta model forecasts.

Figure 3: Speed of westward shift of precipitation over the core monsoon region, as obtained from the slope of the Hovmoeller diagrams of precipitation from RMORPH, NARR, and the Eta model.

Figure 4: Hovmoeller diagrams of the diurnal cycle of CAPE (left) and the vertically-integrated moisture flux convergence, from NARR. Precipitation contours have been overlain. The CAPE contour interval is 100 J kg^{-1}, MFC contour interval is 0.2 kg m^{-2}, and the precipitation contour interval is 0.1 mm h^{-1}. In order to highlight the diurnal

variation, the daily average of CAPE, which ranges from about 3000 J kg^{-1} over the Gulf of California to about 200 J kg^{-1} over the coastal plain and western SMO, has been removed. Both CAPE and the moisture flux convergence have been smoothed by the application of a 9-point smoothing function.

Figure 5: Land-only area average of several elements in the core monsoon region, from NARR (left) and the Eta model, for the 24-hour period beginning at local midnight. The upper panels depict precipitation (solid line, mm h^{-1}), moisture flux convergence (long dash, mm day^{-1}), and evaporation (dotted line, mm h^{-1}). The middle panels are CAPE (J kg^{-1}), and the bottom panels are convective inhibition (CIN, J kg^{-1}).

Figure 6: The same as in Figure 5, for the southwestern United States.

Figure 7: Percentage of precipitation during surge events for RMORPH satellite estimates (left) and Eta model forecasts (right). Blue areas represent greater than 50% of total precipitation occurring during surge events; gray areas are less than 50%. The total amount of precipitation that fell during surges was compared to the total precipitation of the entire two-month period to produce this figure.

Figure 8: a) Meridional moisture flux at 30°N, 114°W, the northern Gulf of California. b) Area averaged precipitation for the southwestern U.S., and c) the core North American Monsoon region (bottom) for July 10–August 31, 2005. From Eta model forecasts (solid) and NARR satellite estimates (dashed); surge times are indicated by shaded regions.

Figure 9: As in Figure 6, for the southwestern United States, divided into surge and non-surge times. 9a) and 9b) show the four-year climatology, from NARR, of this region, divided into surge and non-surge. 9c) and 9d) show the 2004 NAME field campaign period, obtained from NARR; 9e) and 9f) are the 2004 NAME field campaign period, as represented in the Eta model. The upper panels depict precipitation (solid line, mm h^{-1}), moisture flux convergence (long dash, mm day^{-1}), and evaporation (dotted line, mm h^{-1}). The middle panels are CAPE (J kg^{-1}), and the bottom panels are convective inhibition (CIN, J kg^{-1}).

Table 1: Daily average values for surge and non-surge conditions, for the 4-year NARR average, and the NARR and the Eta model 2004 season.

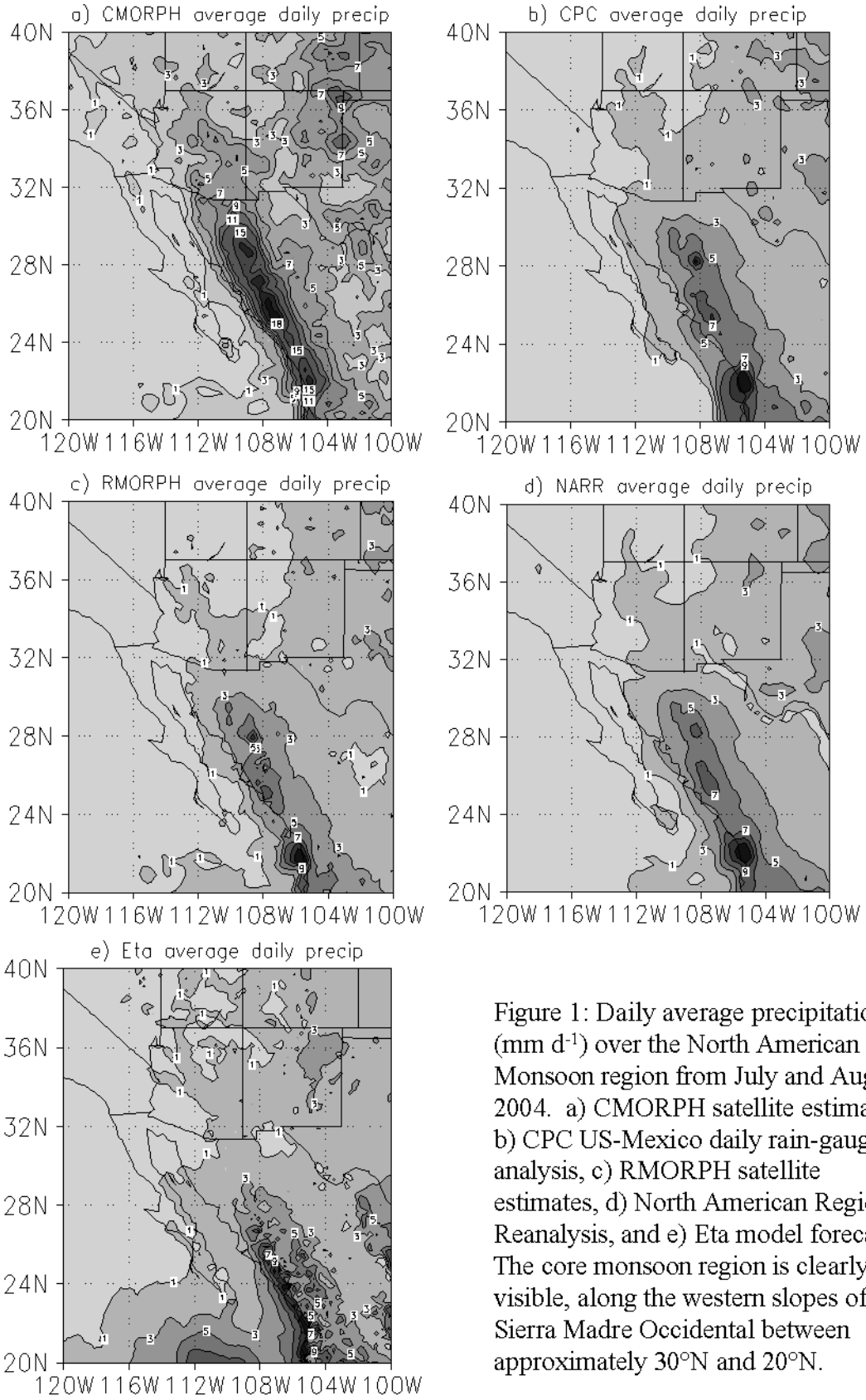

Figure 1: Daily average precipitation (mm d^{-1}) over the North American Monsoon region from July and August, 2004. a) CMORPH satellite estimates, b) CPC US-Mexico daily rain-gauge analysis, c) RMORPH satellite estimates, d) North American Regional Reanalysis, and e) Eta model forecasts. The core monsoon region is clearly visible, along the western slopes of the Sierra Madre Occidental between approximately 30°N and 20°N.

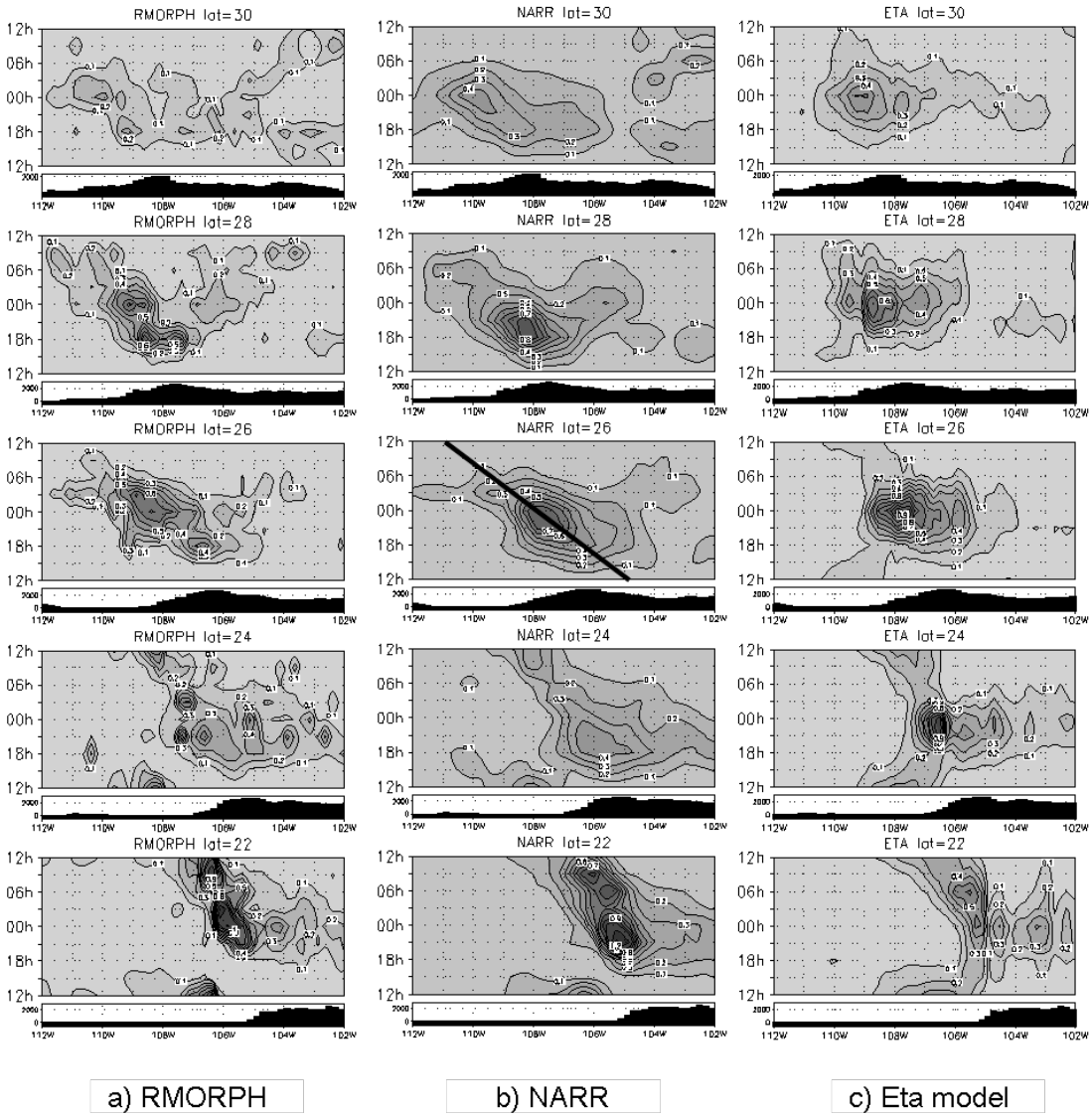

Figure 2: Hovmoeller diagrams of the diurnal cycle of precipitation in the core monsoon region, averaged into 1°-latitude bands. This figure displays every other latitude. The diurnal cycle is shown from local noon to local noon, in order to show the complete cycle; the contour interval is 0.1 mm h^{-1}. From left to right: RMORPH, NARR, and Eta model forecasts. An example of the method used to calculate the speed of the westward shift of precipitation can be seen in the central panel, NARR at latitude 26°N.

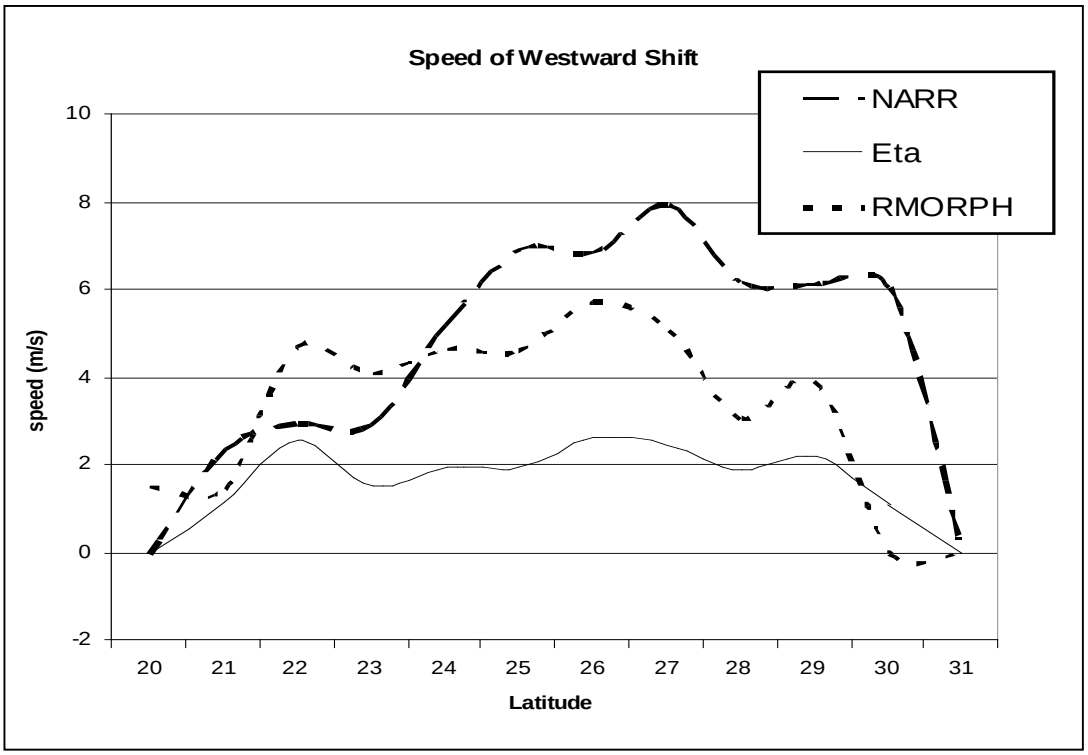

Figure 3: Speed of westward shift of precipitation over the core monsoon region, as obtained from the slope of the Hovmoeller diagrams of precipitation from NARR (long dash), RMORPH (short dash) and the Eta model (solid).

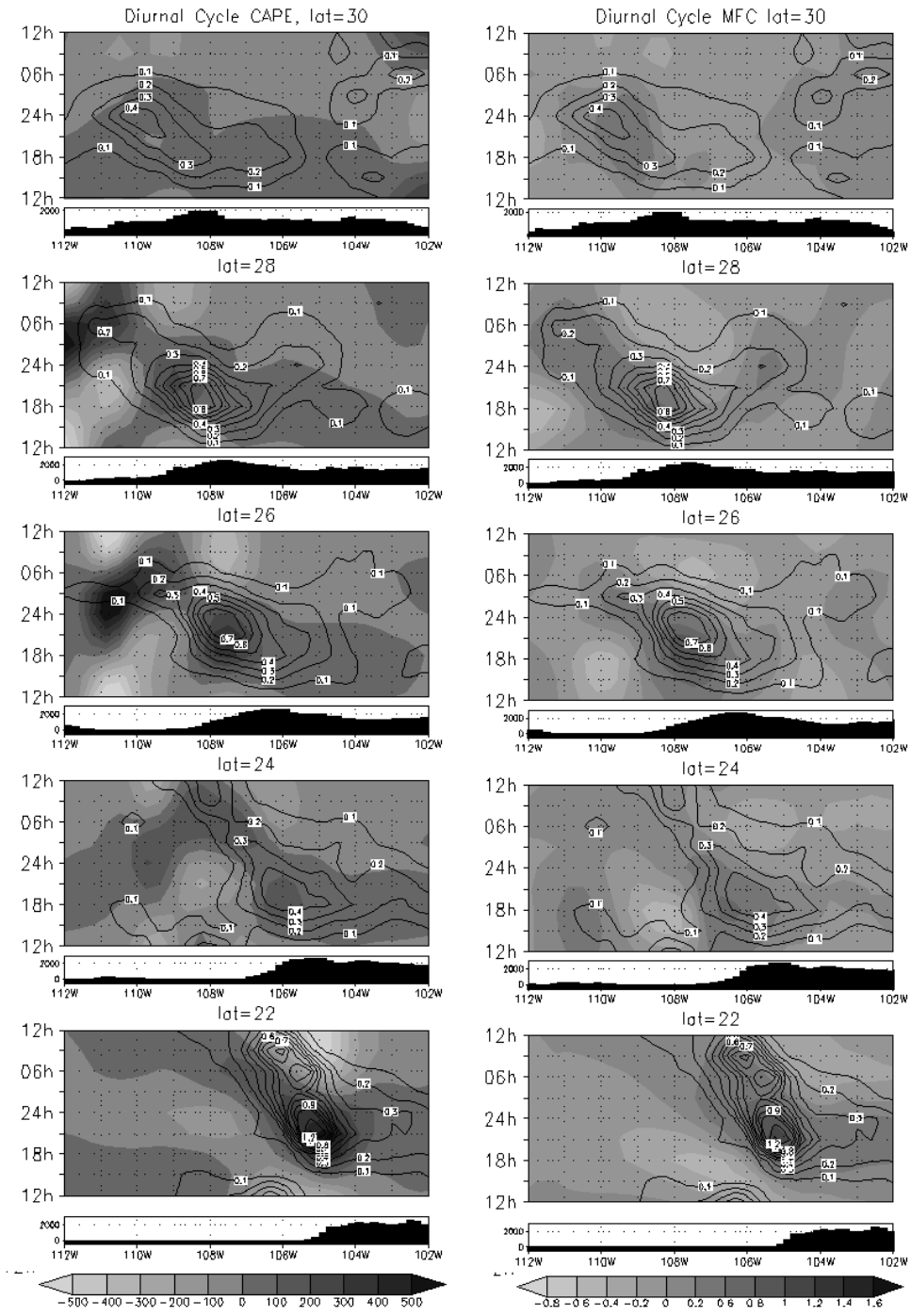

Figure 4: Hovmoeller diagrams of the diurnal cycle of CAPE (left) and the vertically-integrated moisture flux convergence, from NARR. Precipitation contours have been overlain. The CAPE contour interval is 100 J kg^{-1}, MFC contour interval is 0.2 kg m^{-2}, and the precipitation contour interval is 0.1 mm h^{-1}. In order to highlight the diurnal variation, the daily average of CAPE, which ranges from about 3000 J kg^{-1} over the Gulf of California to about 200 J kg^{-1} over the coastal plain and western SMO, has been removed. Both CAPE and the moisture flux convergence have been smoothed by the application of a 9-point smoothing function.

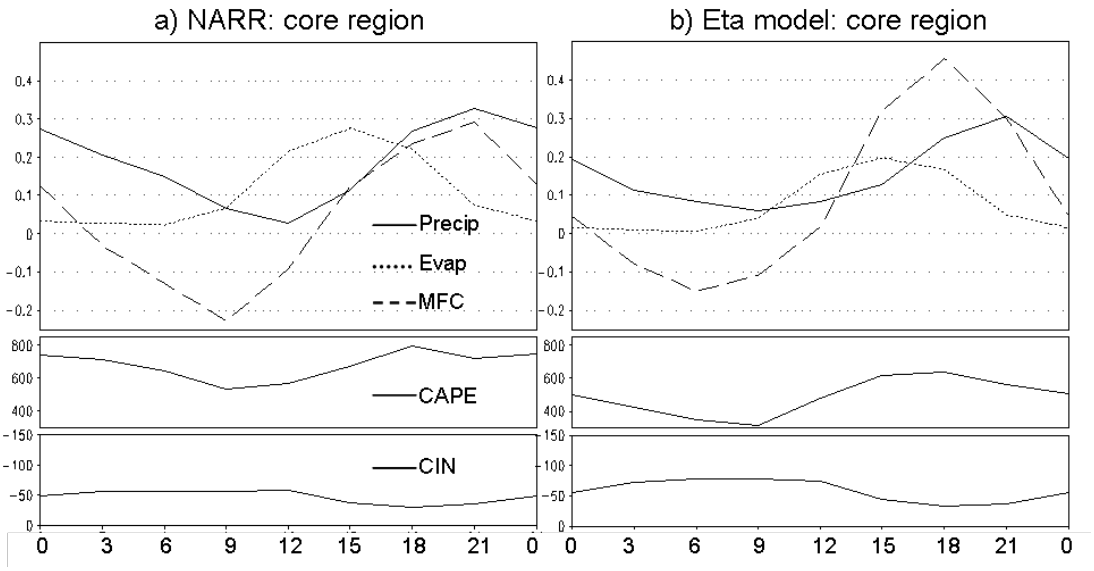

Figure 5: Land-only area average of several elements in the core monsoon region, from NARR (left) and the Eta model, for the 24-hour period beginning at local midnight. The upper panels depict precipitation (solid line, mm h^{-1}), moisture flux convergence (long dash, mm day^{-1}), and evaporation (dotted line, mm h^{-1}). The middle panels are CAPE (J kg^{-1}), and the bottom panels are convective inhibition (CIN, J kg^{-1}).

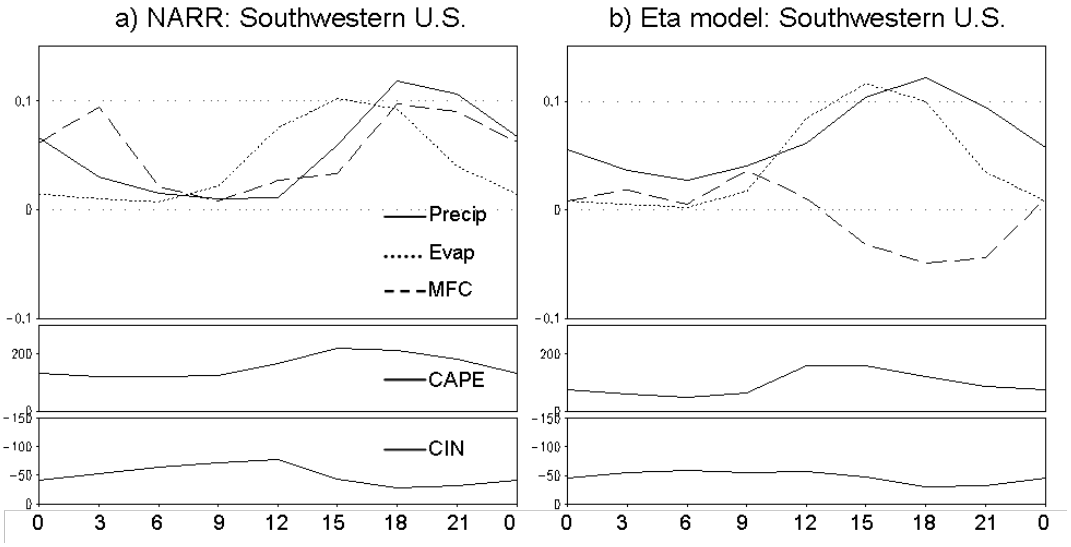

Figure 6: The same as in Figure 5, for the southwestern United States.

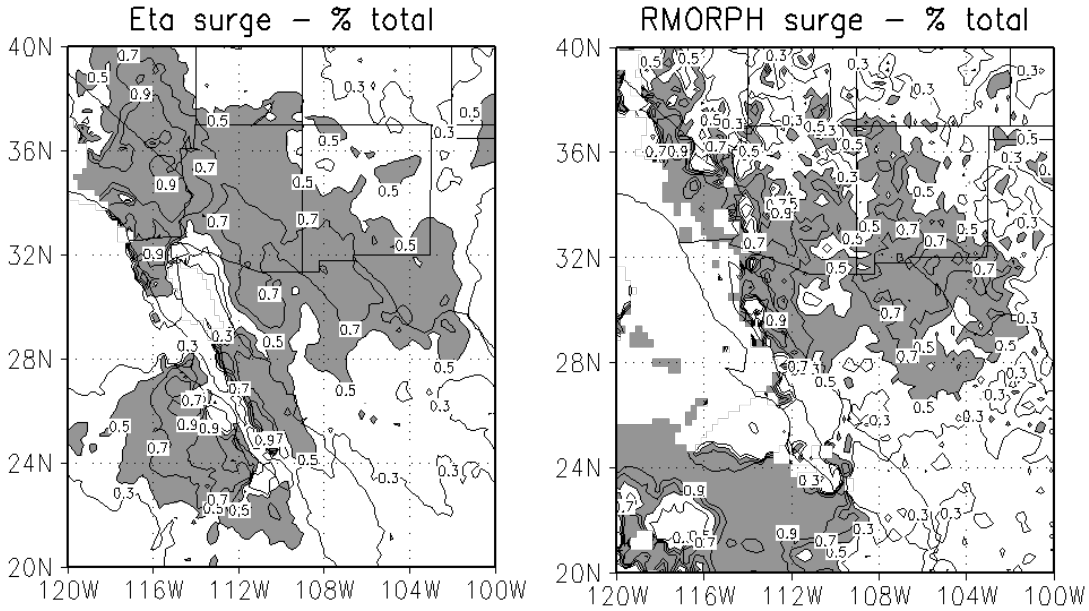

Figure 7: Percentage of precipitation during surge events for RMORPH satellite estimates (left) and Eta model forecasts (right). Gray areas represent greater than 50% of total precipitation occurring during surge events; white areas are less than 50%. The total amount of precipitation that fell during surges was compared to the total precipitation of the entire two-month period to produce this figure.

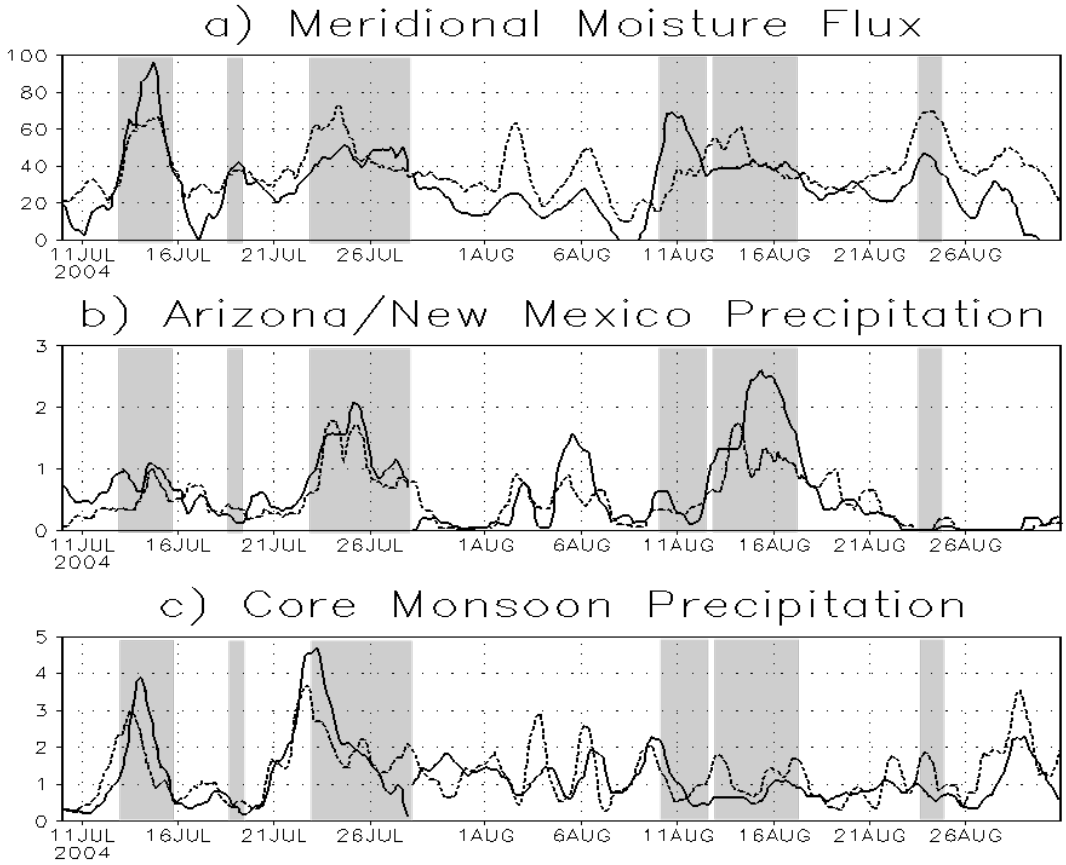

Figure 8: a) Meridional moisture flux at 30°N, 114°W, the northern Gulf of California. b) Area averaged precipitation for the southwestern U.S., and c) the core North American Monsoon region (bottom) for July10 –August 31, 2005. From Eta model forecasts (solid) and NARR satellite estimates (dashed); surge times are indicated by shaded regions.

a) NARR: 2002-2005 surge

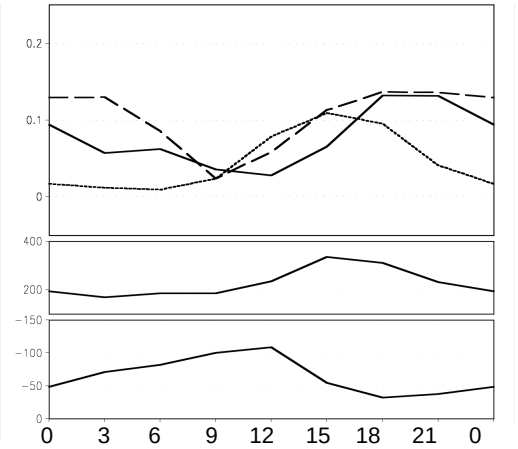

c) NARR: 2004 surge

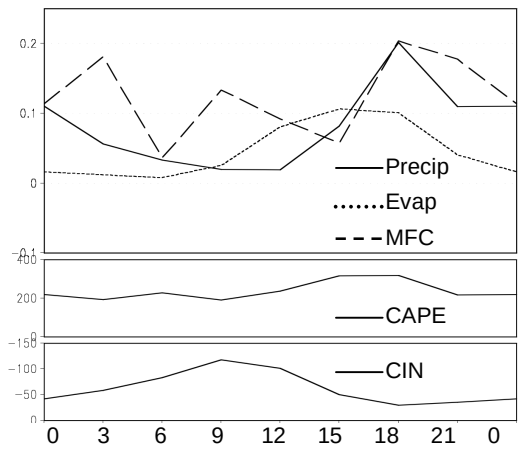

e) Eta model: 2004 surge

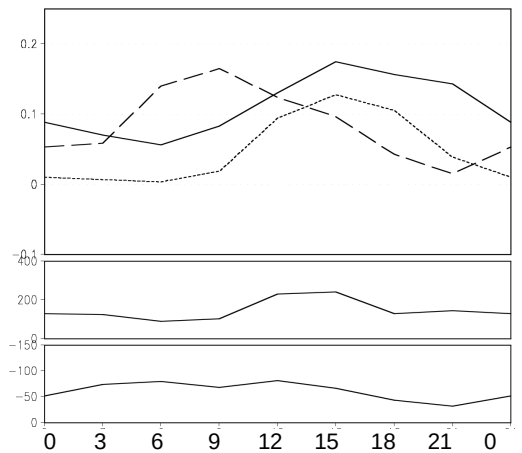

b) NARR: 2002-05 non-surge

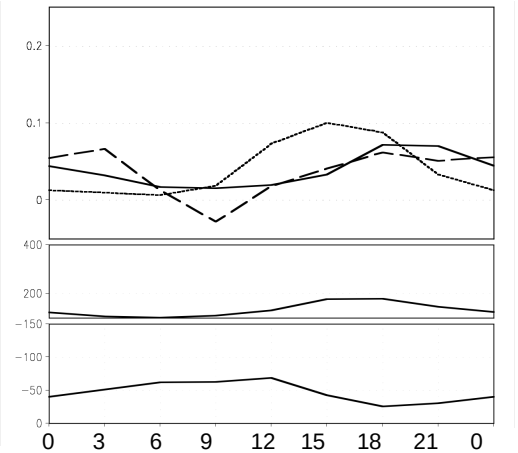

d) NARR: 2004 non-surge

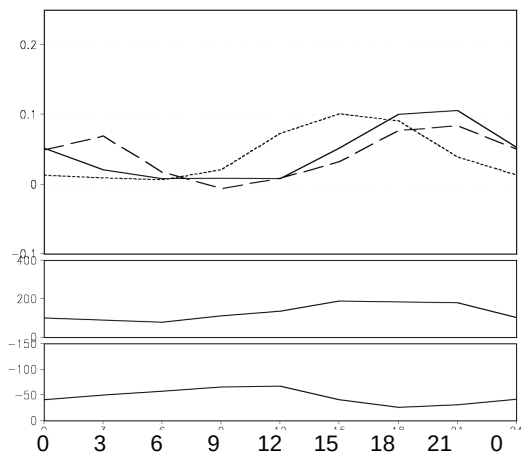

f) Eta model: 2004 non-surge

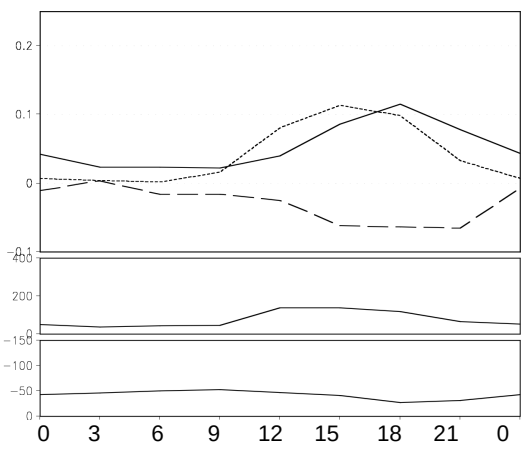

Figure 9 (preceding page): Land-only area average of several elements in the southwestern U.S., for the 24-hour period beginning at local midnight, for surge (top) and non-surge (bottom), as in Figure 6. a) and b) 2002-2005 July-September average, from NARR, c) and d) NAME field campaign period, from NARR, e) and f) NAME field campaign period, from Eta model. The upper panels depict precipitation (solid line, mm h^{-1}), moisture flux convergence (long dash, mm day^{-1}), and evaporation (dotted line, mm h^{-1}). The middle panels are CAPE (J kg^{-1}), and the bottom panels are convective inhibition (CIN, J kg^{-1}).

	NARR (4-yr)		**NARR (2004)**		**Eta Model (2004)**	
	Surge	**Non-surge**	**Surge**	**Non-surge**	**Surge**	**Non-surge**
Precipitation (mm d^{-1})	1.86	0.92	1.992	1.08	2.64	1.272
Evaporation (mm d^{-1})	1.07	0.94	1.08	0.98	1.104	0.96
CAPE (J kg^{-1})	226.1	132.5	237	130.7	146	76.7
CIN (J kg^{-1})	-64.9	-47.0	-61.8	-47	-60.9	-42.5
MFC (mm d^{-1})	1.04	0.37	0.99	0.34	0.66	-0.23

Table 1: Daily average values for surge and non-surge conditions, for the 4-year NARR average, and the NARR and the Eta model 2004 season.

References

Arkin, P. A., 1982: The Relationship Between Interannual Variability in the 200 mb Tropical Wind Field and the Southern Oscillation. *Mon. Wea. Rev.*, **110**, 1393-1404.

Badan-Dangon, A., C. E. Dorman, M.A. Merrifield, C.D. Winant, 1991: The lower atmosphere over the Gulf of California. *J. Geophys. Res.*, **96**, 16 877-16 896.

Barlow, M., S. Nigam, and E. H. Berbery, 1998: Evolution of the North American Monsoon System. *J. Climate*, **11**, 2238-2257.

_____, _____, and _____, 2001: ENSO, Pacific Decadal Variability, and U.S. Summertime Precipitation, Drought, and Streamflow. *J. Climate*, **14**, 2105-2128.

_____, M., and D. Salstein, 2006: Summertime Influence of the Madden-Julian Oscillation on Daily Rainfall over Mexico and Central America. *Geophys. Res. Lett.*, **33**, doi: 10.1029/2006GL027738.

Becker, E. J., and E. H. Berbery, 2008: The Diurnal Cycle of Precipitation over the North American Monsoon Region during the NAME 2004 Field Campaign. *J. Climate*, **21**, 771-787.

Berbery and J. Nogues-Paegle, 1993: Intraseasonal Interactions between the Tropics and Extratropics in the Southern Hemisphere. *J. Atmos. Sci*, **50**, 1950-1965.

_____, and M. S. Fox-Rabinovitz, 2003: Multiscale Diagnosis of the North American Monsoon System Using a Variable-Resolution GCM. *J. Climate*, **16**, 1929-1947.

Bluestein, H. B., 1993: *Synoptic-dynamic meteorology in midlatitudes: Vol. II.* Oxford University Press, New York, NY, 594 pp.

Bond, N.A., and G.A. Vecchi, 2003: The Influence of the Madden-Julian Oscillation on Precipitation in Oregon and Washington. *Wea. and Forecasting*, **18**, 600-613.

Bonner, W. D., 1968: Climatology of the low-level jet. *Mon. Wea. Rev.*, **96**, 833-850.

Bukowsky, M. S., and D. J. Karoly, 2007: A Brief Evaluation of Precipitation from the North American Regional Reanalysis. *J. Hydromet.*, **8**, 837-846.

Cayan, D. R., K. T. Redmond, and L. G. Riddle, 1999: ENSO and Hydrologic Extremes in the Western United States. *J. Climate*, **12**, 2881-2893.

Douglas, M. W., R. A. Maddox, and K. Howard, 1993: The Mexican Monsoon. *J. Climate*, **6**, 1665-1677.

Ek, M., K. Mitchell, Y. Lin, E. Rogers, P. Grunmann, V. Koren, G. Gayno, D. Tarpley, 2003: Implementation of Noah land surface model advances in the National Centers for Environmental Prediction operational mesoscale Eta model. *J. Geophys. Res.*, **108**, doi:10.1029/2002JD003296.

Fan, Y., and H. van den Dool (2004): Climate Prediction Center global monthly soil moisture data set at 0.5° resolution for 1948 to present, *J. Geophys. Res.*, **109**, doi: 10.1029/2003JD004345.

Gershunov, A., 1998: ENSO Influence on Intraseasonal Extreme Rainfall and Temperature Frequencies in the Contiguous United States: Implications for Long-Range Predictability. *J. Climate*, **11**, 3192-3203.

_____, and D. R. Cayan, 2003: Heavy Daily Precipitation Frequency over the Contiguous United States: Sources of Climatic Variability and Seasonal Predictability. *J. Climate*, **16**, 2752-2765.

Grimm, A. M., and R. G. Tedeschi, 2008: ENSO and extreme rainfall events in South America. *J. Climate*, accepted.

Groisman, P.Ya., and Coauthors, 1999: Changes in the Probability of Heavy Precipitation: Important Indicators of Climatic Change. *Climatic Change*, **42**, 243-283.

_____, R. W. Knight, and T. R. Karl, 2001: Heavy Precipitation and high streamflow in the Contiguous United States: Trends in the twentieth century. *Bull. Amer. Meteor. Soc.*, **82**, 219-249.

_____, _____, _____, D. R. Easterling, B. Sun, and J. H. Lawrimore, 2004: Contemporary Changes of the Hydrological Cycle over the Contiguous United States: Trends Derived from In Situ Observations. *J. Hydromet.*, **5**, 64-85.

_____, _____, D. R. Easterling, T. R. Karl, G. C. Hegerl, and V. N. Razuvaev, 2005: Trends in Intense Precipitation in the Climate Record. *J. Climate*, **18**, 1326-1350.

Hendon, H. H., and M. L. Salby, 1994: The Life Cycle of the Madden-Julian Oscillation. *J. Atmos. Sci.*, **51**, 2225-2237.

_____, and M. C. Wheeler, 2007: Seasonal Dependence of the MJO-ENSO Relationship. *J. Climate,* **20**, 531-543.

Higgins, R. W., Y. Yao, and X. L. Wang, 1997a: Influence of the North American Monsoon System on the U.S. Summer Precipitation Regime. *J. Climate,* **10**, 2600-2622.

_____, _____, E. S. Yarosh, J. E. Janowiak, and K. C. Mo, 1997b: Influence of the Great Plains Low-Level Jet on Summertime Precipitation and Moisture Transport over the Central United States. *J. Climate*, **10**, 481-507.

_____, and K. C. Mo, 1997: Persistent North Pacific Circulation Anomalies and the Tropical Intraseasonal Oscillation. *J. Climate*, **10**, 223-244.

_____, Y. Chen, and A.V. Douglas, 1999: Interannual Variability of the North American Warm Season Precipitation Regime. *J. Clim.*, **12**, 653-680.

_____, A. Leetmaa, Y. Xue, and A. Barnston, 2000a: Dominant Factors Influencing the Seasonal Predictability of U.S. Precipitation and Surface Air Temperature. *J. Climate*, **13**, 3994-4017.

_____, J.-K. E. Schemm, W. Shi, and A. Leetmaa, 2000b: Extreme Precipitation Events in the Western United States Related to Tropical Forcing. *J. Climate*, **13**, 793-820.

_____, R. W., V. Silva, J. Larson and W. Shi, 2007: Relationships between climate variability and fluctuations in daily precipitation over the United States. *J. Climate*, **15**, 3561-3579.

_____, _____, V. E. Kousky, and W. Shi, 2008: Comparison of Daily Precipitation Statistics for the United States in Observations and in the NCEP Climate Forecast System. *J. Climate,* In Press.

Hoerling, M.P., and A. Kumar, 2000: Understanding and Predicting Extratropical Teleconnections Related to ENSO. Published in El Niño and the Southern Oscillation, 2000, Cambridge University Press.

Husak, G. J., J. Michaelsen, and C. Funk, 2007: Use of the gamma distribution to represent monthly rainfall in Africa for drought monitoring applications. *Int. J. Climatol*., **27**, 935-944.

Jones, C., 2000: Occurrence of Extreme Precipitation Events in California and Relationships with the Madden-Julian Oscillation. *J. Climate*, **13**, 3576-3587.

_____, Waliser, Lau, Stern, 2004: Global Occurrences of Extreme Precipitation and the Madden-Julian Oscillation: Observations and Predictability. J. Climate, **19**, 6353-6370.

Katz, R. W., and B. G. Brown, 1992: Extreme events in a changing climate: variability is more important than averages. *Climatic Change*, **21**, 289-302.

Kiladis, G. N. and H. F. Diaz, 1989: Global Climatic Anomalies Associated with Extremes in the Southern Oscillation. *J. Climate*, **2**, 1069-1090.

Kousky, V. E., M. T. Kagano, and I. F. A. Cavalcanti, 1984: A review of the Southern Oscillation: Oceanic-atmospheric circulation changes and related rainfall anomalies. *Tellus*, **36A**, 490-502.

L'Heureux, M. L., and R. W. Higgins, 2008: Boreal Winter Links between the Madden-Julian Oscillation and the Arctic Oscillation. *J. Climate*, **21**, 3040-3050.

Lin, Y., K. E. Mitchell, E. Rogers, M. E. Baldwin, and G. J. DiMego, 1999: Test assimilations of the real-time, multi-sensor hourly precipitation analysis into the NCEP Eta model. Preprints, *8th Conference on Mesoscale Meteorology*, Boulder, CO, Amer. Meteor. Soc., 341-344.

Madden, R.A., and P.R. Julian, 1971: Description of a 40-50 day oscillation in the zonal wind in the tropical Pacific. *J. Atmos. Sci.*, **28**, 702-708.

_____, and _____, 1972: Description of Global-Scale Circulation Cells in the Tropics with a 40-50 Day Period. *J. Atmos. Sci.*, **29**, 1109-1123.

Meehl, G. A., and W. M. Washington, 1996: El Niño-like climate change in a model with increased atmospheric CO2 concentration. *Nature*, **382,** 56-60.

_____, and Coauthors, 2006: Climate change projections for the twenty-first century and climate change commitment in the CCSM3. *J. Climate*, **19**, 2597-2616.

Mesinger, F., and Coauthors, 2006: North American Regional Reanalysis. *Bull. Amer. Meteor. Soc.*, **87**, 343-360.

Mo, K.C., and W.R. Higgins, 1998a: Tropical Influences on California Precipitation. *J. Climate*, **11**, 412-430.

_____, and _____, 1998b: Tropical Convection and Precipitation Regimes in the Western United States. *J. Climate*, **11**, 2404-2423.

_____, M. Chelliah, M. L. Carrera, R. W. Higgins, and W. Ebisuzaki, 2005: Atmospheric Moisture Transport over the United States and Mexico as Evaluated in the NCEP Regional Reanalysis. *J. Hydromet.*, **6**, 710-728.

Nakamura, H., T. Sampe, Y. Tanimoto, and A. Shimpo, 2004: Observed Associations Among Storm Tracks, Jet Streams, and Midlatitude Oceanic Fronts. *Earth's Climate: The Ocean-Atmosphere Interaction, Geophys. Monogr.*, 147, Amer. Geophys. Union. 329-345.

Ropelewski, C. F. and M. S. Halpert, 1986: North American Precipitation and Temperature Patterns Associated with the El Niño/Southern Oscillation (ENSO). *Mon. Wea. Rev.*, **114**, 2352-2362.

_____, and _____, 1996: Quantifying Southern Oscillation-Precipitation Relationships. *J. Climate*, **9**, 1043-1059.

_____, and M.A. Bell, 2008: Shifts in the Statistics of Daily Rainfall in South America Conditional on ENSO Phase. *J. Climate*, **21**, 849-865.

Schubert, S. D., Y. Chang, M. Suarez, and P. Pegion, 2005: On the Relationship Between ENSO and Extreme Weather Over the Contiguous U.S. *U.S. CliVar Variations*, **3**, 1-4.

Semenov, V.A., and L. Bengtsson, 2002: Secular Trends in Daily Precipitation Characteristics: Greenhouse Gas Simulation with a Coupled AOGCM. *Climate Dyn.*, **18,** 123-140.

Shafran, P., J. Woollen, W. Ebisuzaki, W. Shi, Y. Fan, R. Grumbine, and M. Fennessy, 2004: Observational data used for assimilation in the NCEP North American Regional Reanalysis. Preprints, *14th Conf. on Applied Climatology*, Seattle, WA, Amer. Meteor. Soc., 1.4.

Shenton, L. R., and K. O. Bowman, 1970: Remarks on Thom's Estimators for the Gamma Distribution. *Mon. Wea. Rev.*, **98**, 154-160.

Silva, V.B.S., and E. H. Berbery, 2006: Intense Rainfall Events Affecting the La Plata Basin. *J. Hydromet.*, **7**, 769-787.

_____, V.E. Kousky, W. Shi, and R.W. Higgins, 2007: An improved gridded historical daily precipitation analysis for Brazil. *J. Hydromet.*, **8**, 847-861.

Thom, H. C. S., 1958: A Note on the Gamma Distribution. *Mon. Wea. Rev*., **86**, 117-122.

Ting, M., and H. Wang, 1997: Summertime U.S. Precipitation Variability and its Relation to Pacific Sea Surface Temperature. *J. Climate*, **10**, 1853-1873.

Watterson, I. G., and M. R. Dix, 2003: Simulated changes due to global warming in daily precipitation means and extremes and their interpretation using the gamma distribution. *J. Geophys. Res.*, **108**, doi:10.1029/2002JD002928.

Wheeler, M.C., and H.H. Hendon, 2004: An All-Season Real-Time Multivariate MJO Index: Development of an Index for Mopnitoring and Prediction. *Mon. Wea. Rev.*, **132**, 1917-1932.

Wilby, R.L., and T. M. L. Wigley, 2002: Future Changes in the distribution of daily precipitation totals across North America. *Geophys. Res. Lett.*, **29**, doi:10,1029/2001GL013048.

Wilks, D. S, 1990: Maximum Likelihood Estimation for the Gamma Distribution Using Data Containing Zeros. *J. Climate*, **3**, 1495-1501.

_____, 1995: *Statistical Methods in the Atmospheric Sciences.* Academic Press, 467 pp.

Yano, J.I., R. Blender, C.D. Zhang, and K. Fraedrich, 2004: 1/f noise and pulse-like events in the tropical atmospheric surface variables. *Quart. J. of the Royal Meteor. Soc.*, **130**, 1697-1721.

Zhang, C., 2005: Madden-Julian Oscillation. *Rev. Geophys.*, **43**, RG2003, doi:10.1029/2004RG000158.

_____, and J. Gottschalck, 2002: SST Anomalies of ENSO and the Madden-Julian Oscillation in the Equatorial Pacific. J. Climate 15, 2429-2445.